CHAPTER-1

INTRODUCTION

Energy is the basic need of any country. More than 60% (website referred at sr. no. 34) of total power generation in India is contributed by steam and gas power plant. With the growing need of energy conservation, constant efforts are actively pursued throughout the world to improve the efficiency of the power plants for meeting the energy need of the world as well as for proper utilization and saving of fuel. The efficiency of any gas or thermal power plant usually depends on the efficiency and working of the turbines and hence turbines are the basic component of any power plant which needs to be improved for improving the efficiency of the plant. The viscous diffusion in the flow through turbine cascade results in the decrease in integrated flux of total pressure through the cascade. Since this decrease in total pressure flux is related to the amount of kinetic and potential energy lost in the cascade by the flow, hence this pressure flux is termed as 'total pressure loss' or simply 'loss'. This total pressure loss has significant effect on the efficiency of the cascade and hence it should be minimized. The historical classification and division of loss into 'profile loss' and 'end loss' continues to be widely used although it is now clearly recognized that the loss generation mechanisms are seldom independent. The first is the loss due to boundary layer on the blade surface and is termed as 'profile loss' due to its dependence on the surface of blade profile. The remaining part of total pressure loss depends on the presence of solid endwalls and is termed as 'endwall or secondary losses'. The secondary losses include loss from the boundary wall on the endwall wetted surface, loss due to flow separation, diffusion of passage secondary vortex and additional loss due to change in blade surface boundary

layers caused by secondary flow. End loss forms a major part of internal aerodynamic losses occurring in turbine. Phenomena of secondary loss are important in turbomachinery mainly for two reasons. Firstly, it causes pressure loss in a stage & secondly, it makes stage exit flow non uniform, which could cause increased pressure losses in a downstream row.

Thus the improvement in the efficiency of turbomachinery becomes the key research area. For getting the improved efficiency of turbomachine it became essential to analyze the flow field and associated loss generation in turbine. The proper designing of turbo machines installed in the plant can minimize the losses and hence improves the efficiency of the plant. In the steam turbines, the steam enters at the cascade inlet, flows between the blade passages of fixed and moving blades and then moved to cascade outlet while flowing between the tailboards.

It is essential to design the turbine cascade in such a way so as to minimize the chances of secondary flow and losses. These losses deviates the expansion of fluid through the turbine from the isentropic process and hence reduce the work output through turbines. These losses reduce the economy of power plant.

1.1 Motivation

The loss of work output and decreased efficiency of turbines and hence the power plant is direct waste of power in any country. The need of increased output with the same input for economical running of the plant and saving of fuel has increased. This can be achieved by proper designing of turbine cascade. Moreover, flow in turbines is extremely complex, three-dimensional and unsteady, resulting in high losses, reduced efficiency & poor performance.

Denton, [1993] said, “End wall loss is the most difficult loss component to understand & predict as virtually all prediction methods are still based on correlations of empirical data, and the result obtained is just approximated to the actual experimental result”. Tremendous work has been done over the last fifty years but secondary flow mechanism is still not clear. Even today the 3-D flow pattern in cascade creates challenges for the researchers and turbo machinery manufactures. But with the availability of various computational software the task of designing becomes a bit easier due to software based simulation process. This being the guiding factor for working on the computational software with the effort of modifying the turbine cascade for decreasing the losses

1.2 Problem Statement

The primary objective of this project is to use the computational software with the aim of numerical study of secondary loss phenomenon in the turbine cascade. Experiment had been conducted in a wind tunnel on the model of profile 6030 rectilinear cascade of smooth turbine blades profile for measurement of end losses by **Samsher [2007].** Three -dimensional model of 6030 cascade geometry was made with the help of Gambit® 2.2.3 as pre processor & FLUENT® 6.2 will be used as solver & post processor for flow simulation. On the model of rectilinear cascade of turbine blades, discretization has been done with the help of Gambit®. Then Fluent® was used on the flow through the blades. From the simulation result, presence and pattern of secondary flow and averaged loss coefficient had been studied for the smooth blade. This numerical result had been validated with the experimental result obtained by **Samsher [2007].**

The secondary loss in smooth cascade was compared with the secondary loss in the cascade having rough surface. This work was done in order to find out the effect of roughness present on various blade surface of the turbine cascade on the secondary loss

1.3 Plan of work

The major milestones in work plan made at beginning of work included the following key targets

- Literature review through all possible resources which are accessible and find suitable articles, reading materials, thesis of work done in past which are relevant to present work.
- Reading of the collected articles, which are relevant to present work.
- Summarizing each article, that what and how has been done, observations and results of various researchers, limitation and future scope of various articles for further work.
- Preparation of the Project Proposal.
- Preparing the 3-D geometry of blade profile & measurement domain in the Gambit® 2.2.3 software. Earlier works on this area usually focused on 2-D geometry blade profile modeling & simulation work. Hence the present work is an advancement over previous works done
- Conservation equations will then be solved by making use of appropriate mathematical model, and the solver & post processor available in FLUENT® 6.2.

- Analyzing the secondary loss in smooth cascade. The results of 3-D simulation will be critically analyzed for level of approximations & validated with those of experimental data
- Applying roughness of 500μm on various surfaces on the same cascade and then comparing the secondary loss for the cascade having roughness on various surfaces with the smooth cascade.
- Thesis writing & presentation.

Experiments were earlier conducted in a wind tunnel on rectilinear cascade to study effect of blade surface roughness on profile loss in steam turbine by **Samsher [2007]**. The same blade profile was modeled in 3-D with help of Gambit® 2.2.3. The model was tested on FLUENT® 6.2. After setting proper operating and boundary conditions, the average total pressure loss, thus found will be validated against experimental results for the smooth blade.

1.4 Expected outcome and actual achieved

Efficiency is probably the most important performance parameter for steam turbines. By studying effect of roughness on the secondary loss phenomenon in the rectilinear cascade, we can appreciate the loss mechanisms in these machines in a better way. This work will open a new avenue of research as no work on this area was done here earlier.

Total pressure loss for the smooth blades was calculated using CFD simulation. This numerical model was validated with the experimental work done by **Samsher [2007].** After this secondary losses were computed using the same CFD model for the

same reaction blade profile but a roughness of 500µm were applied on different surfaces

1.5 Organization of report

The report has been organized in the following sequence. The report is divided into 6 chapters. Introduction of the project topic is given in Chapter 1. An overview of the related literature has been given in Chapter 2. Description of governing equations used, selection of turbulence model, boundary and operating conditions applied for the three- dimensional modeling domain, has been described in Chapter 3. Results followed by discussions are presented in Chapter 4. Conclusions are presented in Chapter 5. Future Scope of the present work is presented in Chapter 6. References are presented after Chapter 6, followed by appendices.

CHAPTER-2

LITERATURE REVIEW

2.1 Overview

Aim of this chapter is to provide an overview of published work that is relevant to current investigation. Given the scope of present work, a comprehensive review of all contributing research is not possible. Review of relevant published literature pertaining to current work is presented in this chapter.

2.2 Theoretical background

Breakdown of turbine internal losses into 'profile loss', 'end wall loss' and 'leakage loss' continues to be widely used, though it is now clearly established that loss generation mechanisms are seldom independent. Secondary flows are a mean flow (website referred at sr. no. 35) in the transverse plane superimposed upon the axial mean flow and are generated and maintained by one of two fundamentally different mechanisms. The first occurs in curved ducts and is pressure driven, and the second is turbulence driven and is found in non-circular straight ducts. The first kind of secondary flow occurring in the bent ducts, can occur in the laminar flow with large relative velocities, of the order of 20-30% of the stream wise velocity. Second kind of secondary flow occurring in the non-circular ducts, can occur only in the fully developed turbulent flow condition resulting in relative velocity of the order of 2-3% of the stream wise velocity.

Secondary flows arise due to the production and redistribution of low momentum fluid within a blade passage. Secondary flows show very complex flow pattern, which involves vortices with strong three-dimensionality. Blade passage of very less height

gets fully occupied by the secondary vortices and subjected to higher losses whereas the longer blade experiences lesser secondary losses as larger proportion of their height is free from secondary vortices.

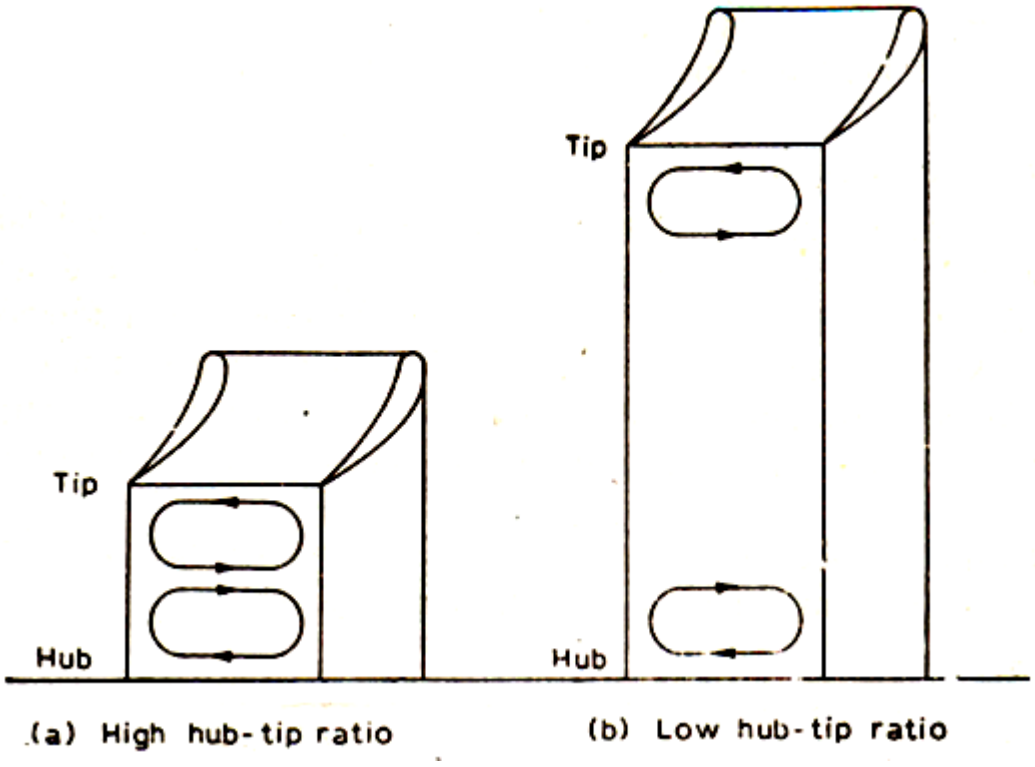

Fig. 2.1: Secondary vortices in short and long blades *(S M Yahya, 2002)*

Secondary losses generally includes all the losses occurring on the walls, hub and casing. Total losses also vary along the blade height. Total losses are maximum along the hub and tip due to secondary flow and losses *(S M Yahya, 2002).* So if total losses in a blade passage are measured along the blade height then peak appears near the hub and tip as shown in Fig.2.2. The loss in the central region which is free from secondary vortices is small and is subjected to only profile losses.

The mechanism of secondary loss generation is usually complex due to relative rotation of blade rows and end wall. In addition to this the tip leakage flow makes the secondary loss mechanism more complicated. Continuous research has been done to predict the exact mechanism of secondary losses which are usually based on the empirical data, but this field still provide challenge to the researchers and hence a wide scope of findings are still open for the researchers. Secondary flow can result into 30% of the total pressure loss through a turbine stage.

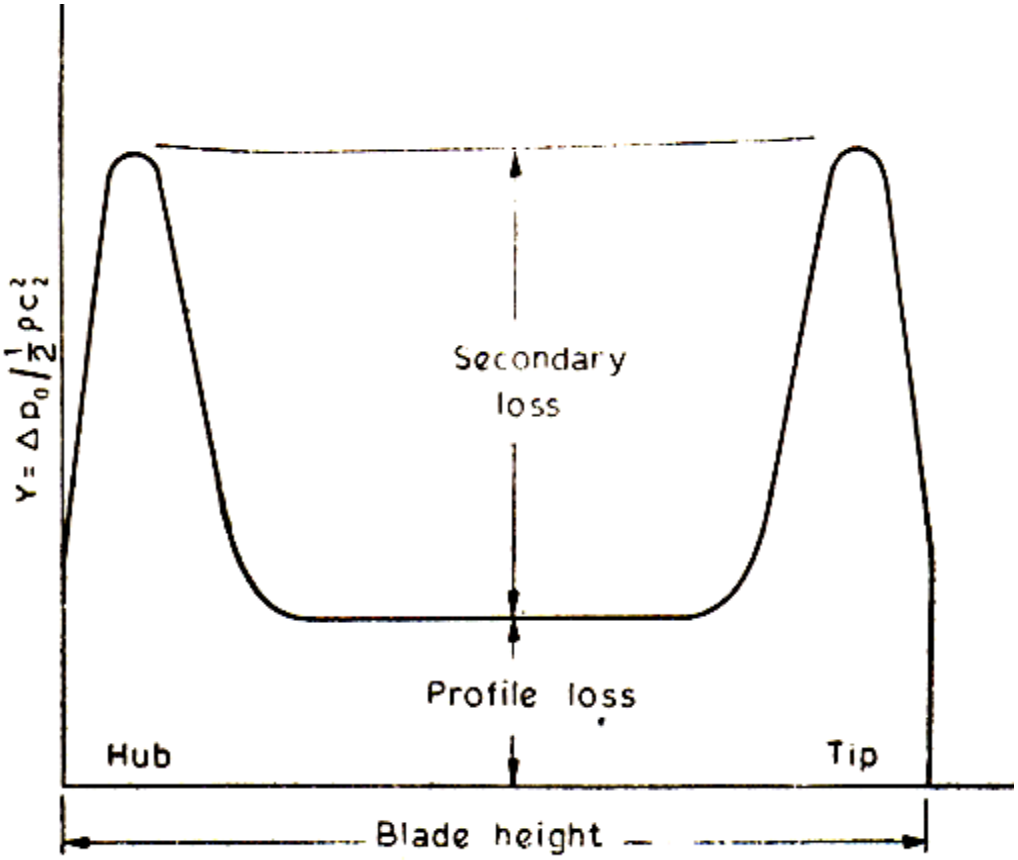

Fig. 2.2: Variation of losses along blade height *(S M Yahya, 2002)*

Turbine internal losses can be categorized as 'profile loss', 'end/secondary loss' and leakage loss. Somehow one loss is dependent on other and loss generation mechanism is seldom independent. Usually the relative magnitudes of various turbine internal losses depend upon the type of turbine, blade aspect ratio, blade turning, pitch to chord ratio, tip

clearance and inlet vorticity. Various researchers showed the variation of various internal losses with different parameters.

2.3 Recent work

Yaras and Sjolander [1992 b] shows the schematic breakdown of losses in the end region excluding profile losses as shown in Figure 2.3.

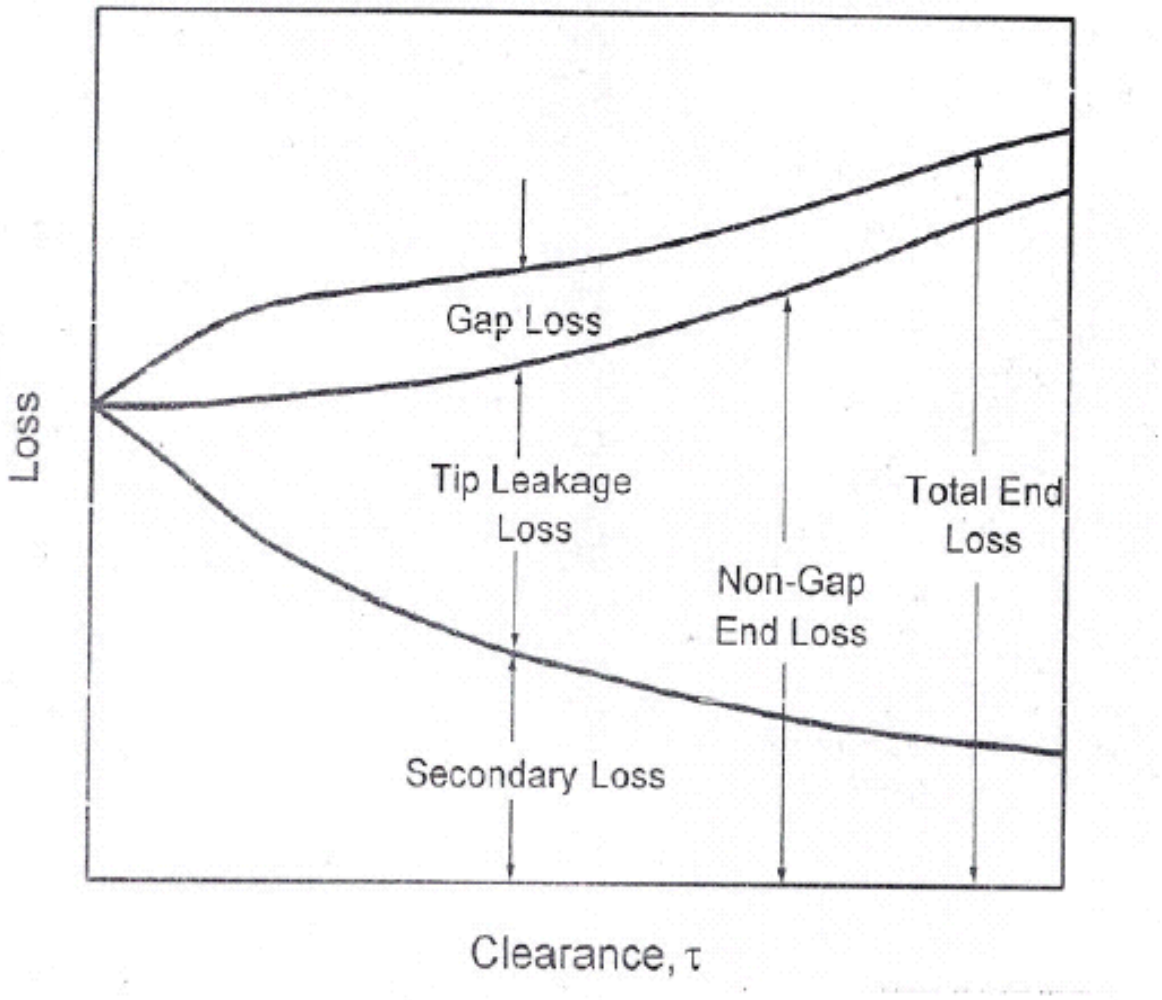

Fig 2.3: Schematic breakdown of losses in the end region, excluding profile *loss (Yaras and Sjolander, 1992b)*

Extensive amount of research has been conducted over past fifty years to understand and estimate secondary flows in axial blade cascade. First classical

secondary flow vortex system, which was predicted by classical secondary flow theories is shown below in Figure 2.4 and was described by **Hawthorne [1955].** It shows resulting component of exit vorticity in direction of flow when the fluid, with inlet vorticity is deflected through the cascade.

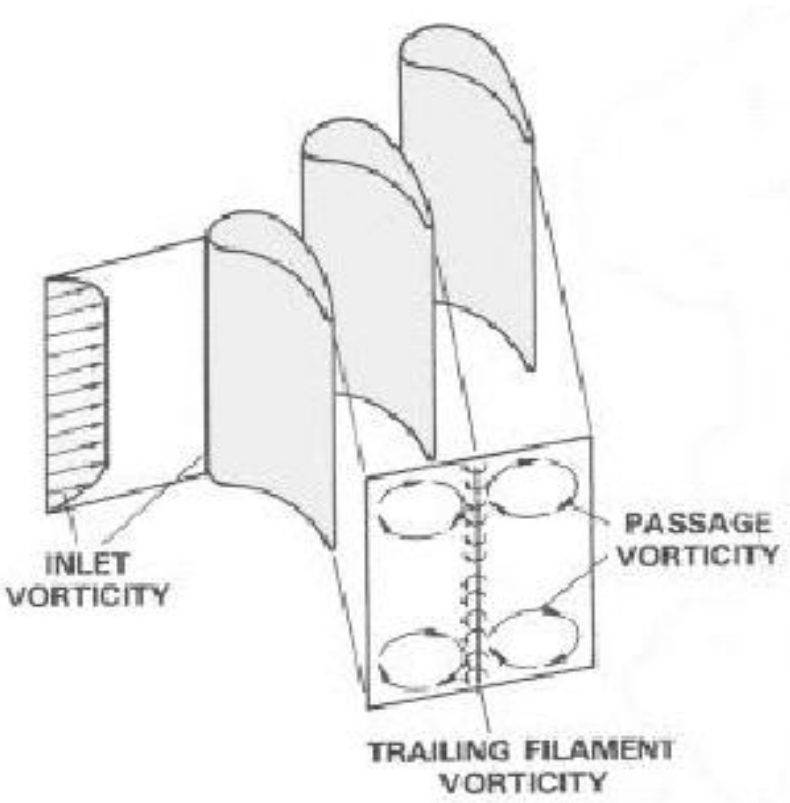

Fig.2.4: *Classical Secondary Flow Model (Hawthorne 1955)*

As a result of Hawthorne's model, details of flow field in cascades have been fairly well mapped by a number of researchers with help of visualization techniques. Some of these techniques include smoke wire, ink-dot-liquid film and China film techniques.

Langston et al. [1977] was one of the first to study the evolution of secondary flows. He used hot wire and flow visualization techniques to qualitatively assess flow

patterns at boundary layer, near the end wall region of a cascade. Langston said that the incoming inlet boundary layer splits into two sections at a point known as saddle point, which is located at the leading edge of the blade as shown in Fig 2.5. One stream moves towards the pressure surface and other towards suction surface due to the adverse pressure gradient which resulted into 3-D flow separation and horseshoe vortex formation. End wall cross flow is observed, which is the phenomenon of drifting of pressure surface leg of horseshoe vortex towards the adjacent suction surface because of the blade to blade pressure gradient. Suction surface leg rotates in opposite direction of pressure surface leg and consequently termed as counter vortex. The counter vortex mix with passage vortex and then drawn into end wall region on suction side of blade.

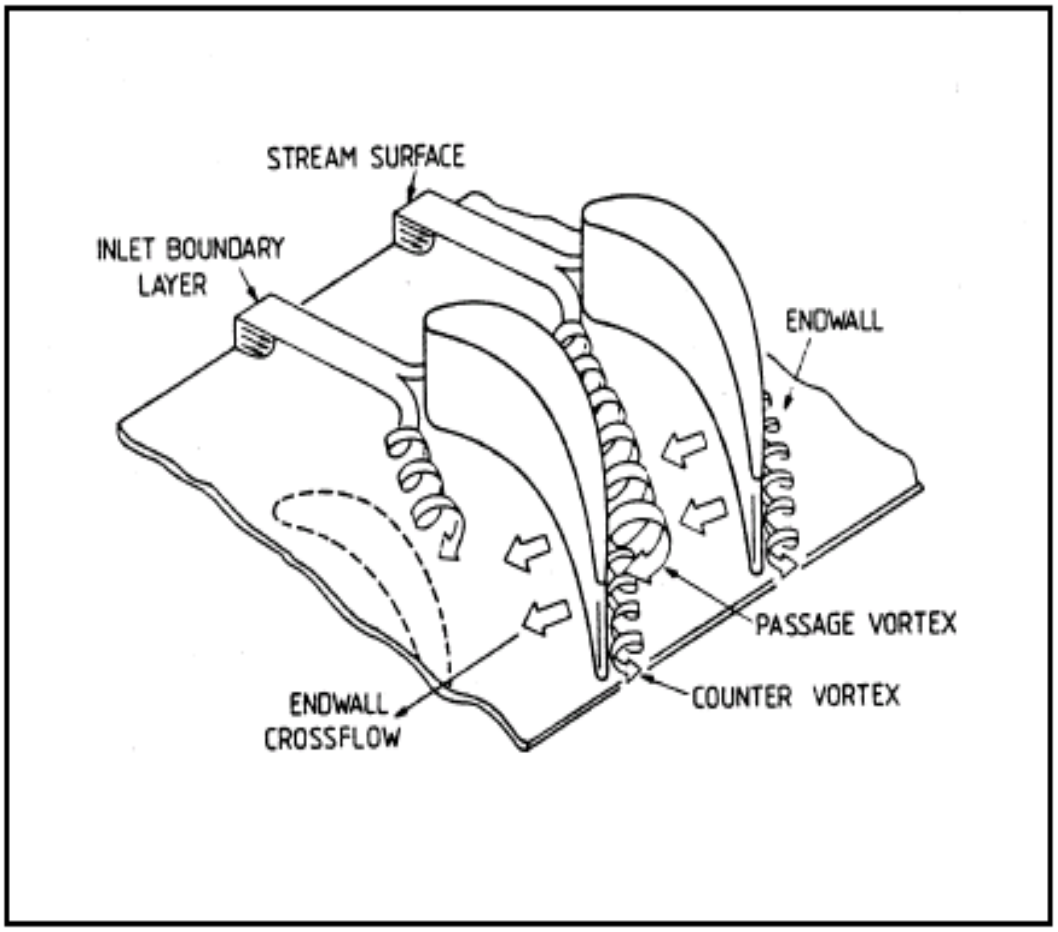

Fig. 2.5: *End wall vortex pattern (Langston et al. 1977)*

Further experiments were performed to compare Langston's results. One such experiment was by **Marchal et al. [1977]** who agreed that pressure surface leg of horseshoe vortex did merge and strengthen the passage vortex. Using a coloured smoke wire technique, and evidence of a large number of photographs, **Sieverding et al. [1983]** proposed a model that was able to clarify evolution of secondary flows. His model shown in Fig. 2.6 revealed that suction and pressure legs of the horseshoe vortex did combine to form passage vortex

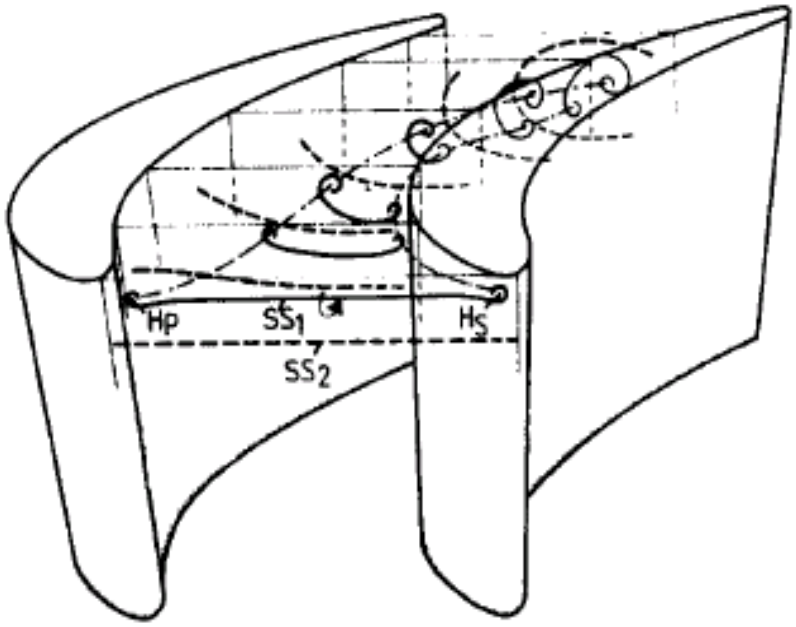

Fig.2.6: *Development of the Horseshoe and Passage Vortices (Sieverding et al. 1983)*

Sharma et al. [1987] showed flow patterns associated with inlet boundary layer in a turbine cascade which are in agreement of the previous work done by Langston et al. as shown in Fig. 2.7.

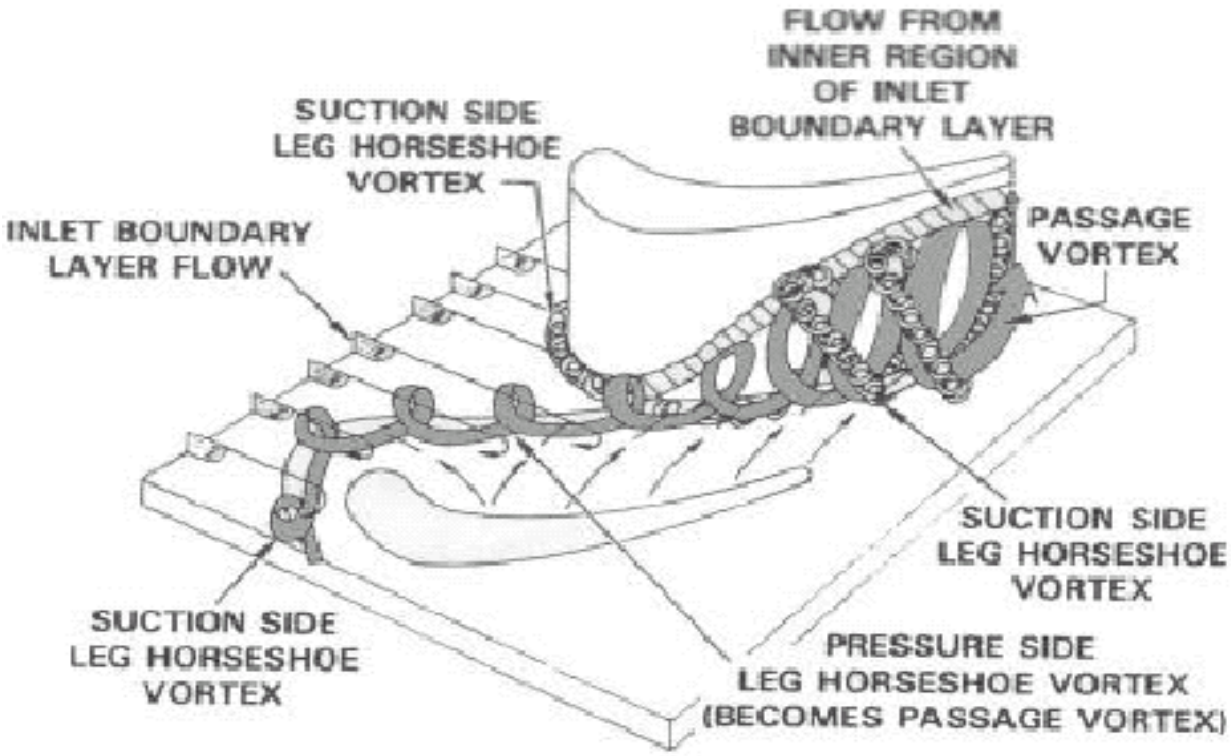

Fig. 2.7: *Cascade flow structure (Sharma et al. 1987)*

Wang et al., (1997) confirmed the works of Sieverding by using smoke wire visualization techniques in blade cascade. He revealed the existence of pressure and suction leg horseshoe vortices. Suction leg vortex twist itself around the pressure leg vortex and form the passage vortex. He concluded that pressure side vortex moves towards the suction side and merge with passage vortex at approximately one fourth of the distance from the leading edge.

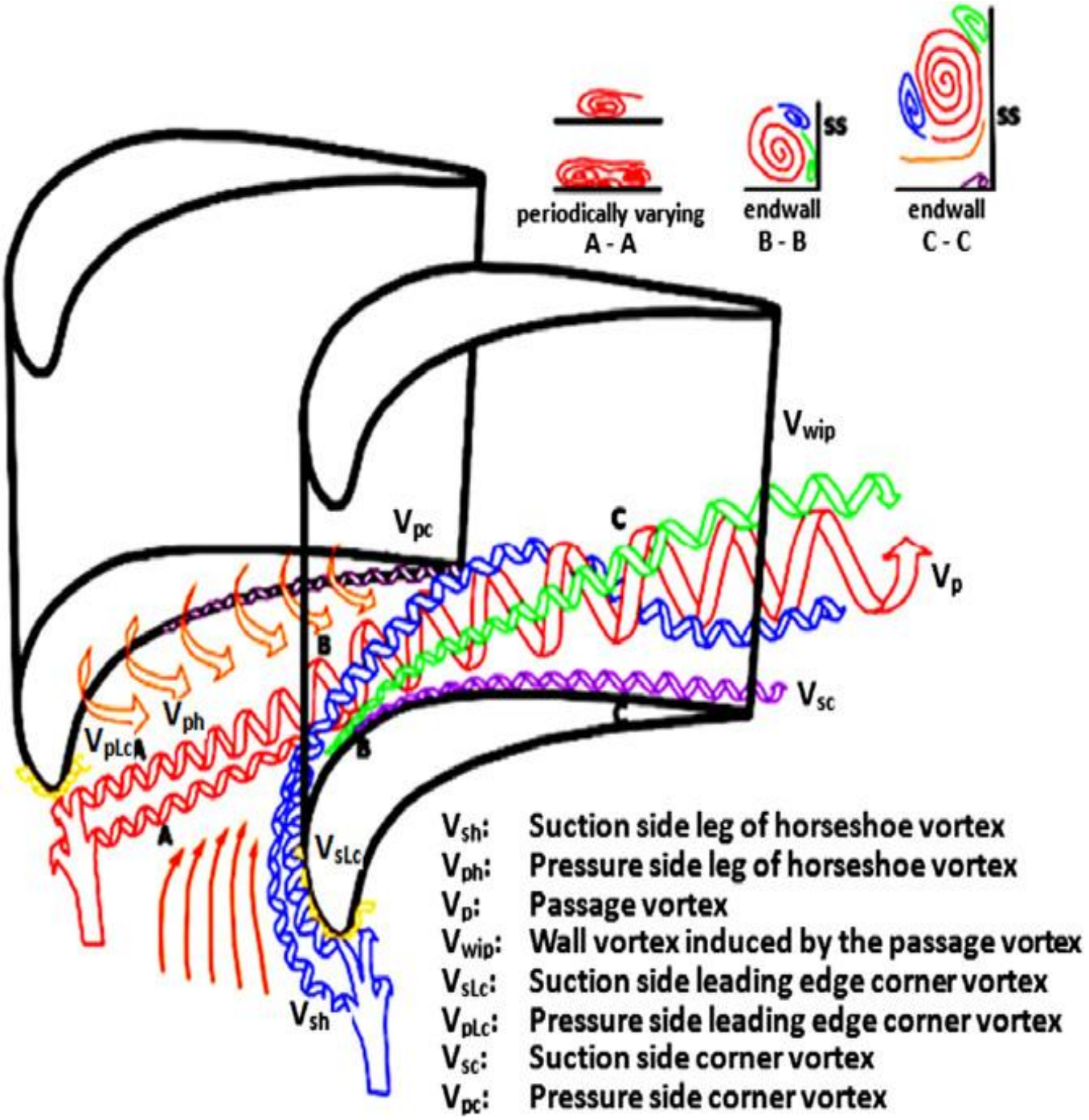

Fig. 2.8: Secondary flow model *(Wang et al. 1997)*

2.4 Ways of Reducing Secondary Losses

The total pressure loss in the cascade is accounted for the 'profile' and 'secondary losses'. These losses directly affect the efficiency of the cascade. Reduction of these losses is essential. Various researchers tried to find out the ways of reducing the secondary losses in the cascade.

There are two methods of reducing secondary losses. One is leading edge modification and other is end wall contouring. There are two main design of leading edge geometry: the fillet and the bulb. The leading edge fillet can reduce the radial total pressure gradient near the top of the fillet and hence prevent the generation of the leading edge vortex by accelerating the incoming boundary layer. The leading edge bulb can intensify the suction side branch of the horseshoe vortex with a desirable weakening effect on the passage vortex.

Another method of reducing secondary flow is end wall contouring, including the meridional plane end wall contouring and non-axisymmetry end wall contouring. These methods are proposed by various researchers, which are tried to be summarized in this section with their corresponding effect on the secondary flow.

2.4.1 End Wall Contouring

Moon et al. [2001] analyzed the effect of end wall fencing for reducing the secondary flow using k-ξ turbulence model. They justified the optimized positioning of the endwall fencing for reducing the secondary flow losses. They validate the computational result with the Wang et al. experimental data for the turbine cascade shown below.

Table 2.1: Turbine cascade geometry *(Moon et al. 2001)*

Chord length (C)	184.15 mm
Axial chord to chord ratio (C_{ax}/C)	0.704
Aspect ratio (H/C)	2.483
Solidity (C/P)	0.75
Blade inlet angle (β_1)	−35°
Blade outlet angle (β_2)	72.5°
Turning angle	107.5°
Incidence angle	0°

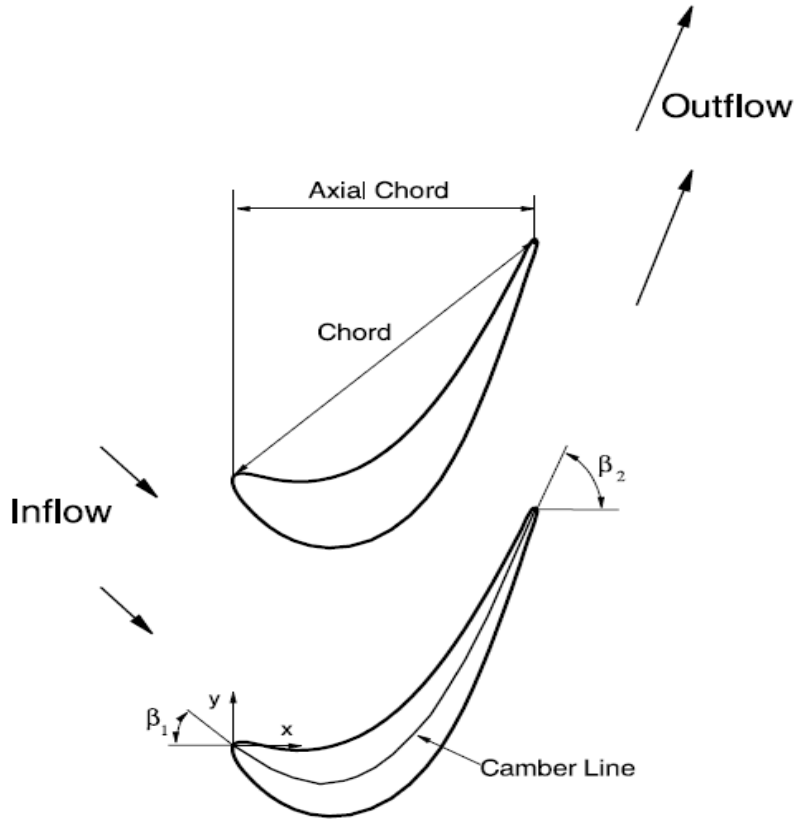

Fig. 2.9: Turbine blade definition and co-ordinate system *(Moon et al. 2001)*

They mount the fence of 5 mm thickness of same profile as camber line on cascade end wall. Three fences 1/3rd, 2/3rd and 3/3rd heights of inlet boundary layers were used for experimental purpose.

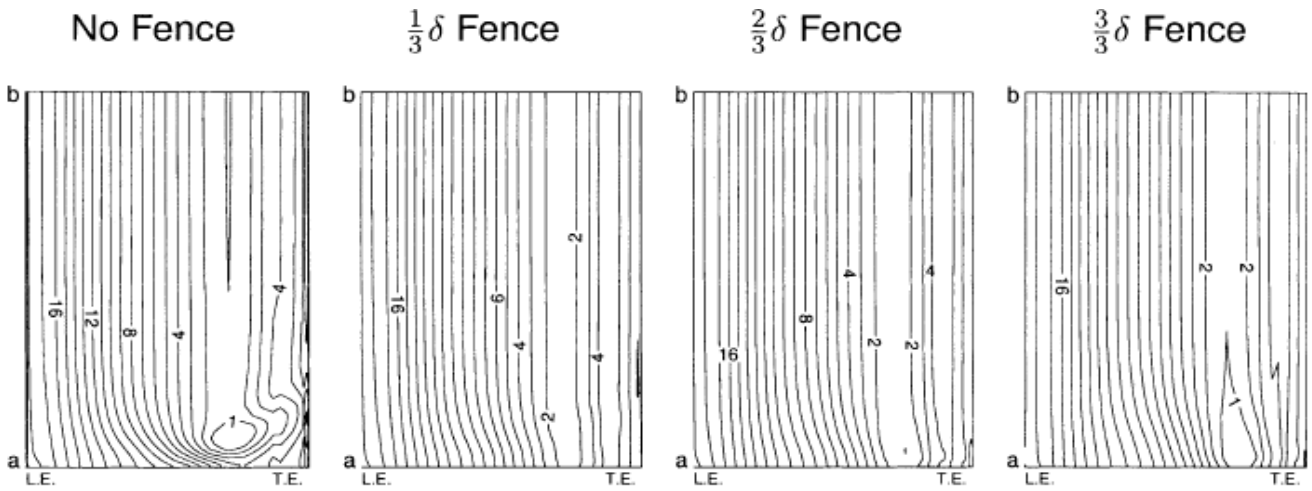

Fig.2.10: Contour plots of static pressure coefficients at the suction surface (a) end wall b) midspan (Moon et al. 2001)

It is clear from the static pressure coefficients plots that with the end wall fencing secondary flow near the suction surface is suppressed because the end wall fencing prevents the merging of pressure side horse shoe vortex with the passage vortex and hence total pressure loss decreases. Increasing the fence height, shift the blocking point of the divided streamline in the downwards direction, but the strength of secondary flow get increased at the suction side with overall increase in the secondary flow losses with increased fence height. It can be seen through the graph that the end wall fencing with a height of 1/3rd of the boundary layer thickness reduces the secondary flow loss to greatest extent.

Saha et al. [2008] analyzed the turbulent flow through a three dimensional non-axisymmetrical blade passage and found out the effect of endwall contouring. Contouring is usually achieved by contracting the flow area upstream of the blade passage in the streamwise direction, which accelerates the flow through the blade passage. The use of fillet modifies the pressure distribution locally near the junction, thus reducing the strength and size of secondary vortices. Endwall profiling is done in such a way to have convex

curvature in the pressure side and concave curvature on the suction side. The convex surface increases the velocity by reducing the local static pressure, while the concave surface decreases the velocity by increasing the local pressure.

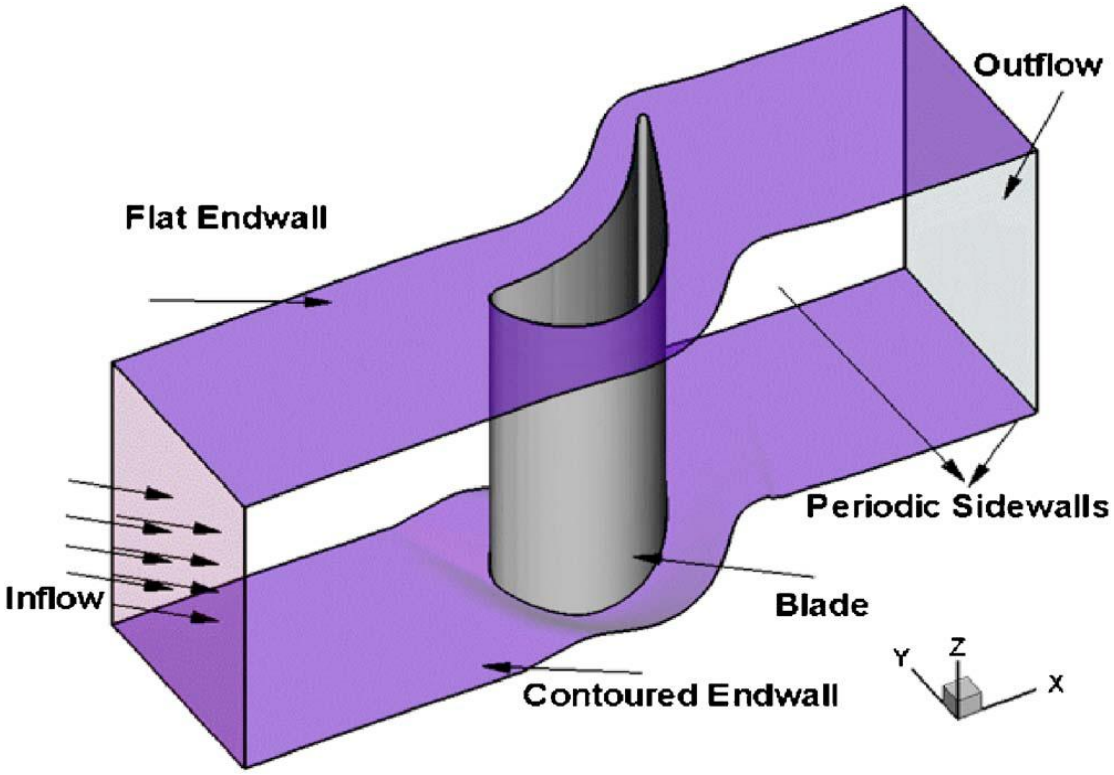

Fig. 2.11: Flow model and the confining boundaries (Saha et al., 2008)

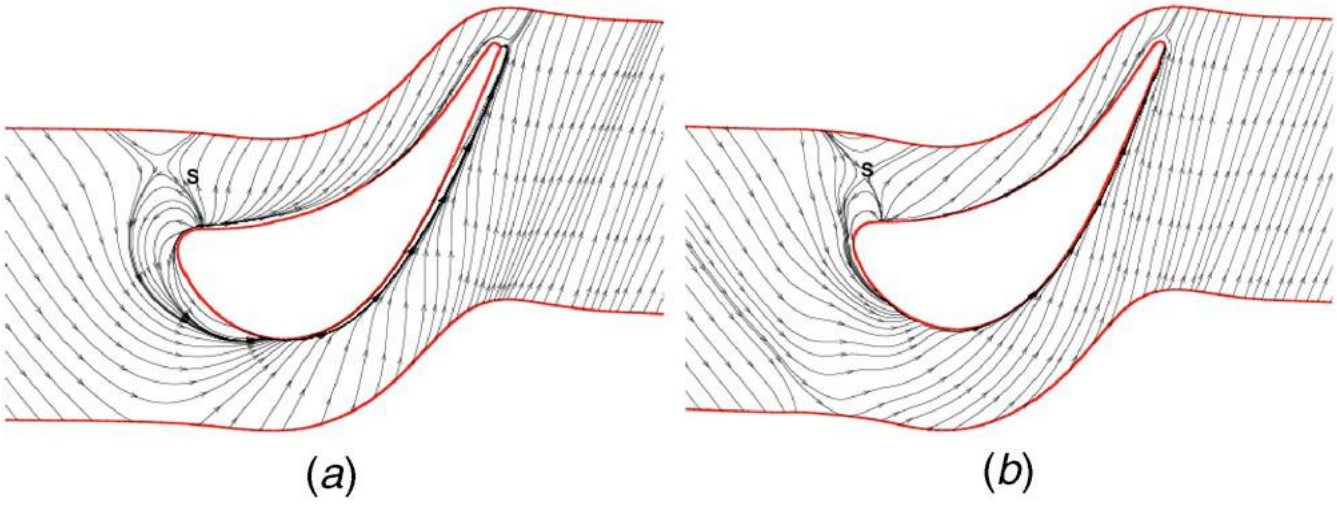

Fig. 2.12: Surface streamlines on the end wall: a) flat b)contoured end walls(Saha et al., 2008)

Three dimensional endwall contouring reduces the pitchwise pressure gradient near the endwall which reduces the chances of flow separation. Endwall contouring reduces the total pressure loss by the peak value get lower by 10% and mass averaged loss value is reduced by 3.2%. Moreover the strength and size of secondary passage vortex also decrease.

The secondary losses in low aspect ratio high pressure turbine are very prominent. **Sonoda et al. [2009]** use axisymmetrical end wall contouring method for reducing the secondary losses in high pressure turbine having low aspect ratio. They investigate the effect of three types of end wall contouring: 1) only hub contour, 2) only tip contour, and 3) hub and tip contour on the aerodynamic performance of the ultralow-AR transonic turbine IGV. Comparison of experimental and CFD result is done and much agreement is found. A special probe is used for the total pressure measurement. This total pressure is compared with CFD simulated result.

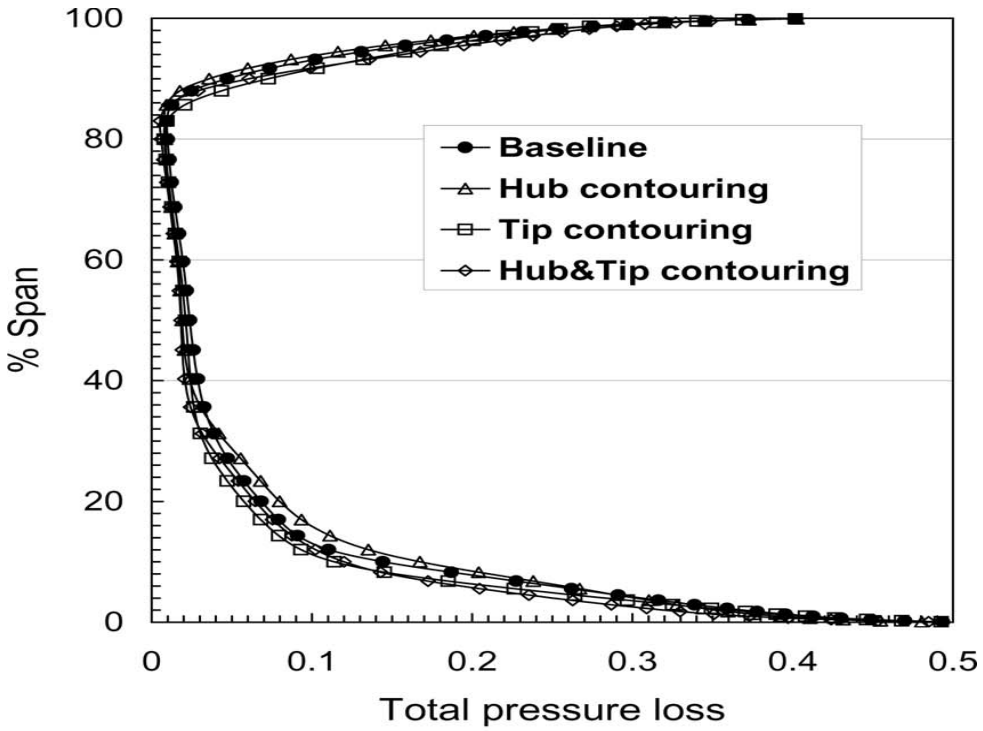

Fig. 2.13: Spanwise distribution of loss (Sonoda et al. 2009)

Fig. 2.13 shows that end wall contouring reduce the total pressure loss. Moreover hub contouring, the tip contouring, and the hub and tip contouring all reduce the mass averaged overall loss by 4%, 5%, and 10%, respectively, as compared to the base line.

Knezevici et al. [2010] measured the secondary losses in turbine cascade with non axis- symmetric end wall contouring in a low-speed linear cascade test facility. It is observed that the overall secondary loss decreases in contoured geometry but from the wall to 10% of the span contouring increases the secondary loss. Then the loss remain equal for next 6% and finally from 16% to 34% of the span appreciable loss reduction is achieved in the contoured geometry. The reduction in loss was attributed to a reduction in secondary kinetic energy and improved outlet flow quality.

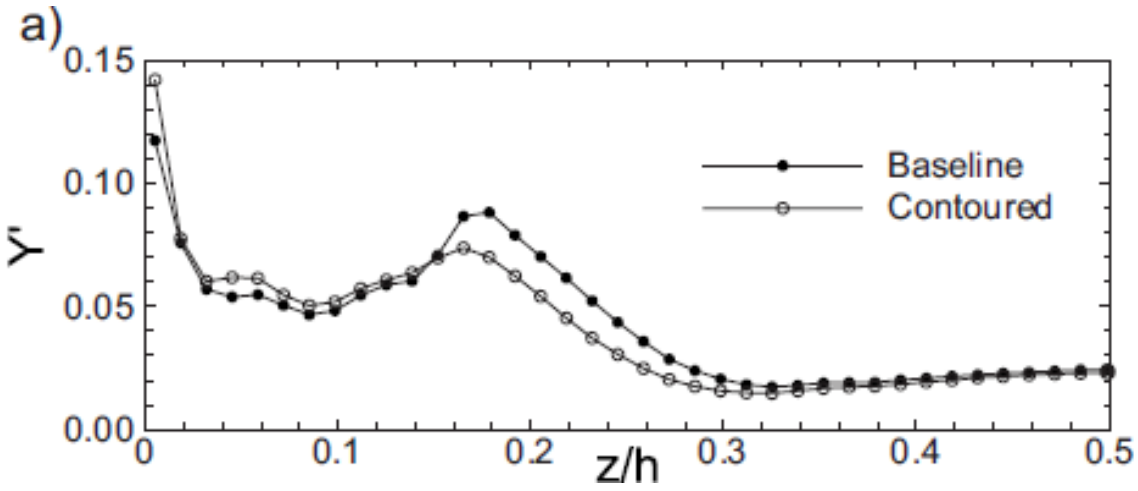

Fig. 2.14 : Pitch wise mass averaged pressure loss cofficient result for 140% axial chord measurement plane *(Knezevici et al. 2010)*

Torre et al. [2011] described a new flow mechanism for the reduction in secondary flows in low pressure turbines using the benefit of contoured endwalls. They used the contoured endwall to modify the formation of the horseshoe vortex, which are the three-dimensional complex vortices formed due to flow separation because of some obstacle in the flow direction. CFD analysis, with the nonlinear solver known as Mu^2s^2T had been

employed. Turbulence effects are modeled using the k-ω model. The secondary flows happen to be confined closer to the wall and also weaker for the case of the contoured endwall. As a consequence, a reduction of 20% in the mixed-out endwall losses and a reduction of 72% in SKEH are obtained.

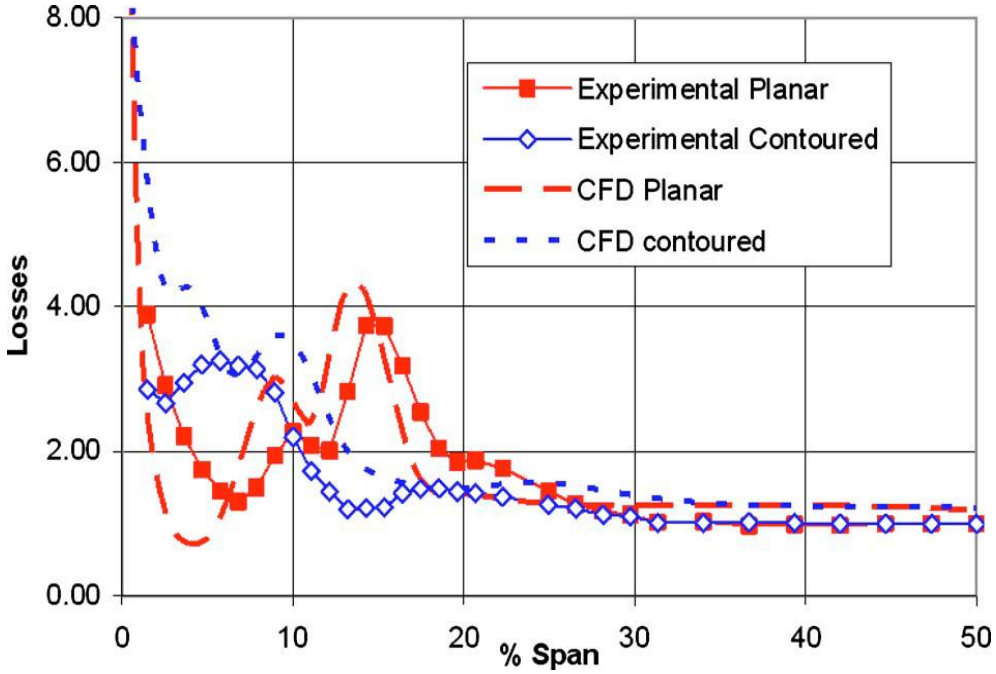

Fig 2.15: Measured and calculated pitchwise mass averaged gross stagnation pressure loss coefficient *(Torre et al.2011)*

2.4.2 Leading Edge Modifications

Sauer et al. [2001] performed experiment to validate the fact that leading edge modification reduces the secondary losses in the turbine cascade. They used popular T106 cascade as baseline profile and modify their leading edge by introducing the bulb at the leading edge which increase the leading edge diameter and named them T106/1, T106/2 and T106/3 by increasing its radius by a small amount lengthwise it extends for b_o= 5 mm staying constant. From there it merges within b_o = 15 mm into the reference profile.

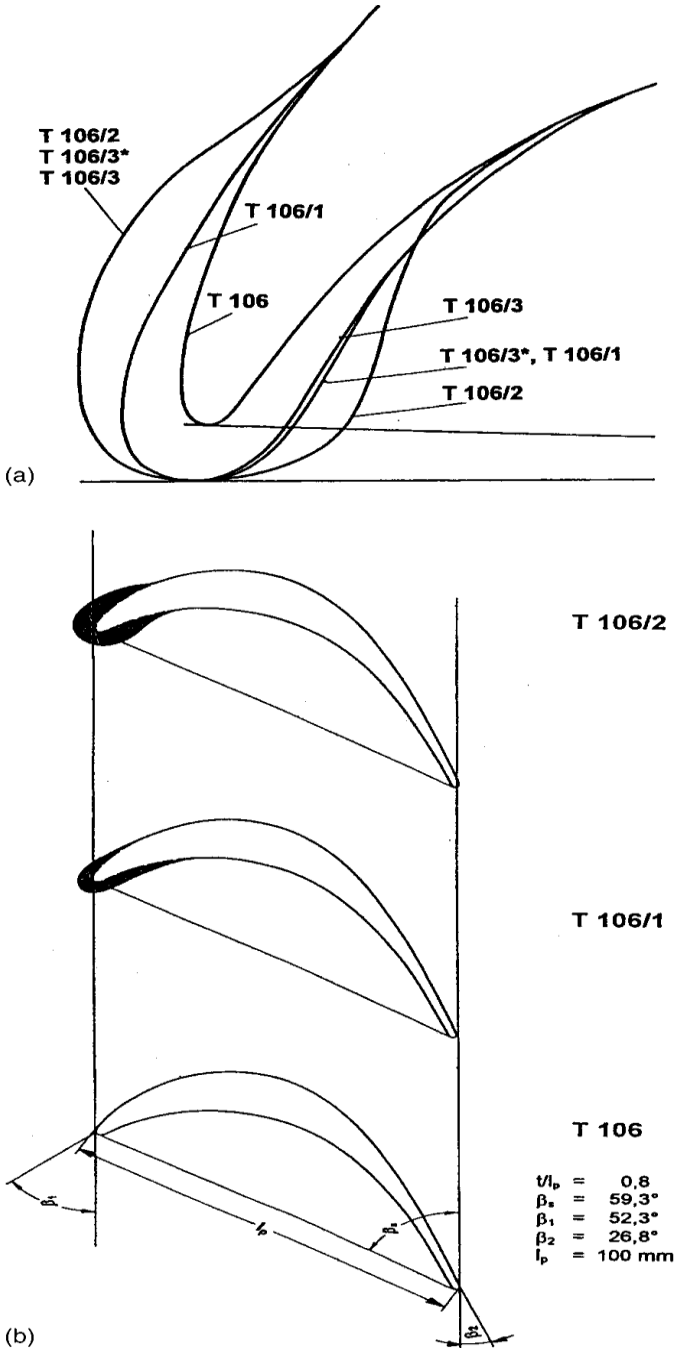

Fig. 2.16: a) T106 Cascade data (equal blading for each modification) and (b) T106 profile and the modification (leading edge endwall bulb) (Sauer et al. 2001)

Leading edge bulb in the endwall region intensifies the suction side horse shoe vortex. It interacts with the counter rotating passage vortex moving that away from the suction side, resulting into decrease in secondary flow losses. The endwall loss could be lowered by 47 percent from originally 4.5 percent to 2.39 percent for configuration T106/3.

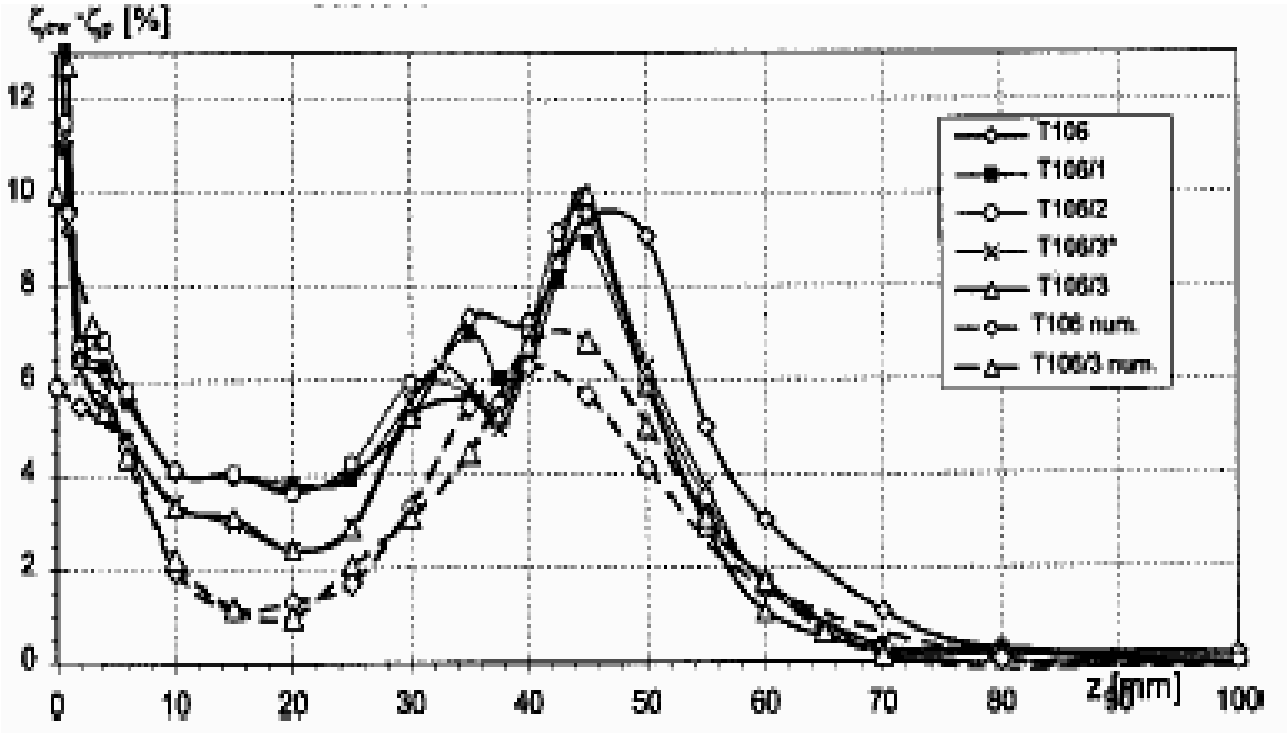

Fig. 2.17: Span wise endwall loss distribution (Sauer et al. 2001)

In 2001 Brear et al. concluded the use of thin solid blades in the modern air craft engine as these blades are relatively in expensive. But in the thin blade profile separation bubble often occur near the leading edge of the blade. This is known as pressure surface separation and leads to increased profile loss. So Brear et al. in [2002] tried to reduce this pressure surface separation. They used four types of blade profile A, B, C and D which were having same suction surface and pitch. Blade A was used by Brear in 2001 and all other blades were modification of blade A. Blade B was havind uniform span but thicker than Blade A. Blades B and C were same as blade A in the central third of span, but are blended out to a thicker profile at the endwalls. Blade C has the same profile at the endwall as blade D, while blade B is thinner at the endwalls as shown in Fig. 2.18.

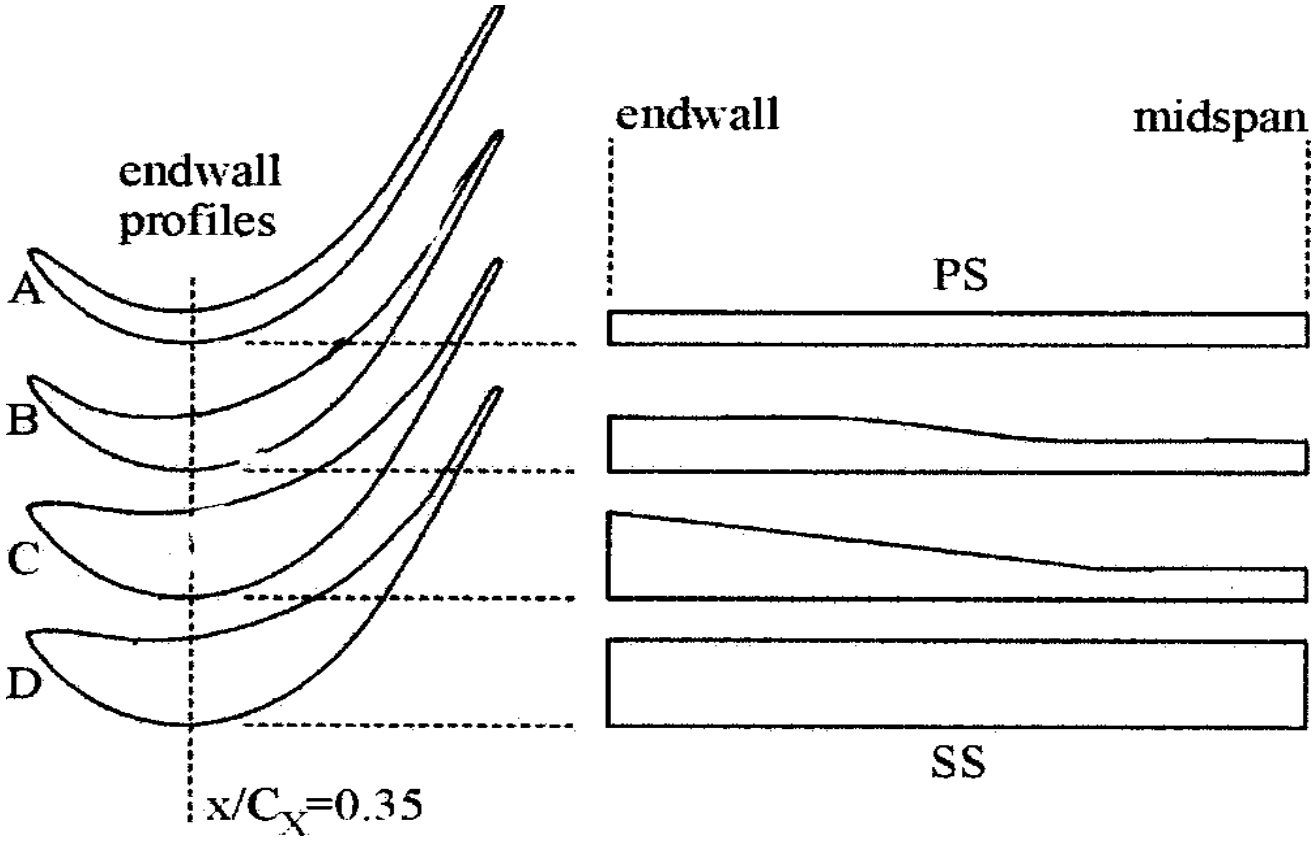

Fig. 2.18: Endwall and sectional profiles of blades A, B, C, and D (Brear et al. 2002)

It was observed that Blade A and D have same exit yaw angle and hence same loading at the mid span. Moreover as the Blade C and D fall between blade A and D and have the uniform span so Blade C and D had also same loading. It was also observed that variation of pressure surface geometry (as done for Blade D) had not affect the profile loss much and hence it was concluded that added thickness of Blade D around midspan at 0 deg incidence did not improve the aerodynamic performance in comparison to the increased cost of manufacturing. This also supported the finding of Brear et al. in 2001.

They found out the mass averaged values of yaw angle, loss coefficient and profile loss coefficient as shown in Table 2.2.

Table 2.2: Mass-averaged results of blades A, B, C, and D at 125 percent Cx from experiment and numerical predictions (Brear et al. 2002)

	α_3 (°)		Y_3		Y_P	
	expt.	**pred.**	**expt.**	**pred.**	**expt.**	**pred.**
A	62.3	62.4	0.0450	0.0347	0.0282	0.0250
B	62.4	62.6	0.0418	0.0334	0.0286	0.0248
C	62.5	62.8	0.0404	0.0312	0.0282	0.0245
D	62.5	62.7	0.0403	0.0300	0.0281	0.0244

Using the aft loading principle which states that for a given blade loading, it is best to impose the largest blade-to-blade pressure gradient in regions that are most resistant to cross-passage transport i.e., regions where the flow has highest momentum, it was concluded that secondary flow strength and loss can be reduced by increasing the momentum of fluid near the end wall and it can be done by increasing the thickness at the pressure surface. So increasing the blade thickness at the pressure surface decrease the strength of secondary flow by increasing the momentum near the wall.

Shih et al. [2003] observed effects of leading-edge airfoil fillet on the flow in a turbine-nozzle guide vane due to turbulent driven secondary flow. They used three types of configuration a) no fillet (baseline), b) a fillet whose thickness fades on the airfoil, c) a fillet whose thickness fades on the endwall. It has been found that a pointed/sharp fillet on the leading edge of the airfoil as shown in Fig. 2.19 (a) could reduce or eliminate horseshoe vortices. But ‘‘pointedness and sharpness’’ of the fillet must be aligned with the stagnation flow. For rounded fillets, Fig. 2.19(b), it was found that intensity and size of horseshoe vortices increase with radius of the fillet. A bulb-type fillet as shown in Figure 2.19(c) is

intended to intensify horseshoe vortices on the suction side in order to reduce the pressure-side-to-suction-side secondary flow.

The increased size of the stagnation zones on the endwalls about the airfoil's leading edge lowers the flow speed and velocity gradients there, which in turns reduces turbulence production. This could be one of the main reasons for the reduced aerodynamic loss and surface heat transfer on the endwall.

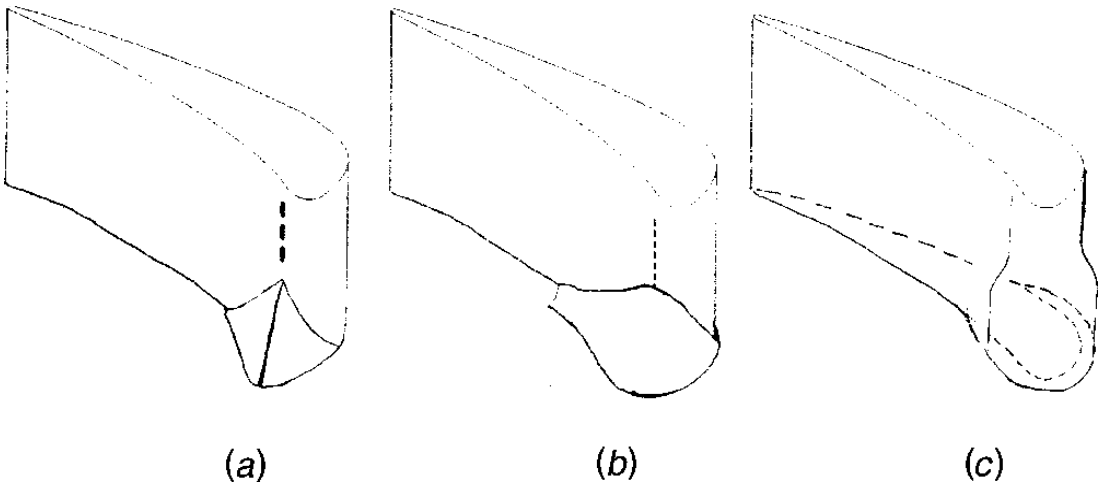

Figure 2.19: Basic leading-edge fillet geometries a) sharp/pointed, b) rounded, c) bulb type (Shih et al. 2003)

Benner et al. [2004] investigated the effect of leading edge modification on turbine cascade losses. They selected two blade configurations LS2 and LS3. LS2 is a baseline aerofoil and LS3 is an aerofoil having leading edge diameter approximately twice of LS2 leading edge. The modified aerofoil LS3 has slightly smaller stagger angle and hence more aft loaded than LS2. Measured and mixed-out secondary losses were higher for LS2. Stronger streamwise vorticity, passage vortex and secondary kinetic energy were accounted as the reason for higher secondary loss in LS2. Moreover stronger vortex close to the suction surface and endwall produce thinner boundary layer larger edge velocities, which increase the loss production near the endwall. . In addition, the stronger passage

vortex seemed to induce a stronger separation vortex on the suction side of the aerofoil. The higher secondary velocities in the region where these two vortices interacted resulted in higher downstream mixing losses for the baseline aerofoil.

The greater size and strength of the passage vortex for the baseline aerofoil is attributed to this aerofoil's front-loaded pressure distribution and the resulting stronger upstream pressure field as shown in Fig.2.20 Moreover the profile loss was higher for LS3 because of greater leading edge geometry. They concluded that diameter of leading edge has minor affect on secondary losses but type of loading primarily affects the secondary loss. Forward loading increases the secondary losses.

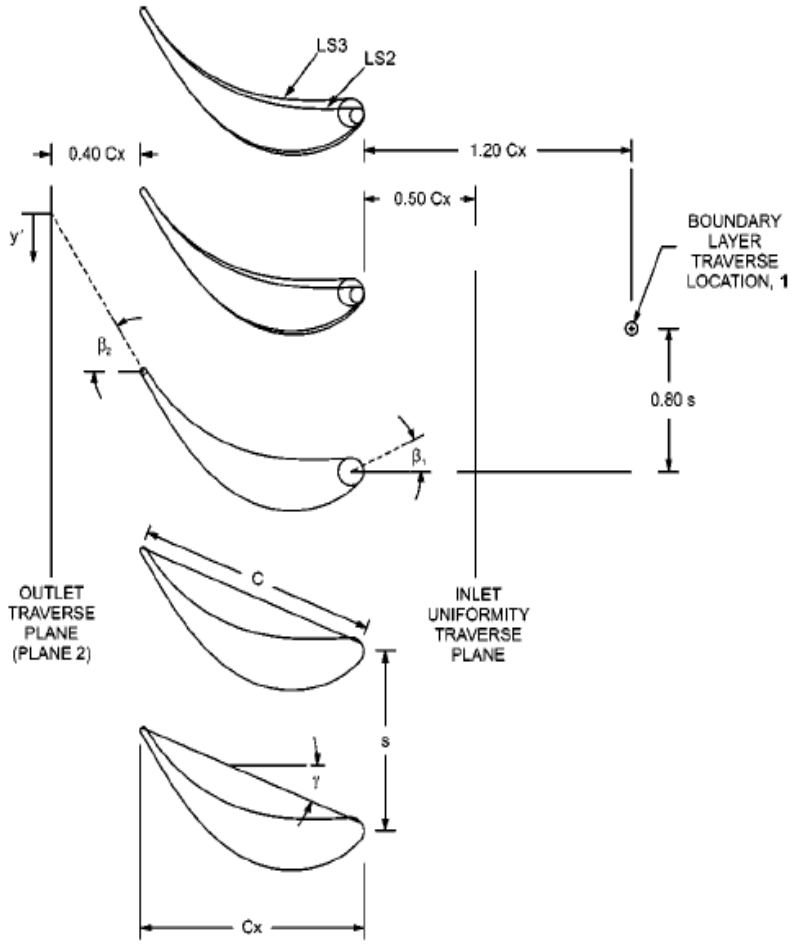

Fig.2.20: Cascade geometry for LS2 and LS3 and measurement location (Benner et al. 2004)

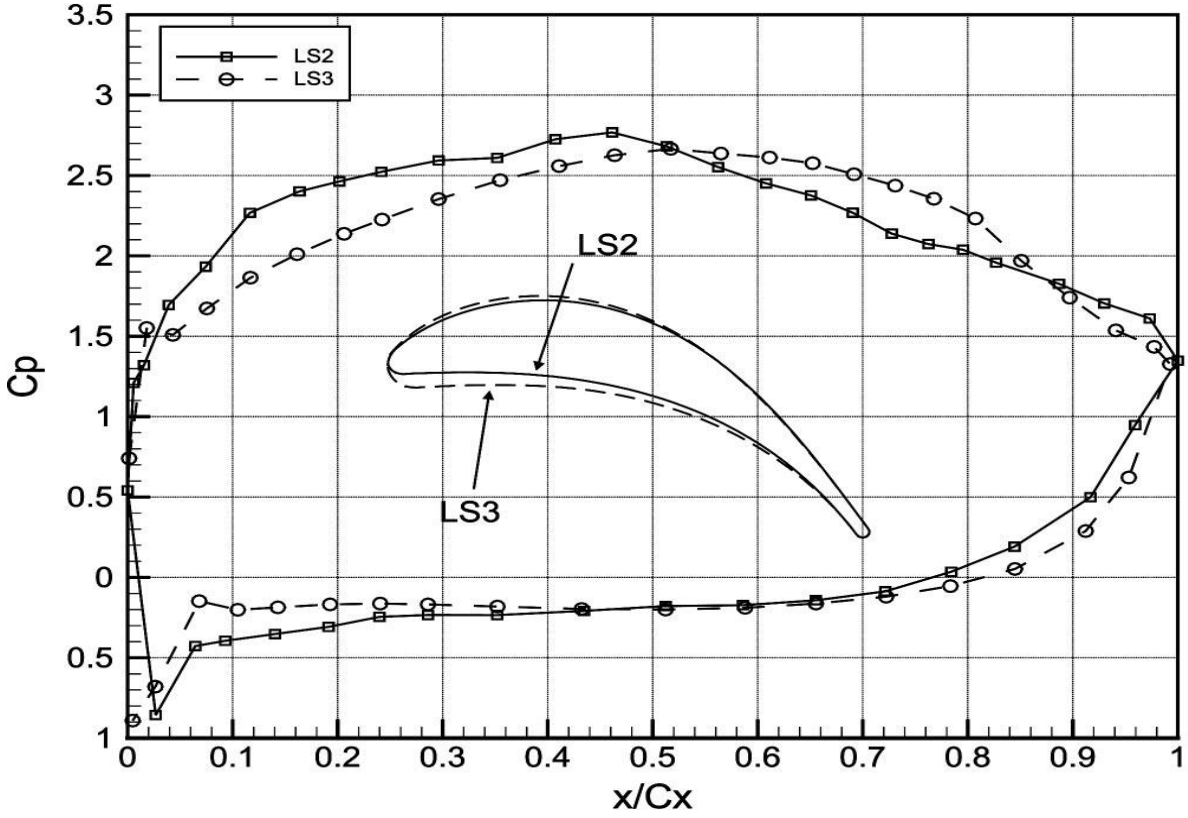

Fig. 2.21: Measured midspan surface pressure distributions for LS2 and LS3 at design incidence (Benner et al. 2004)

Mahmood et al. [2007] studied the secondary structure in a blade passage with and without leading edge fillet. Fillet can be defined as thickening of the blade profile at the leading edge near the endwall. G. I. Mahmood et al. measured the velocity and pressure at a constant Reynolds number of 233,000 based on the blade chord and the inlet velocity. They designed two solid wooden blades with corresponding fillet and named them fillet1 and fillet 2. Fillet given to fillet1 was having a linear profile while fillet2 was given a parabolic profile. In the early stages of the development of the secondary flows, the fillets were seen to reduce the size and strength of the suction-side leg of the vortex with associated reductions in the pressure loss coefficients and pitch angles. Further downstream, the total pressure loss coefficients and vorticity show that the fillets lift the passage vortex higher above the endwall and move it closer to the suction side in the

passage. Near the trailing edge of the passage, the size and strength of the passage vortex is smaller with the fillets, and the corresponding reductions in pressure loss coefficients extend beyond the mid-span of the blade. It was observed that fillet 2 is having a better capability of reducing the pressure loss coefficient.

Korakianitis et al. [2010] has proposed a direct design method based on specifying blade surface-curvature distributions so as to minimize the chances of flow separation. Korakianitis in his earlier work prescribed a method of blade designing with a continous slope of curvature for getting better aerodynamic performance. Later on in 2010 Korakianitis and. Hamakhan modified the proposed direct design method in the vicinity of the leading edge. They prescribed a leading edge having a shape of circle or ellipse. A polynomial function is defined as a thickness distributor in relation to the parabolic construction line, to join the leading edge with the main part of the blade surface, resulting in continuous curvature and slope of curvature at these crucial locations. With this modified direct design method they designed three blades B1, B2 and B3 using fluent solver.

For all three blades the solution have been obtained for design point conditions as well as for incident angles of 0°, - 5°, +5°, -10°, and +10°. At design point conditions blade B1 exhibits perfectly acceptable behavior, without any leading-edge flow-disturbances at the joining points of the blade surface with the leading edge circle. At +5° a small disturbance is shown on the suction surface at the location of joining the leading edge circle with the blade surface. At -5° a small acceleration–deceleration region is shown on the pressure surface at the location of joining the leading edge circle with the blade surface. These flow-disturbances are made worse at +10°, and -10°. These disturbances at off-design conditions are progressively improved in blades B2 and B3 by small changes in the blade surface- curvature distribution.

Table 2.3: Stagnation pressure loss *(Korakianitis et al. 2010)*

Blade Name	Design And Off- design Conditions				
	-10	-5	0	+5	+10
B1	0.002430	0.002450	0.002480	0.002518	0.002560
B2	0.002424	0.002446	0.002474	0.002508	0.002552
B3	0.002357	0.002404	0.002433	0.002467	0.002515

The prescribed surface curvature blade design technique smoothen the boundary layer flow and hence minimize the flow separation with a reduced pressure loss.

Lei et al. [2011] analyze the effect of leading edge modification on the secondary loss. They use vortex generator for introducing counter rotating vortex which oppose the passage vortex and hence reduce the secondary flow losses. They fixed half delta wing at the cascade end wall for generating the stream wise vortex. For finding out the optimum position of the vortex generator they used four different cascade configurations.

The delta wings were fixed to the end-wall at 60° to the axial direction to maintain an incidence angle of 10°. The four different configurations were: 1) the cascade with no vortex generator (NV), 2) with vortex generator near the suction side surface (SS-V), 3) with vortex generator near the pressure side surface (PS-V) and4) with vortex generator at the middle of the passage (MID-V).

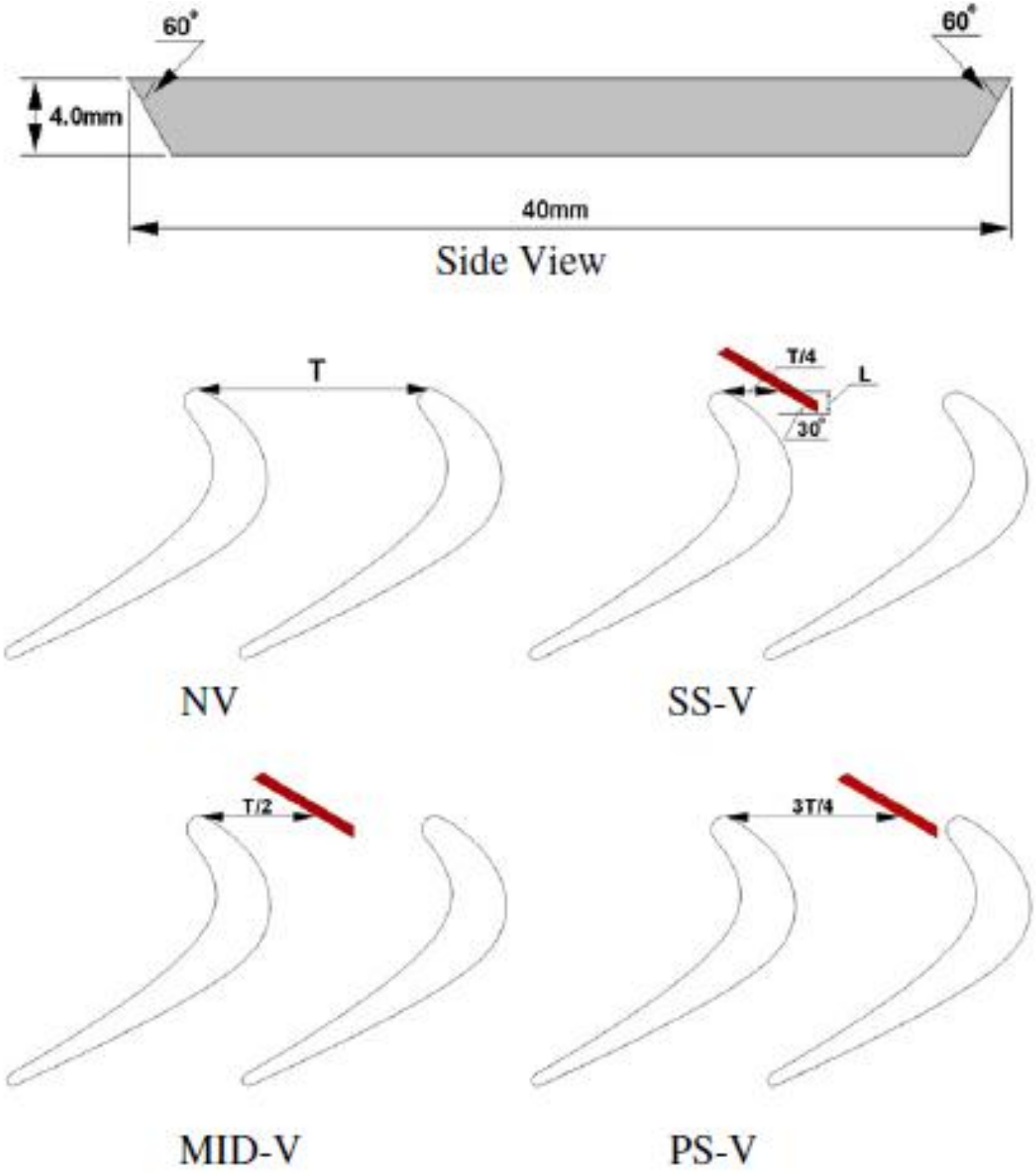

Fig. 2.22: Schematic diagram of the delta wing geometry and delta wing installation positions *(Lei et al. 2011)*

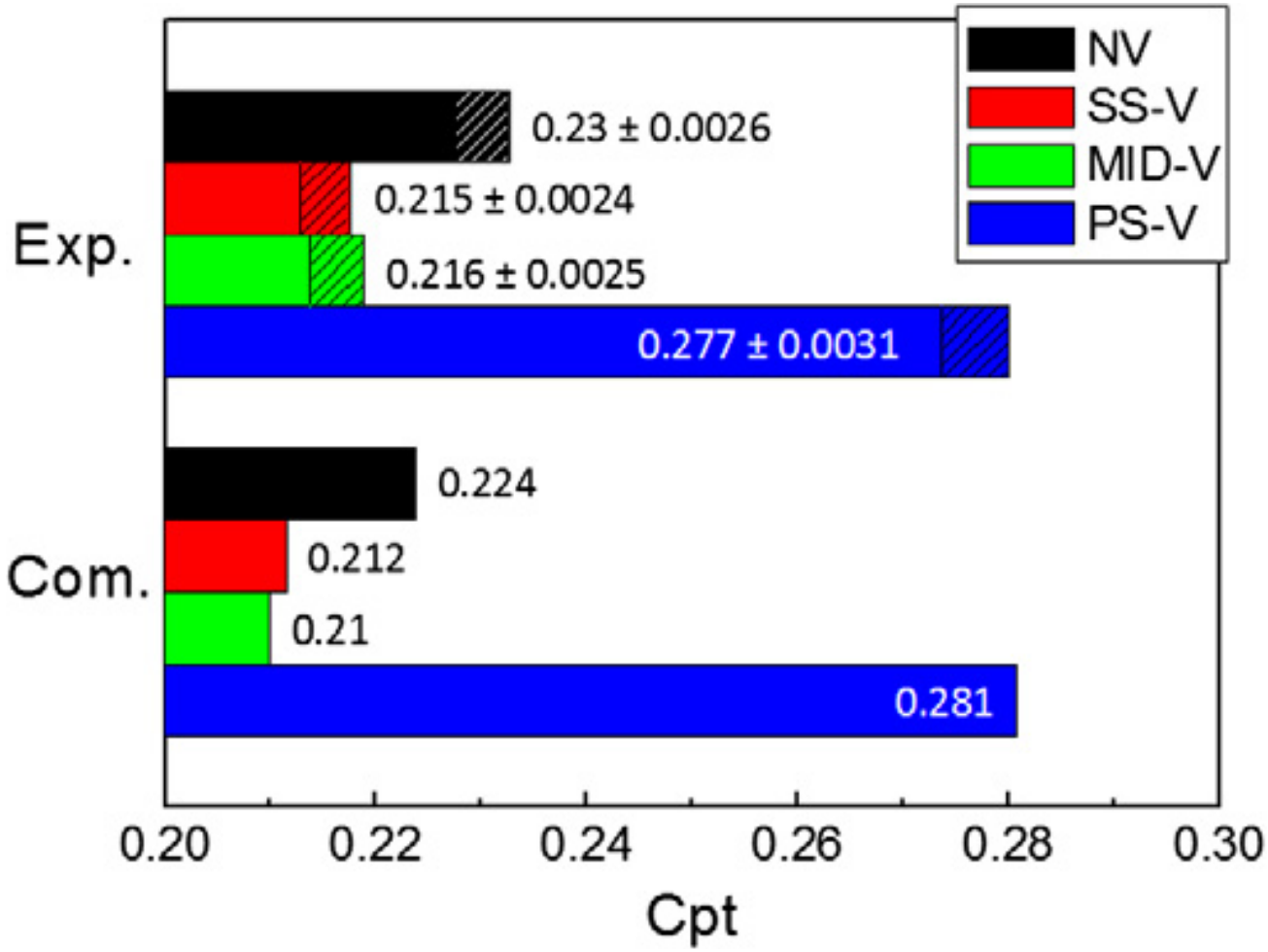

Fig.2.23: Comparison of mass-averaged stagnation pressure loss at the cascade exit *(Lei et al. 2011)*

The computation is performed using commercial CFX software and it can be seen that experimental and computational data are in agreement with each other. They conclude that in SS-V configuration, the vortex generator is near to the suction side. Here close to the endwall sreamwise vortex is stretched because of accelerated flow so by Kelvin's calculation theorem, the streamwise velocity must increase. This sreamwise vortex meets the passage vortex and resulted into decrease in stagnation pressure loss. Whereas in PS-V configuration vortex generator is near the pressure side. The leading edge of the delta wing is quite close to the blade leading edge. When the inlet flow passes the delta wing, it turns towards the end-wall rolling up into a strong secondary vortex due to the

potential field effect of the blade leading edge. The secondary vortex rotates in the same direction as the pressure side leg of the horseshoe vortex (HPV). Therefore the passage vortex strength increases remarkably. And hence it is concluded that vortex generator should not be fixed near the pressure side as it would strengthen the secondary vortex, but fixing the vortex generator near the suction side can reduce the secondary loss. Moreover installation of vortex generator induces some additional mixing losses but overall loss is reduced.

Zhang et al. [2011] also investigated the effect of modifying leading edge geometry. They optimized the Hodson–Dominy (HD) blade and found out the change in total loss in the cascade using Large Eddy Simulations (LES) and Reynolds Average Navier–Stokes (RANS) simulations.

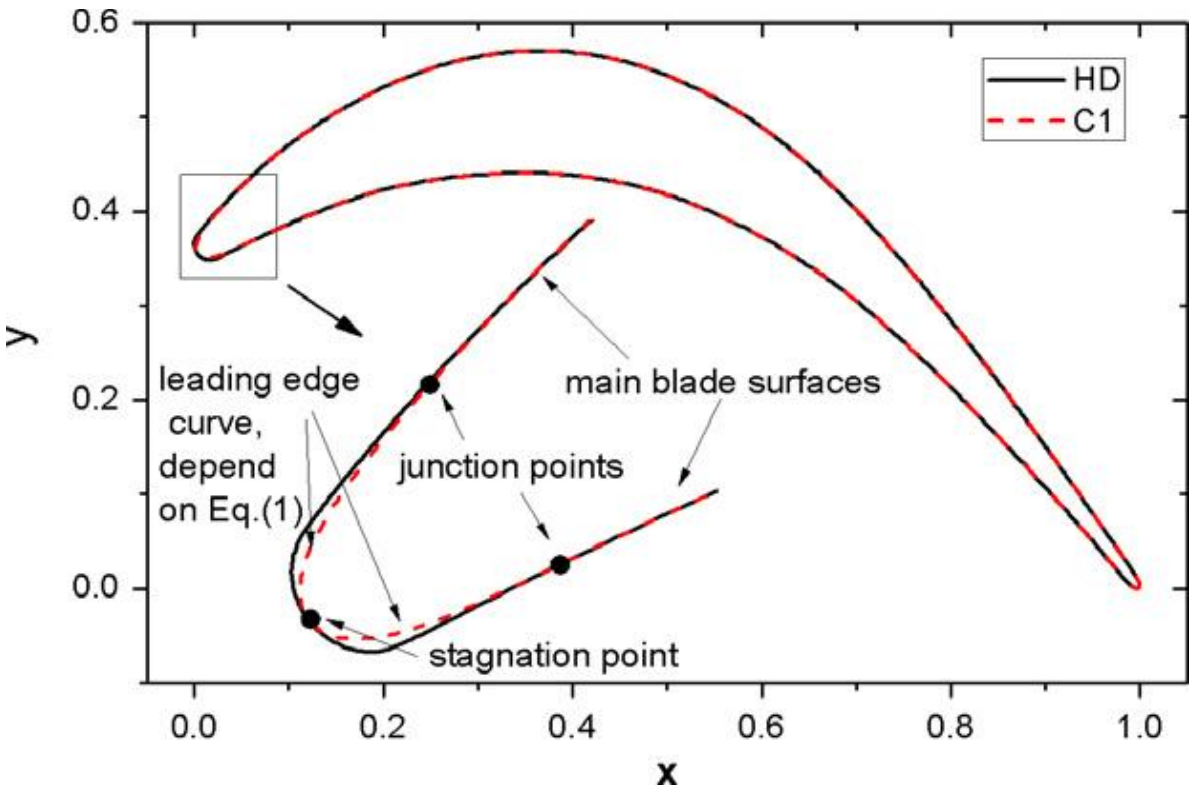

Fig. 2.24: Original and redesigned profiles *(Zhang et al., 2011)*

By redesigning the HD blade suction side pressure spike is restrained and separation bubble is completely removed. The dissipation coefficient near the suction side leading edge is very large causing nearly 18% loss in HD blade. Blade redesigning cut down the loss to 2/3. Middle chord loss and trailing edge loss are declined about 6.25% and 11.8%, respectively. Finally the total loss decrease by 10%.

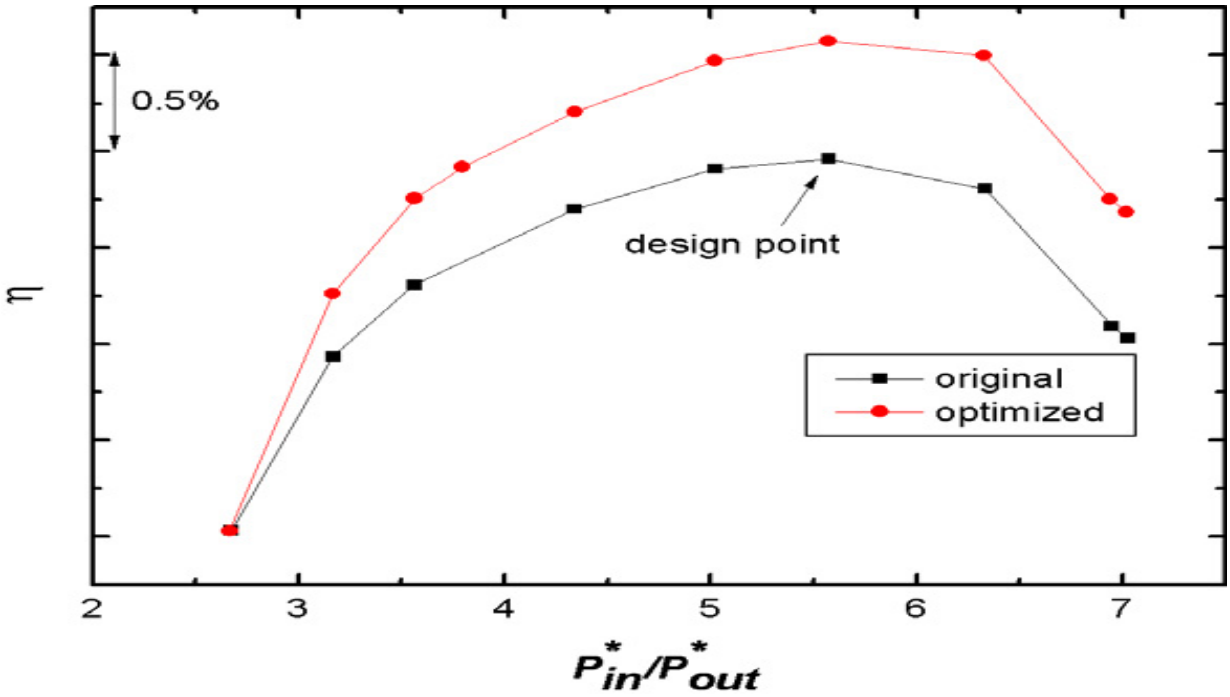

Fig. 2.25: Efficiency characteristic for original HD and optimized blade (Zhang et al., 2011)

2.5 Parameters affecting the Secondary Flow

Pullan et al. [2006] analyzed the secondary flow and loss caused by the blade row interaction. In addition to the passage vortex in the rotor hub, additional vortices were observed away from the endwall. The presence of these additional vortices had been attributed to the stator exit flow field. They concluded that the wake with steep gradients of absolute total pressure normal to the axisymmetric stream surface of primary flow was responsible for the rotor exit vortices. Comparison of steady and unsteady simulation was

also done using the Denton's solver. Additional loss of 10% was observed in unsteady simulation as compared to steady simulation because of three reasons:

i) The mixing out of the inlet flow.

ii) The unsteady interaction of the inlet flow with the blade row boundary layers.

iii) The mixing associated with the rotor secondary flows over and above that of the rotor secondary flows in the steady calculation.

Chaluvadi et al. [2003] investigated the three dimensional flow field in the high pressure axial flow turbine. The flow field is investigated in a low-speed research turbine using pneumatic and hot-wire probes downstream of the blade row. To further understand the flow field steady and unsteady numerical simulation was also done. It was observed that most of the loss over the span was associated with the blade wake, but because of the secondary flow in the hub and casing additional loss was observed there. The simulated result was validated properly with the experimental result.

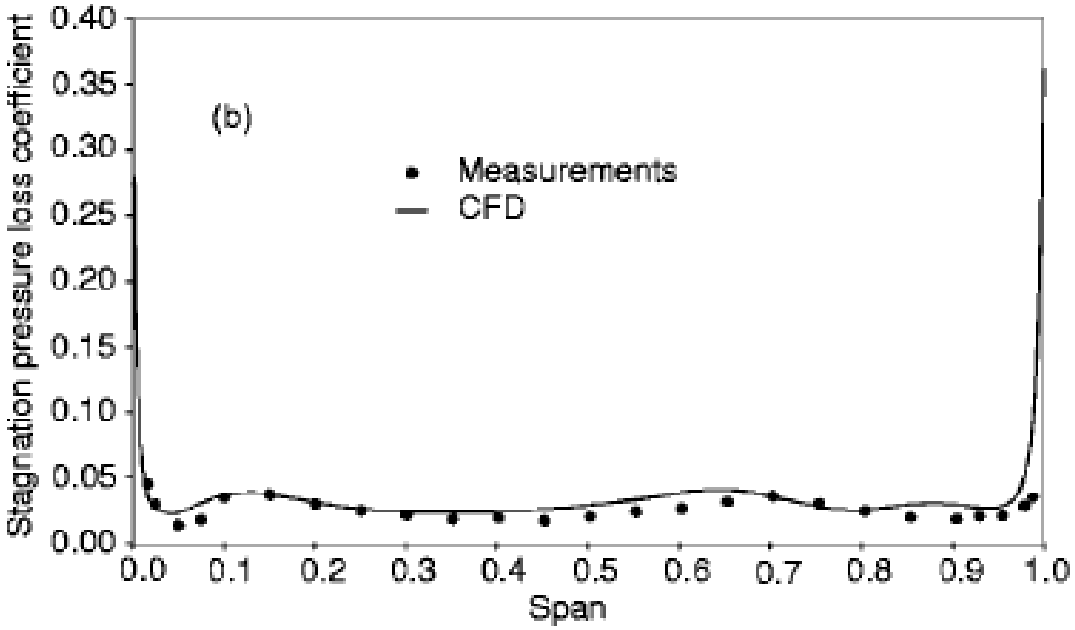

Fig. 2.26: Variation of stagnation pressure loss with the span at the stator trailing edge (Chaluvadi et al. 2003)

They also proposed a new kinematic model for calculating loss generation which is shown in Fig. 2.27. They defined a term stretching ratio which is the ratio of exit vortex filament length to the inlet filament length.

$$SR = \frac{DQ}{AP} = \frac{\cos(\theta_2)}{\cos(\theta_1)} \frac{\cos(\gamma_1 + \theta_1)}{\cos(\gamma_2 + \theta_2)}$$

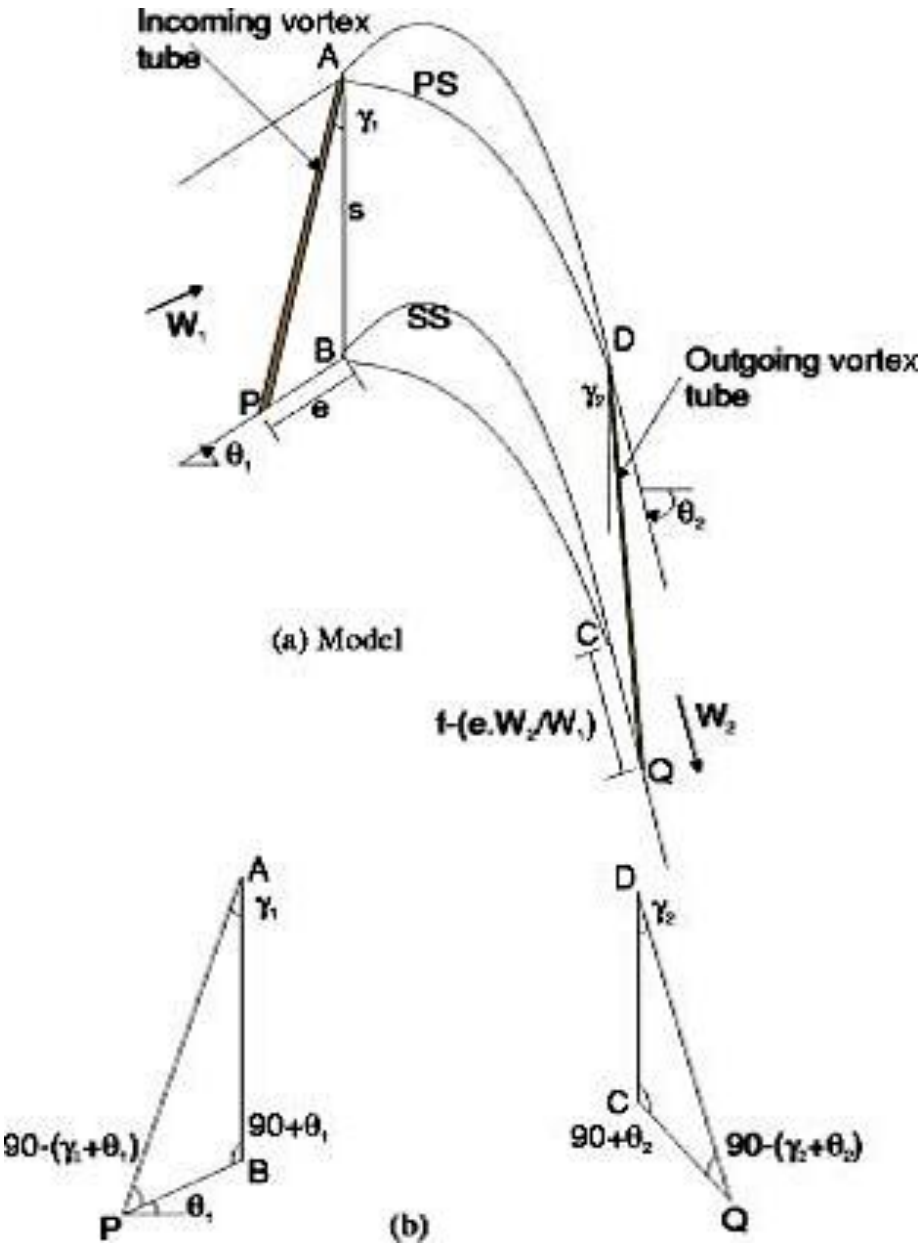

Fig. 2.27: Kinematic model illustrating the vortex transport through a turbine blade passage (Chaluvadi et al. 2003).

Using this model they showed that secondary kinetic energy is increased with stretching ratio. It was also observed that secondary kinetic energy is a weak function of stage loading but it increases with reduction in flow coefficient. Hence depending on the ratio of secondary flow losses to stage loss, additional loss generated due to passage vortex transport. Hence turbine loading conditions can be easily decided using this model.

Porreca et al [2008] studied the effect of optimized shroud design on the aerodynamic performances of the blade. In the unshrouded blade design, the blade tip is extended toward the rotor casing while keeping a reasonable gap between rotating and stationary parts. But this type of design leads to increased leakage loss. Shrouding the blade seal the gap and ensure better aerodynamic performance but this simultaneously increases the complexity of cooling arrangement and blade/disk centrifugal stresses. Hence partial shrouding is can be done in order to set a layoff between the fully shrouded and unshrouded design. They analyzed three designs of blade. Full shroud (FS) configuration, partial shroud (PS) configuration, and enhanced partial shroud (EPS) geometry

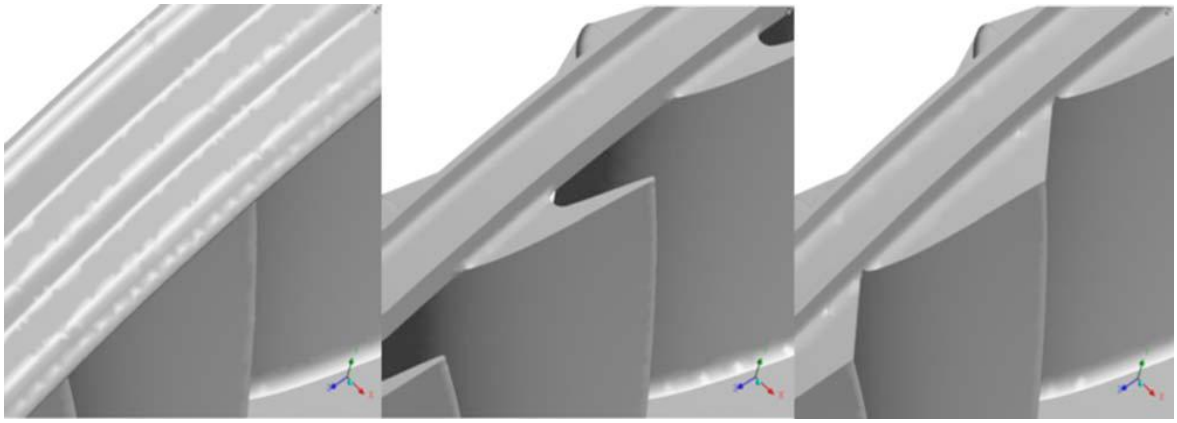

Fig. 2.28: Schematic of the shroud geometry: FS (left), PS (middle) and EPS (right) (Porreca et al. 2008)

For all three configuration numerical simulation was done by using ANSYS CFX solver. No pressure reduction was observed in FS case corresponding to tip leakage vortex because boundary layer is sucked into the leakage path which weakens the passage vortex. But in PS and EPS significant pressure reduction was observed at 80% span. In PS case this pressure reduction was attributed to the tip leakage vortex which originated because of the uncovered region of blade of TE and expands on cavity region, this decrease the aerodynamic performance by 1.1%. In EPS this pressure reduction occur because of the growth of passage vortex downstream of shroud platform and then mixing with the leakage vortex. It was observed that EPS has only 0.5% penalty on the aerodynamic efficiency as compared to 1.1% penalty in case of PS. This happen because of enhanced mixing and stronger leakage vortex

Pullan et al. [2008] analyzed the effect of sweep on the axial flow turbines. When the stacking axis of the blade is not perpendicular to the axisymmetric stream surface in the meridional view of the turbine then sweep is introduced into the turbine. Sweep usually increases the mid span profile loss but tend to decrease the secondary loss. Graham Pullan et al. take two type of cascade. One is unswept and is denoted as H and other is highly swept at $\lambda = 45°$ known as HS.

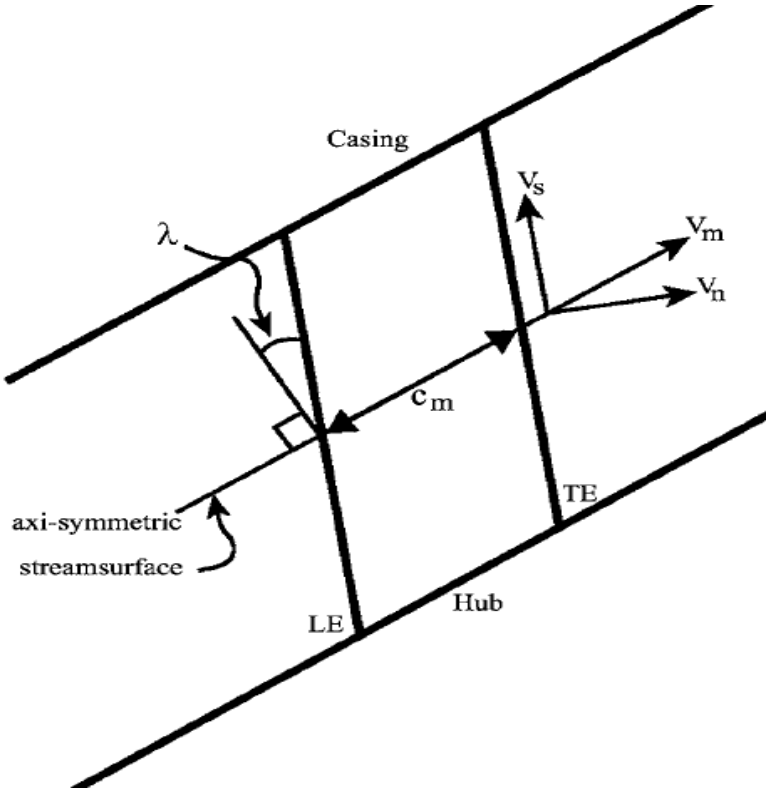

Fig.2.29: Meridional view of blade to define sweep angle λ (Pullan et al. 2008)

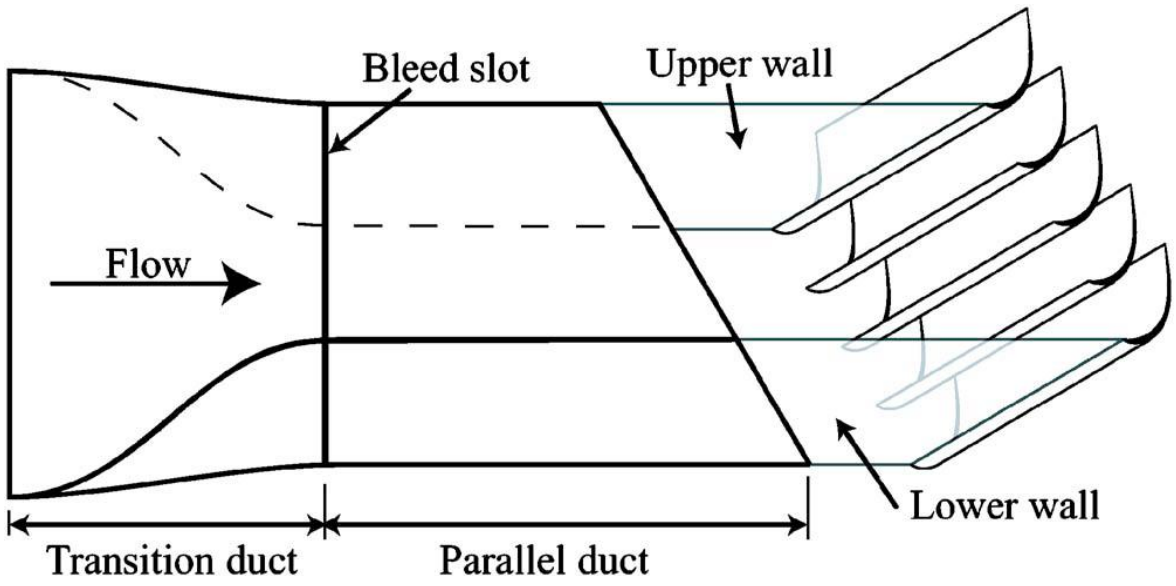

Fig. 2.30: Schematic of swept cascade blade HS, side view (Pullan et al. 2008)

The hub of blade HS generate secondary flows, which penetrates a smaller distance up the suction surface from the endwall. Here the sweep causes a delay in the cross flow because of two reasons. Firstly leading edge loading at hub is greatly reduced and

secondly the bulk motion of primary flow opposes the secondary flow leading to a reduction of 24% in secondary loss. Whereas at the casing of blade HS secondary flow is generated with a reduced end wall overturning at the row exit. Here the sweep encourages the crossflow by increasing the leading edge loading. However, once the inlet boundary layer has swept on to the suction surface, it is replaced on the endwall by irrotational primary flow, which arrives at the casing over the pressure side half of the passage. At this endwall, the measured secondary loss is 39% of that for Blade H.

So it is concluded that sweep decrease the secondary loss but increase the profile loss and hence a trade off is to be done between the secondary and profile loss with the sweep by varying the aspect ratio. Moreover sweep decrease the overturning at the casing of blade HS and hence create a more uniform flow at the downstream row. **Persico et al. [2009]** studied the effect of increasing the stator and rotor blade loading and by reducing the stator-rotor axial gap. Wake blade and vortex blade summary was prepared for the cases listed in Table 2.4.

Table 2.4: *Summary of the test cases (Persico et al. 2009)*

Case	rpm	I_S (deg)	x_{gap}/b_S
Nominal	6800	0	0.35
Case 0	6800	0	1.00
Case 1	6800	22	0.35
Case 2	5800	22	0.35
Case 3	6800	22	1.00

Higher stator loading (Case 1) increase the wake formation in hub region. This resulted into two counter rotating legs in the hub region of stronger intensity. Case 2 resulted into weak qualitative changes in wake formation but the intensity of rotor passage vortex is increased. This could be because of periodic reduction of endwall relative total pressure gradient and

of blade loading occurring when the inlet wake enters the rotor channel. For large radial gap as in Case 3 and Case 0, inspite of strong counter rotating vortices generated by stator, lower traces of stator-rotor interaction was found downstream of stage. But if the incidence angle is reduced as in Case 3, stator loading strongly affects the mixing process.

Holley et al. [2009] used oil film interferometry for predicting the shear stress in the turbine cascade. The mass average total pressure loss as a function of axial distance along the turbine cascade had been calculated by Langston in 1977.

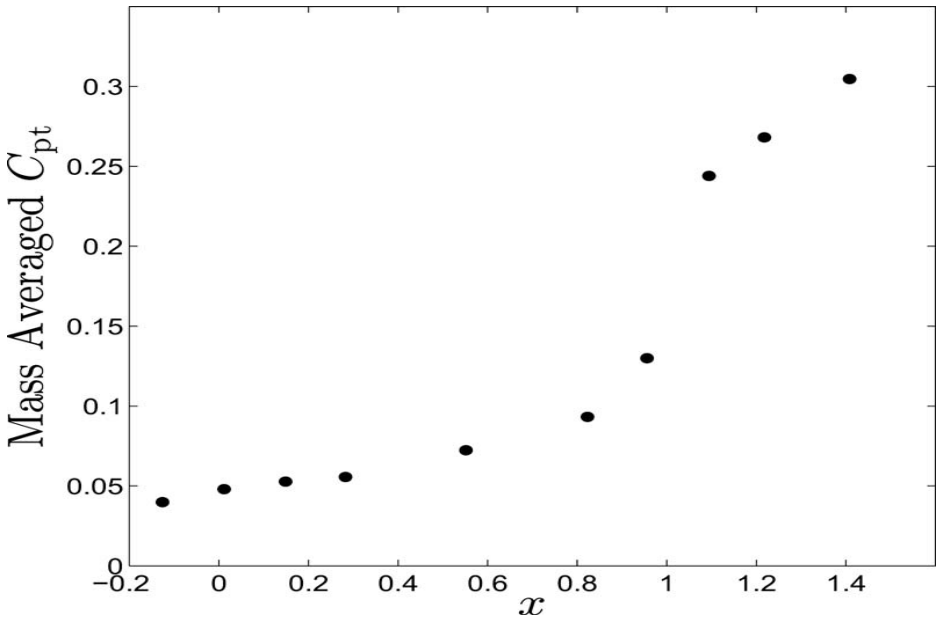

Fig. 2.31: Development of measured mass-averaged total pressure coefficient through the cascade *(Langston 1977)*

Skin friction was measured using OFI. Oil film on the surface of blade got thin due to shear stress. Knowledge of film thickness profile in the flow direction gave the measure of shear stress. They concluded that skin friction is the major cause of loss in the cascade. They validated their skin friction coefficient and pressure with the previous work and presented work provide a better understanding of the flow physics in the cascade.

Nho et al. [2012] studied the effect of blade tip shape on the secondary flow. The leakage between the blade tip and the fixed shroud leads to leakage vortex which increases the aerodynamic losses. They used 11 different types of blade profile to study the effect of variation in blade tip profile on total pressure loss and secondary flow using the 5 hole probe.

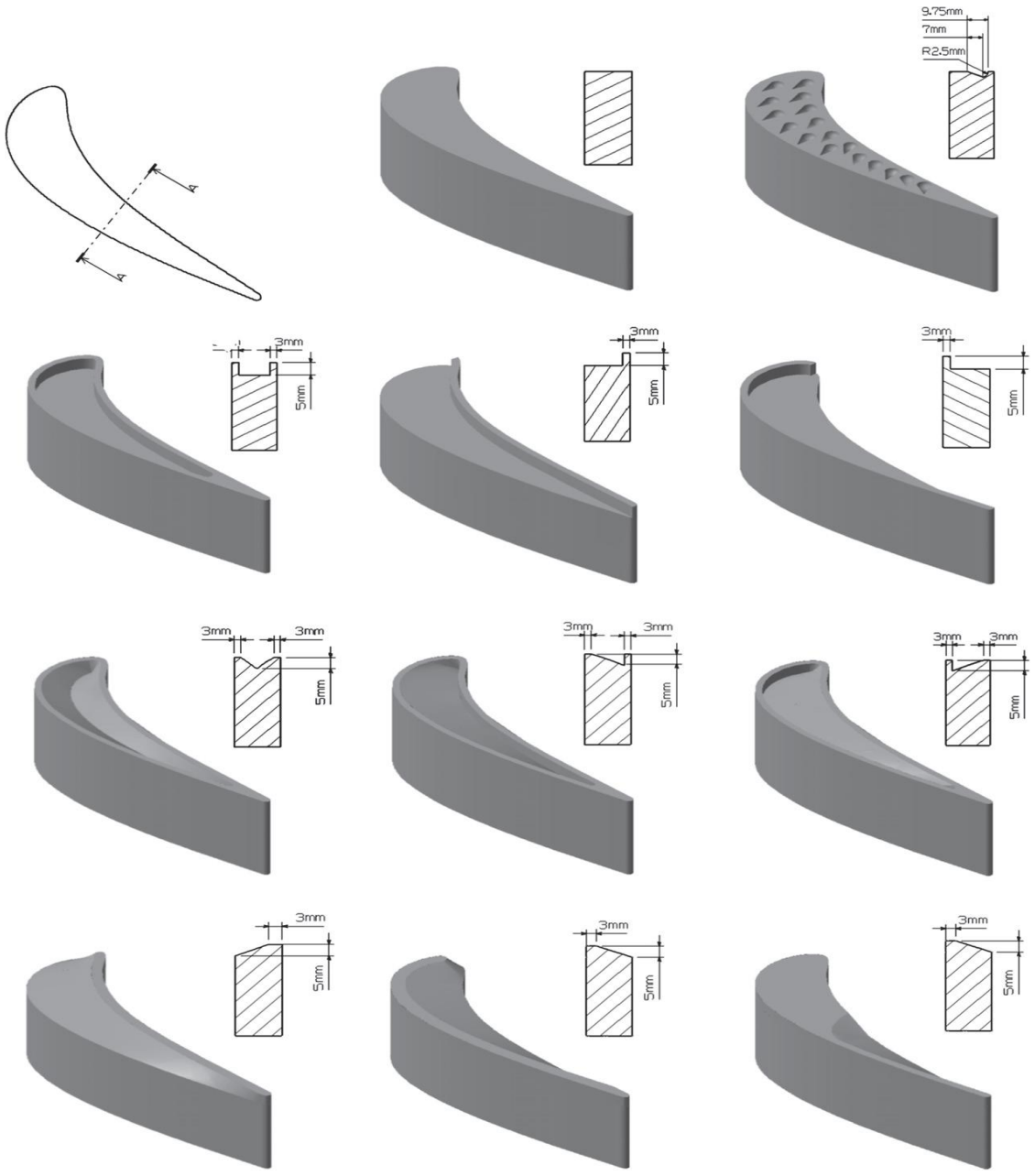

Fig. 2.32: Shape and cross sectional view of tested blade tips. (a) PLN, (b) DIM, (c) DSS, (d) PSS, (e) SSS, (f) GCL, (g) GPS, (h) GSS, (i) CPS, (j) CSS, and (k) TEC. *(Nho et al. 2012)*

The Fig. 2.32 shows 11 different blade tip namely:

PS: pressure side

SS: suction side

PLN: plane tip

DIM: dimpled tip

DSS: double squealer tip

PSS: pressure side squealer tip

SSS: suction side squealer tip

GCL: grooved along camber line tip

GPS: grooved along pressure side tip

GSS: grooved along suction side tip

CPS: chamfered from pressure side tip

CSS: chamfered from suction side tip

TEC: trailing edge chamfered tip

At zero tip clearance a clockwise rotating passage vortex A and an anti clockwise rotating trailing edge vortex B were observed. As the tip clearance is provided another counter clockwise rotating vortex C was observed which is known as leakage vortex. Leakage vortex weakens the passage vortex but overall pressure loss coefficient also increases. Increasing the tip clearance resulted into stronger leakage vortex and greater pressure loss coefficient.

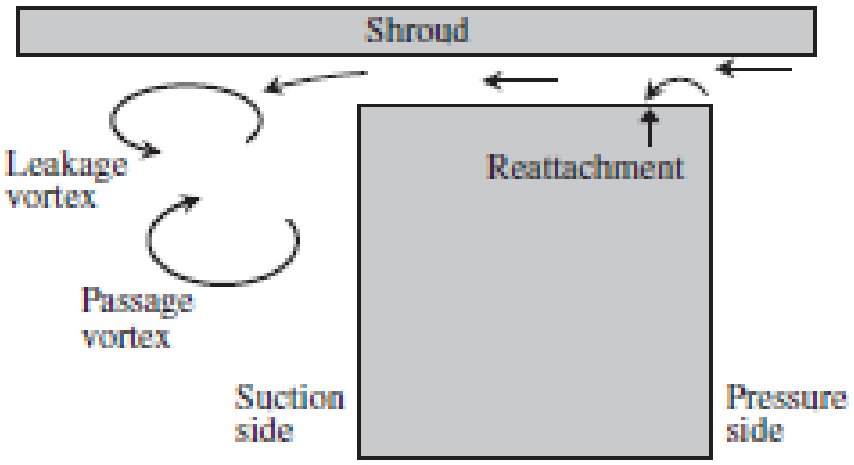

Fig. 2.33: Conceptual view of the flow near the plain tip region *(Nho et al. 2012)*

Young Cheol Nho et al. [2012] gave the following conclusions:

i) Leakage, passage and trailing edge vortex were observed on the cascade downstream. Leakage vortex rotates in opposite direction of passage vortices

ii) As the tip clearance increases the leakage vortex becomes stronger weakening the passage vortex but overall pressure loss coefficient increases.

iii) Dimpled tip reduces the total pressure loss than the plan tip at 1.5% clearance because dimple induces the flow resistance which decreases the leakage. It gave the best pressure reduction performance

iv) Among all the tip grooved along pressure side tip and double squealer tip showed the best total loss reduction

v) On the basis of structural stability and total pressure loss coefficient, grooved type tip can lead to higher performance of the plant reducing the secondary flow.

2.6 Conclusions from literature review

Literature review revealed considerable amount of publications both experimental and computational in the field of secondary loss phenomena for turbine cascade. The end loss flow models from different authors are based on steady flow experiments and very often result from flow visualization techniques in cascades.

Based on these reviews, there appears to be a number of factors that influence end losses: these are total airfoil loading, size of end wall surface area, vorticity in inlet end wall boundary layer, sweep and shrouding. Each of these factors has some influence on end loss generation which undoubtedly an indication of complexity of end wall flows.

Moreover various researchers had tried to find out the ways of reducing the secondary losses. Leading edge modification and endwall contouring are the two common and efficient ways of reducing the secondary loss which can consequently increase the aerodynamic efficiency of the turbine cascade.

2.7 Gaps in Literature Review

Much work has been done to understand the occurrence and modeling of secondary flow and end loss phenomenon. Moreover researchers had tried to reduce the secondary loss in any cascade in order to get higher aerodynamic efficiency of the power plant. Effect of sweep, shrouding, leading edge modification and contouring has been studied efficiently. Roughness being an influential parameter in the working of any power plant is important to be considered for proper analysis of the plant. It is a well known fact that roughness over the blade surface increases the profile loss in the cascade. But effect of roughness on the secondary flow and corresponding losses has not studied much.

2.8 Scope of Present Study

The primary objective of this present study is to carry out the three dimensional computational investigations of end loss phenomena in reaction blade profile (profile 6030) on turbine flow path at steady state condition. The purpose of this present work is to validate the CFD result for the smooth blade with experimental result obtained by **Samsher (2002)** and then using the Fluent software for computing the average secondary loss by applying roughness of 500µm on various surface of profile 6030. This result will be compared with the secondary loss in case of smooth cascade profile 6030. Comparison of results shades some light on the effect of roughness on the secondary loss in the turbine cascade of any plant.

CHAPTER-3
MODELLING OF CASCADE

Geometry, boundary conditions and flow analysis in turbomachinery are complex as geometry is three- dimensional, boundary conditions are varied and flow is unsteady which necessitates use of CFD as analytical tool. The present computational study has been carried out using CFD

Aim of this chapter is to provide brief overview of the CFD software used, description of three dimensional geometry modeling & computational methodology and boundary conditions. This chapter provides basic theory on the primary equations governing fluid motion, various turbulence models available, computational domain, operating & boundary conditions used in current study to investigate effects of end loss phenomena in turbine steam path.

3.1 Basic Governing Equations

Theoretically, to analyze the fluid flow, the basic conservation equations have to be solved. The equations that govern the flow include those for the

- Conservation of momentum (Navier-Stokes equation)
- Conservation of mass (Continuity equation)
- Conservation of energy (Energy Equation)

Conservation of momentum was independently constructed by Navier (1827) and Stokes (1845) and are referred to as the Navier-Stokes equation. Solution of governing equations is achieved by discretising the domain into finite control volume mesh. The governing equations are integrated over each control volume in such a way that mass, momentum, energy etc. are conserved in a discrete sense for each control volume.

3.1.1 Continuity equation

This states that mass can neither be created nor destroyed. The general continuity equation in tensor notation is expressed as shown in equation 3.1.

$$\frac{\partial \rho}{\partial t} + \frac{\partial}{\partial x_i}(\rho u_i) = S_m \qquad (3.1)$$

The equation 3.1 is valid for both incompressible as well as compressible flow. For flow in which density of fluid remains constant, the continuity equation reduces to as shown in equation 3.2.

$$\frac{\partial}{\partial x_i}(\rho u_i) = S_m \qquad (3.2)$$

Where, ρ is the density of the fluid, $\frac{\partial}{\partial xi}$ is the divergent operator, u_i is the velocity vector of the fluid and S_m is the momentum source term.

3.1.2 Momentum equation

The conservation of momentum is derived from Newton's second law of motion & in an inertial reference frame in Cartesian coordinate system is expressed as shown in equation 3.3.

$$\frac{\partial}{\partial t}(\rho u_i) + \frac{\partial}{\partial x_j}(\rho u_i u_j) = -\frac{\partial p}{\partial x_j} + \frac{\partial \tau_{ij}}{\partial x_j} + \rho g_i + F_i \qquad (3.3)$$

Where p is the static pressure, ρg_i is the gravitational body force, F_i is the external body force and τ_{ij} is the stress tensor which is expressed as shown in equation 3.4.

$$\tau_{ij} = \left[\mu \left(\frac{\partial u_i}{\partial x_j} + \frac{\partial u_j}{\partial x_i} \right) \right] - \frac{2}{3} \mu \frac{\partial u_i}{\partial x_j} \delta_{ij} \qquad (3.4)$$

Where μ is the molecular viscosity and the second term on the right hand side is the effect of volume dilation and δ_{ij} is the Kronecker's delta.

The value of $\delta_{ij} = 0$ if, $i \neq j$

$= 1$ if, $i=j$.

3.1.3 Energy equation

The conservation of energy equation is expressed as shown in equation 3.5.

$$\frac{\partial}{\partial t}(\rho E) + \frac{\partial}{\partial x_i}(u_i(\rho E + p)) = \frac{\partial}{\partial x_i}\left(k_{eff} \frac{\partial T}{\partial x_i} - \sum_{j'} h_{j'} j_{j'} + u_j (\tau_{ij})_{eff} \right) + S_h \qquad (3.5)$$

Where k_{eff} is the effective conductivity ($k+k_t$, where k_t is the turbulent thermal conductivity) and $j_{j'}$ is the diffusion flux of species j'. The first three terms on the right hand side of energy equation represents energy transfer due to conduction, species diffusion and viscous dissipation respectively. S_h source term if any includes heat of chemical reaction.

The energy term 'E' is further expanded as shown in equation 3.6.

$$E = h - \frac{p}{\rho} + \frac{u_i^2}{2} \qquad (3.6)$$

Where sensible enthalpy 'h' is defined as shown in equation 3.7.

For ideal gases

$$h = \sum_{j'} m_{j'} h_{j'} \tag{3.7}$$

And for incompressible flows as shown in equation 3.8.

$$h = \sum_{j'} m_{j'} h_{j'} + \frac{p}{\rho} \tag{3.8}$$

$m_{j'}$ is the mass fraction of species j' and enthalpy $h_{j'}$ is shown in equation 3.9.

$$h_{j'} = \int_{T_{ref}}^{T} c_{p,j'} dT \tag{3.9}$$

In addition to the above three basic equations of flow, some other equations are also solved depending on the nature of flow phenomenon involved in the problem. For example, if swirling flow takes place in the flow domain, then axial and radial momentum conservation equations are to be solved, where the swirl velocity is included in the equation. Similarly, viscous heating (dissipation) is important for compressible flows, PDF model in energy equation for combustion process, energy source term for chemical reactions, Boussinesq model for natural convection etc. The numerical solution of the three basic equations of fluid flow gives a close approximation to the flow problem for a steady and laminar flow. Most of the flow occurring in nature and engineering applications is turbulent. So treatment for turbulence is required to have better solution to the problem.

These equations along with the conservation of energy equation form a set of coupled, nonlinear partial differential equations. It is not possible to solve these equations analytically for most engineering problems. However, it is possible to obtain approximate

computer-based solutions to the governing equations for a variety of engineering problems. This is the subject matter of Computational Fluid Dynamics

3.2 Turbulence models

Fluid flows of practical relevance are mostly turbulent which is responsible for transport of mass, momentum, heat, etc. in the flow. Turbulence models approximate these transport processes in terms of mean flow field by empirical formulations. Transport equations for turbulence quantities are used to model the transport of turbulence.

Turbulence consists of fluctuations in flow field in time & space. Turbulent flows are highly irregular, unsteady, and chaotic and always occur at high Reynolds number. Turbulence is rotational and three dimensional and is characterized by high level of fluctuating vorticity. Turbulent flows are characterized by fluctuating velocity fields. These fluctuations mix transported quantities such as momentum, energy and species concentration and cause the transported quantities to fluctuate. The instabilities are related to the interaction of viscous terms and non linear inertia terms in the equations of motion. This interaction is very complex: the mathematics of non linear partial differential equation has not been developed to a point where general solutions can be given. The fluctuations of transported quantities are small scale and high frequency, and are too computationally expensive to simulate directly in practical engineering calculation. So the instantaneous governing equations are time averaged, ensemble-averaged, or otherwise manipulated to remove the small scales, which gives a modified set of equations which are less expensive to solve numerically. But the modified equations contains additional unknown variables for which turbulence models are required to determine these unknown quantities in terms of known quantities.

Turbulence models have been specifically developed to account for effects of turbulence without taking recourse to prohibitively fine mesh & Direct Numerical Simulation. Turbulence models modify the original unsteady Navier Stokes equations by introduction of averaged fluctuating components to produce Reynolds Averaged Navier Stokes (RANS) equations. This represents transport equations for mean flow quantities only, with all the scales of turbulence being modeled. The approach of permitting a solution for mean flow variable greatly reduces the computational effort. A computational advantage is seen even in transient situations, since the time step will be determined by the global unsteadiness in the mean flow rather than by the turbulence. This approach is generally adopted for engineering calculations. The most commonly used model κ-ε and its variants, κ-ω and its variants, Spallart-Allmaras and the Reynolds stress model (RSM) adopted the RANS approach for solving turbulent flow field.

In RANS approach, the solution variables in the instantaneous Navier-Stokes equations are decomposed into mean (ensemble-averaged or time averaged) and fluctuating components. The velocity component in tensor notation (3-D) is expressed as shown in equation 3.10.

$$u_i = \overline{u_i} + u_i' \qquad (3.10)$$

Where $\overline{u_i}$ and u'_i are the mean and instantaneous velocity components

Similarly for scalar quantities is shown in equation 3.11:

$$\phi = \bar{\phi} + \phi' \qquad (3.11)$$

Where ϕ denotes a scalar quantity such as pressure, energy, species concentration.

Putting the values of flow variable into instantaneous continuity and momentum equation the simplified equations are expressed as in 3.12 & 3.13.

$$\frac{\partial \rho}{\partial t} + \frac{\partial}{\partial x_i}\left(\rho u_i\right) = 0 \qquad (3.12)$$

$$\rho \frac{Du_i}{Dt} = -\frac{\partial p}{\partial x_i} + \frac{\partial}{\partial x_j}\left[\mu\left(\frac{\partial u_i}{\partial x_j} + \frac{\partial u_j}{\partial x_i} - \frac{2}{3}\delta_{ij}\frac{\partial u_l}{\partial x_l}\right)\right] + \frac{\partial}{\partial x_j}\left(-\rho\overline{u_i' u_j'}\right) \qquad (3.13)$$

The above continuity and momentum equations have the same general form as the instantaneous Navier-Stokes equations. Additional terms appear which represent the effects of turbulence, is called Reynolds stresses, $\rho\,\overline{u'_i\,u'_j}$ and must be modeled in order to achieve "closure" of the modified momentum equation. Closure implies that there are sufficient numbers of equations for all unknowns, including the Reynolds stress tensor resulting from averaging procedure. The equations used to close the system define the type of turbulence model. Additional information on various turbulence models, specifics of numerical solver including validation & verification of the CFD code can be found in **Fluent (2005)** user's manual.

3.2.1 Choice of appropriate Turbulence Model

This is the most important stage of the modeling process. Turbulence modeling should be realistic as far as possible for obtaining a better result. The turbulence in turbomachinery flows is affected by rotation, curvature, three- dimensionality, separation, free stream turbulence, compressibility, large scale unsteadiness, heat transfer and other complex strain effects. The most widely used models for turbomachinery application is the κ-ε model **(Launder and Spalding, 1974)**. In this model, the turbulent kinetic energy (κ)

and the energy dissipation rate (ε) are considered as the properties, which govern the turbulent flow phenomena.

Standard κ-ε model provides good prediction for many flows but is less accurate in prediction of separation & misses out on some of the transport effects. Standard κ-w model is able to predict separation but misses out on some of the transport effect.

The Realizable κ-ε turbulence model of **Shih et al. (1995)** has been selected for solution of present problem .It is a recent development that satisfies the mathematical constraints on the normal stresses. This model is expected to provide more accurate results since it contains additional terms in the transport equations for κ and ε that are more suitable for stagnation flows and flows with high streamline curvature. When attempting to predict secondary flow features, it is important to ensure correct airfoil loading in the simulation, as this will have a direct impact on secondary flow loss.

This model is different from standard κ-ε model in two aspects, this model contains a new formulation for turbulent viscosity. A new transport equation for dissipation rate, ε , has been derived from an exact equation for transport of mean square vorticity fluctuation. From the name of the model it indicates that the model satisfies certain mathematical constraints on the Reynolds stresses, consistent with the physics of turbulent flow. Other two κ-ε models are not realizable. The benefits of realizable κ-ε model is that it predicts more accurately the spreading rate of both planar and round jets. This model provide superior performance for flows involving rotation, boundary layers under strong pressure gradient, separation and recirculation (as in case of flow past aerofoil). Initial studies have shown that the realizable model provides the best performance of all the κ-ε model version for validation of separated flows and flows with complex secondary flow features.

The modeled transport equations for κ and ε in the realizable κ-ε model are shown in equations 3.14 to 3.16.

$$\frac{\partial(\rho k)}{\partial t}+\frac{\partial}{\partial x_j}(\rho k u_j) = \frac{\partial}{\partial x_j}\left[\left(\mu+\frac{\mu_t}{\sigma_k}\right)\frac{\partial k}{\partial x_j}\right] + G_k + G_b - \rho\varepsilon - Y_M + S_k \quad (3.14)$$

and

$$\frac{\partial(\rho\varepsilon)}{\partial t}+\frac{\partial(\rho\varepsilon u_j)}{\partial x_j} = \frac{\partial}{\partial x_j}\left[\left(\mu+\frac{\mu_t}{\sigma_k}\right)\frac{\partial \varepsilon}{\partial x_j}\right] + \rho C_1 S\varepsilon - \rho C_2 \frac{\varepsilon^2}{\kappa+\sqrt{\nu\varepsilon}} + C_{1\varepsilon}\frac{\varepsilon}{\kappa}C_{3\varepsilon}G_b + S_\varepsilon \quad (3.15)$$

Where $C_1 = \left[0.43, \frac{\eta}{\eta+5}\right]$, $S = \sqrt{2S_{ij}S_{ij}}$ and $\eta = S\kappa/\varepsilon$ (3.16)

In the above equations G_k is the turbulent kinetic energy due to mean velocity gradients, G_b is the generation of turbulent kinetic energy due to buoyancy, Y_M is the contribution of fluctuating dilatation in compressible turbulence to the overall dissipation rate, C_2 and $C_{1\varepsilon}$ are constants, σ_κ and σ_ε are the turbulent Prandtl number for κ and ε respectively. These values are computed as shown in equations 3.17 to 3.19.

$$G_k = -\rho\overline{u'_i u'_j}\frac{\partial u_j}{\partial x_i} \quad (3.17)$$

$$G_b = \beta g_i \frac{\mu_t}{\mathrm{Pr}_t}\frac{\partial T}{\partial x_i} \quad (3.18)$$

and β is computed as $\beta = -\frac{1}{\rho}\left(\frac{\partial\rho}{\partial T}\right)_p$ (3.19)

For ideal gases the term is expressed as shown in equations 3.20 & 3.21.

$$G_b = g_i \frac{\mu_t}{\rho \Pr_t} \frac{\partial \rho}{\partial x_i} \quad (3.20)$$

$$Y_M = \rho \varepsilon 2 M_t^{\ 2} \quad (3.21)$$

$\mu_t = \sqrt{\frac{\kappa}{a^2}}$ where is a is speed of sound (a = $\sqrt{\gamma RT}$)

3.3 Description of Computational Domain

The present work is to analyze the secondary loss in smooth cascade and then comparing this loss with the secondary loss in the cascade having roughness of 500µm computationally using commercially available software FLUENT® code. The FLUENT® code is based on finite volume technique and collocated grid method is used to compute the flow domain. The 6030 cascade profile consists of three flow channels using four test blades placed in rectilinear cascade test section with appropriate stagger angle, chord, pitch, and inlet fluid flow angle and inlet/outlet section for fluid (air) to flow as shown in Fig.3.1.

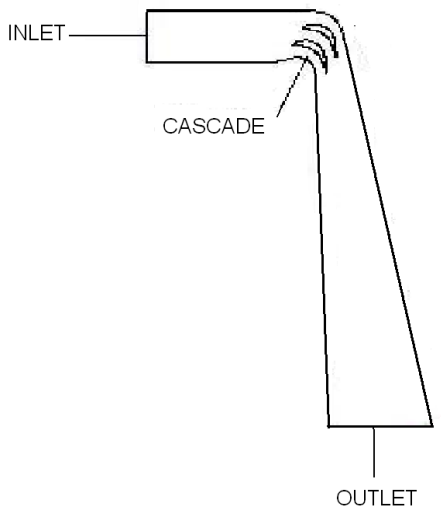

Fig. 3.1: Shape of turbine blade 6030 cascade model *(Samsher 2007)*

3.3.1 Geometry Creation using Gambit®

For any CFD analysis the most important part is geometry creation and meshing as it has tremendous influence on the solution. Therefore, great care has to be taken in choosing appropriate mesh and mesh size.

A three dimensional model of the profile 6030 was created, with the help of Gambit® and the dimensions of the model were kept same as the experiment performed by Samsher [2007] from inlet measurement plane to exit of the tunnel. But due to the limitation of the available system processing of this profile having five flow channels was not possible so the same profile was designed in Gambit with four blades and three flow channels. Dimensions of the cascade & flow parameters for test section are shown in Table 3.1. Chord of all the blades are 50 mm and height is 95 mm. The coordinates of the profile 6030 used for study are given in Appendix 2.

Table 3.1 Cascade dimensions and flow parameter.

Parameters	**Profile 6030**
Cascade type	Rectilinear
Type of test blade	Reaction type
Chord (mm), c	50
Pitch (mm), S	22
Height (mm), l	95
Blade stagger angle	70°
Inlet flow angle	65°

Number of blades	4
Number of channels	3
Working fluid	Air
Inlet air temperature	30°C
Reynolds number at exit (R_{e2})	4.7×10^5

First of all various co-ordinates of 6030 profile are plotted using vertex command in Gambit®. By using the edge command all the co-ordinates are joined to obtain a wireframe model. This gives us a blade of the turbine. Now rotate this blade at the stagger angle of 70°. Copy this profile 3 times to get the desired cascade and now adjust the cascade to the required inlet flow angle.

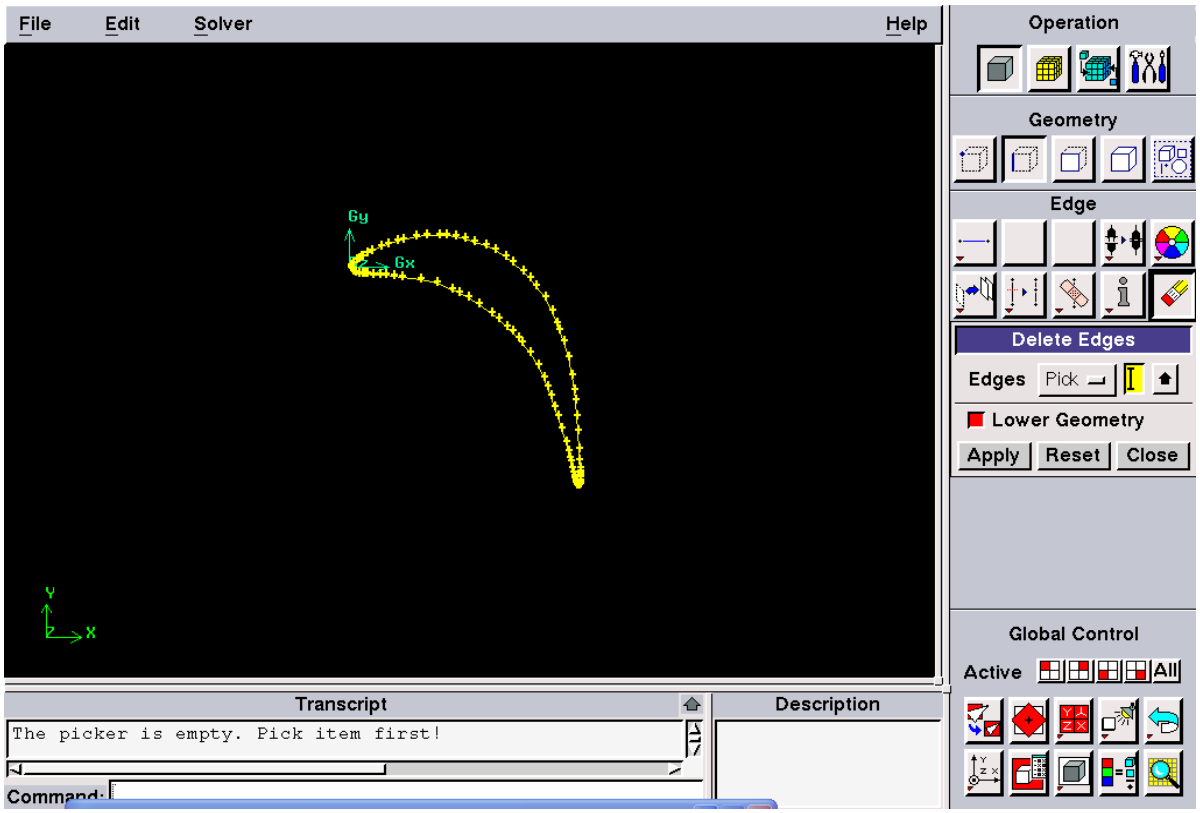

Fig.3.2: A Blade at Required Stagger Angle

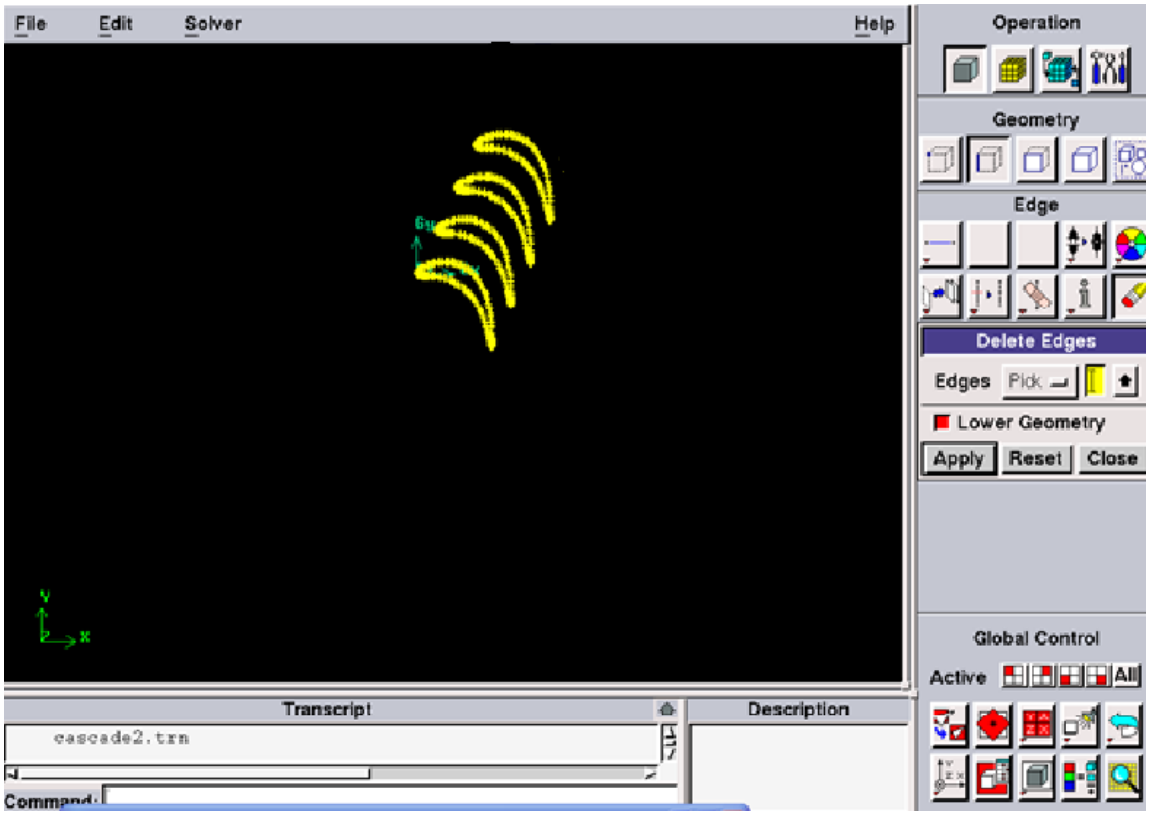

Fig. 3.3: A required set of blades

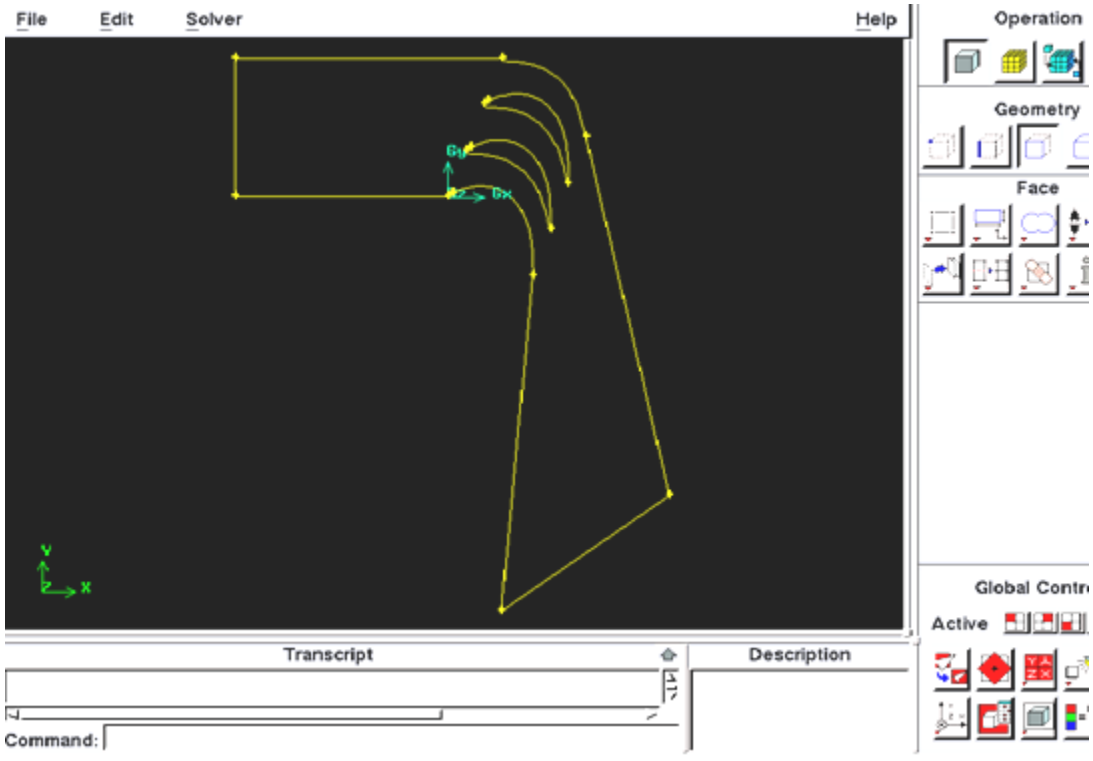

Fig. 3.4: Designed Cascade

The wireframe cascade model obtained is divided into 2 faces. Face 1 consists of the outer boundaries of cascade and Face 2 is obtained by subtracting the inner 2 blades faces from Face1.

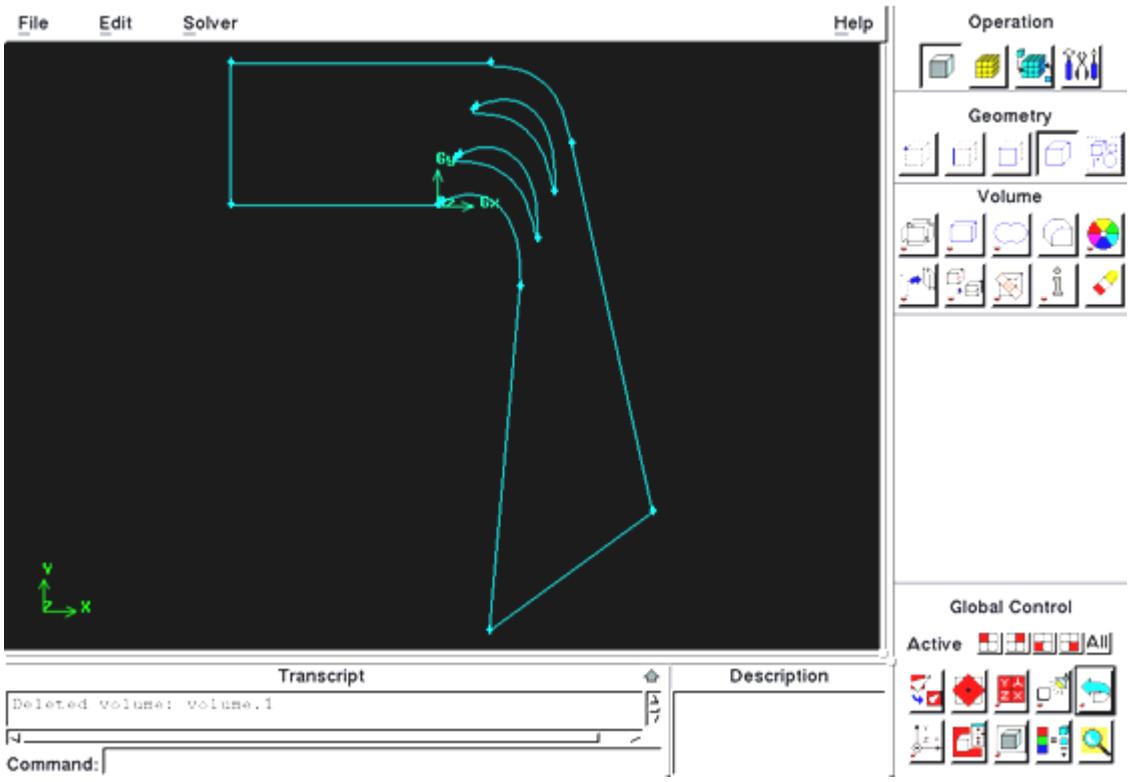

Fig. 3.5: face of the designed cascade.

Then this 2-D model was converted into 3-D by sweeping the faces of the 2-D model by blade height. Flow domain was modeled with four blades, instead of six used in experiment in order to optimize on computing power/processor capacity. Flow is assumed to be symmetric about the mid span plane.

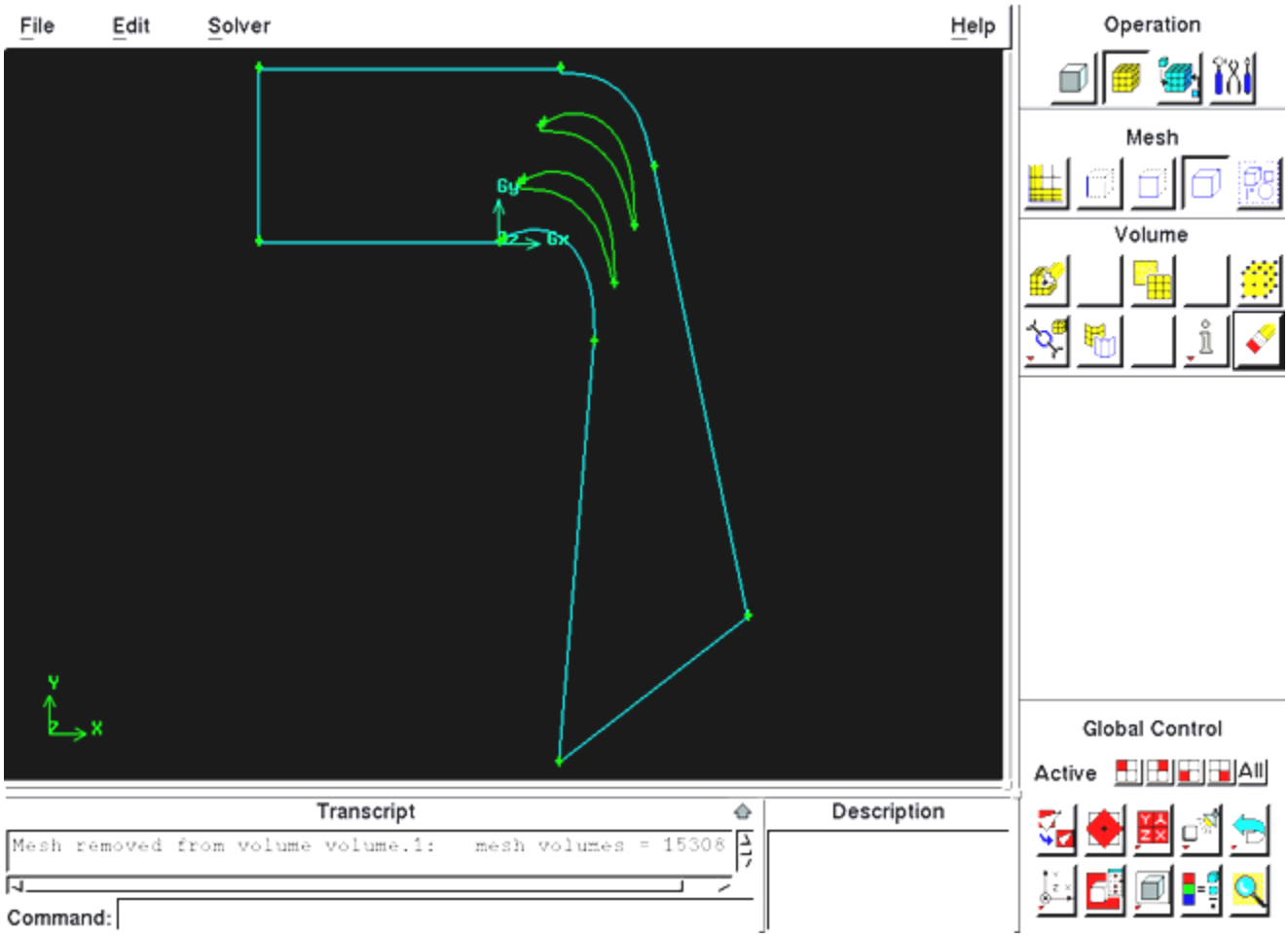

Fig. 3.6: Volume of designed cascade

After creating the desired volume which is subjected to fluid flow meshing of Volume 1 is done of 1 interval size.

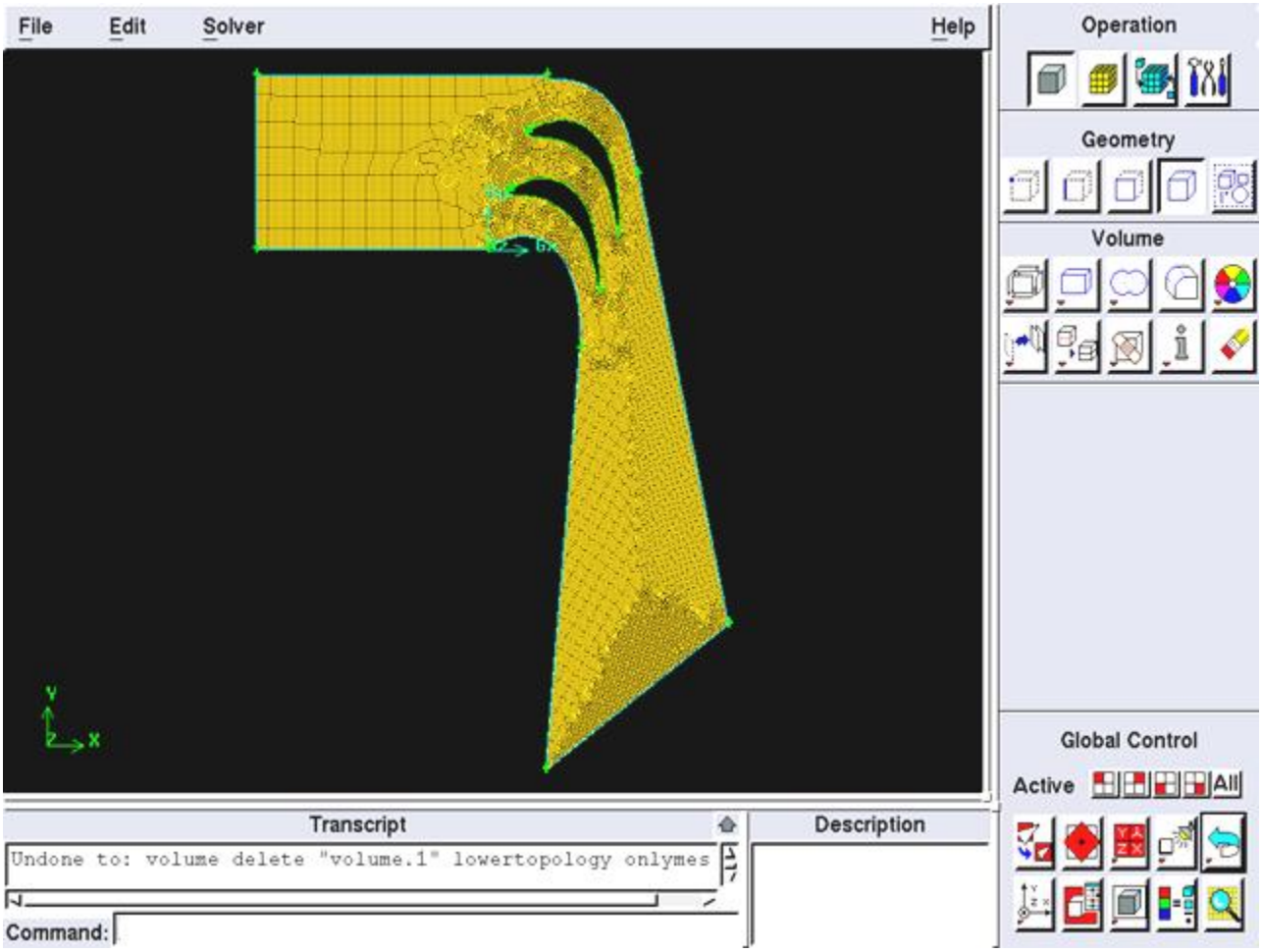

Fig. 3.7 : Meshing of fluid field

Now the boundary types are defined. The inlet to the cascade is defined as velocity inlet and outlet as pressure outlet, all other boundaries are defined as wall. These boundary types will be used in Fluent to define the boundary conditions which is an important aspect of Fluent. This meshed 3-D geometry of cascade is saved and then exported to mesh which will be used read in fluent as case file. Grid checking and scaling of the model is done in fluent. K-epsilon realizable viscous solver model is selected because of its added advantage. The various operating and boundary conditions are stated and the model is iterated to convergence.

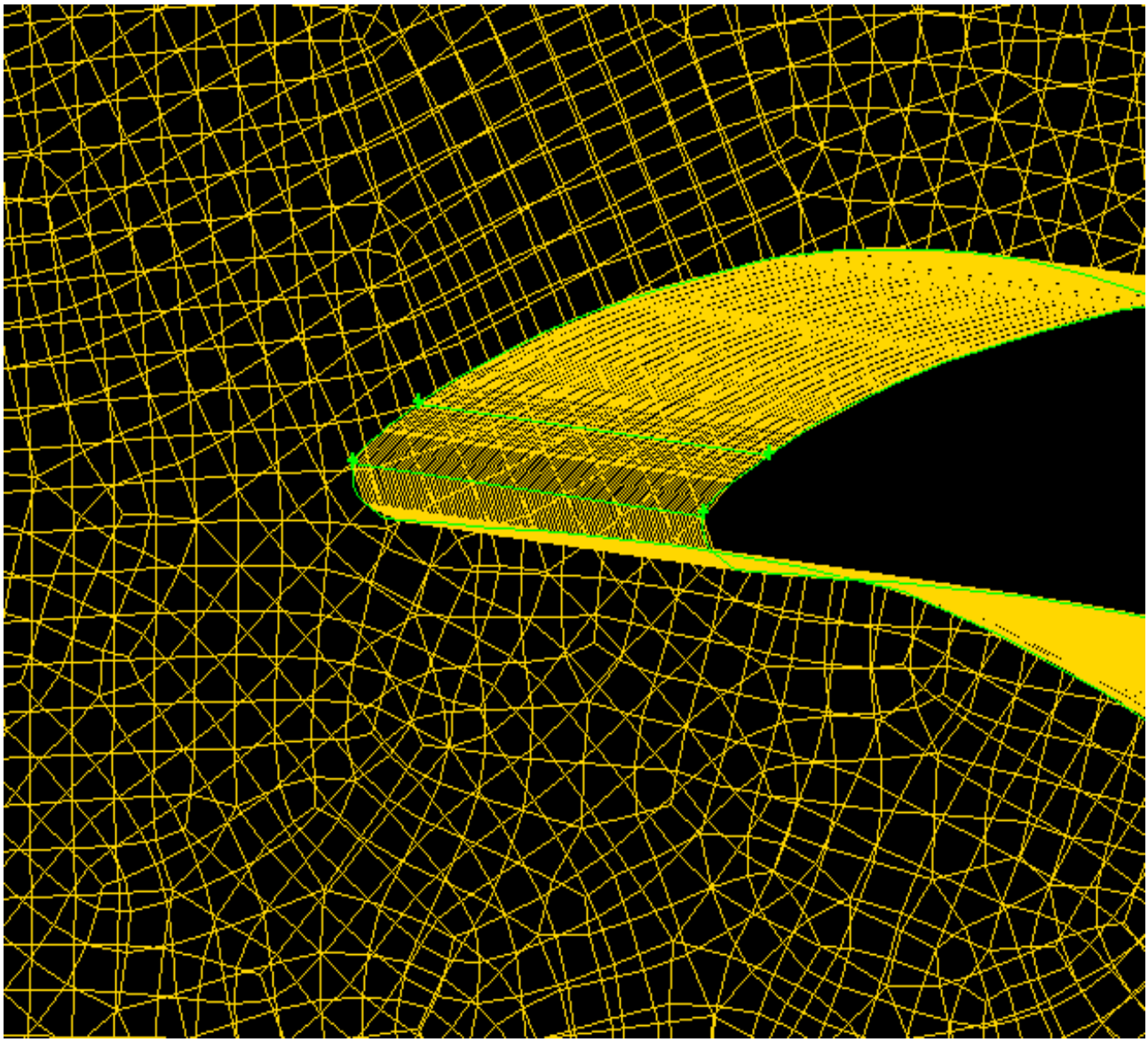

Fig.3.8: *3-D meshing near the leading edge of blade 6030*

Total cell count for the entire computational domain: 15,30,830 hexahedral cells

15 separate boundary zones were created from various faces & boundary types were assigned as follows

Boundary zone	**Boundary type**
Inlet faces	Velocity inlet
Outlet faces	Pressure outlet
Suction surface of blade 1	Wall
Suction surface of blade 2	Wall
Suction surface of blade3	Wall
Pressure surface of blade 2	Wall
Pressure surface of blade 3	Wall
Pressure surface of blade 4	Wall
Lower inlet	Wall
Upper inlet	Wall
Lower outlet	Wall
Upper outlet	Wall

3.4 Boundary And Operating Conditions

3.4.1 Boundary Conditions

Boundary conditions are perhaps the most important factor in influencing accuracy of flow computation. The manner in which boundary conditions are imposed also influences convergence properties of solution. Appropriate description of boundary conditions help in accurate capture of physics of flow. Boundary conditions specify the flow and thermal variable on the boundaries of the physical model. Therefore, boundary conditions are critical components of the simulation and are important that the boundary conditions be specified appropriately. For the designed cascade velocity inlet and pressure outlet boundary conditions are used. A well posed set of inlet and exit boundary conditions for this flow are:

For flow inlet plane - Inlet velocity, temperature, turbulence intensity (%) and turbulent viscosity ratio are specified.

For flow exit plane - Exit static pressure, exit total temperature, turbulence intensity (%) and turbulent viscosity ratio are specified.

The atmospheric temperature is assumed to be constant at 27 °C, though in experiment performed by Prof Samsher it varied from 20°C to 35 °C. The velocity at the inlet is given as 102 m/s. The pressure outlet value at exit is assigned as zero gauge pressure, as the exit is directly exposed to atmosphere.

Initially blade surfaces were kept smooth and results were obtained. Then a roughness of 500µm as applied on suction surfaces and pressure surfaces of the blade individually and then on both the surfaces together and corresponding results were noted.

FLUENT® requires specification of transported turbulence quantities at inlet and outlet, when flow enters a domain. The turbulent kinetic energy and specific dissipation rate at the inlet and outlet are assumed uniform in the present case. The turbulence quantities can be specified in terms of turbulence intensity, turbulent viscosity ratio, hydraulic diameter, and turbulence length scale. The turbulence intensity, I is the ratio of the root mean square of the velocity fluctuations, u', to the mean flow velocity, u_{avg}.

The turbulence intensity at the core of a fully developed duct flow can be estimated from the following formula derived from an empirical correlation for pipe flows:

$$I = \frac{u'}{u_{avg}} = 0.16(\mathrm{Re}_{D_H})^{-1/8} \qquad (3.22)$$

The turbulence length scale l, is physical quantity related to the size of the large eddies that contain the energy in turbulent flows. In fully developed flows, l is restricted by the size of the duct, since the turbulent eddies cannot be larger than the duct. An approximate relationship between l and the physical size of the duct is as following:

$$l = 0.07L \qquad (3.23)$$

where L is the relevant dimension of the duct. The factor of 0.07 is based on the maximum value of the mixing length in fully developed turbulent pipe flow, where L is the diameter of the pipe. In a channel of non-circular cross-section, L can be based on hydraulic diameter. The turbulent kinetic energy is derived from the turbulent intensity I as following:

$$k = \frac{3}{2}(u_{avg}I)^2 \qquad (3.24)$$

where u_{avg} is the mean flow velocity.

The turbulent dissipation rate ε can be calculated from the turbulence length scale l, by the following relationship:

$$\varepsilon = C_{\mu}^{3/4} \frac{k^{3/2}}{l} \qquad (3.25)$$

where C_μ is empirical constant specified in the turbulence model (approximately 0.09). From the above relations the values of turbulent kinetic energy and turbulent dissipation rate are calculated for inlet and outlet and specified in boundary conditions at inlet and outlet.

For the blade surfaces, wall boundaries are assigned. And for the rest of bounded edges, wall boundary conditions are prescribed.

3.4.2 Operating conditions

Operating pressure affects the solution in different ways for different flow regimes. In a low Mach number compressible flow (like the present simulation), the overall pressure drop is small as compared to the absolute static pressure and can be significantly affected by numerical round off. To avoid the problem of round-off error, the operating pressure (generally a large pressure roughly equal to the average absolute pressure in the flow) is subtracted from the absolute pressure. The relation between the operating pressure, gauge pressure and absolute pressure is expressed as:

$$P_{abs} = p_{op} + p_{gauge} \qquad (3.26)$$

The location of the operating pressure is equally important when the computational output is to be compared with experimental results. So the location of the operating

pressure is to be identified where the absolute static pressure is known. In the present problem the pressure parameter at inlet is known.

The operating pressure is considered 101325 Pa at the inlet measurement point, at x = -0.08985, y = 0.0002 m and z= 0.0475m

The measurement plane is at 15 % distance of chord distance as shown in Fig. 3.9.

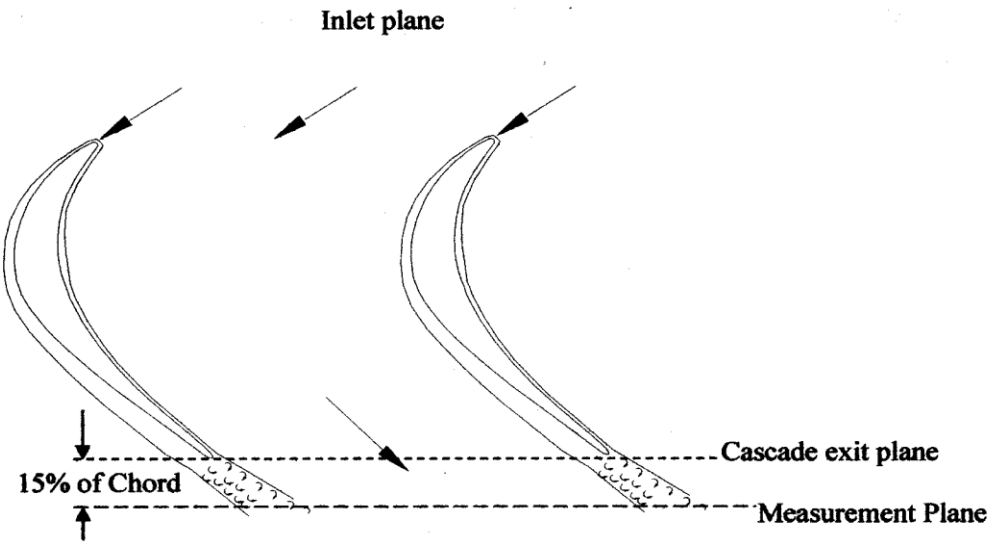

Fig. 3.9 : Measurement plane at 15% of the chord

3.5 Profile loss calculations

The efficiency of cascade can be expressed as

$$\eta = \frac{h_1 - h_2}{h_1 - h_{2s}} = \frac{V_2^{\,2}}{V_{2s}^{\,2}} = \phi^2 \tag{3.27}$$

$$\eta = \frac{C_p (T_0 - T_2)}{C_p (T_0 - T_{2s})} = \frac{\left[1 - \frac{T_2}{T_0}\right]}{\left[1 - \frac{T_{2s}}{T_0}\right]} \tag{3.28}$$

Where C_p is the specific heat of air at constant temperature, T_0 is the temperature at inlet, T_2 is the actual temperature at exit and T_{2s} is the temperature at exit when expansion in the cascade is isentropic.

In the cascade, the total and static pressures at outlet, P_{02} and P_2 respectively and total pressure at inlet is P_{01}, are measured with yaw probe and total pressure probe. Therefore, in terms of the measured values, equation 3.29 can be written as:

$$\eta = \frac{\left[1-\left[\frac{P_2}{P_{02}}\right]^{\frac{\gamma-1}{\gamma}}\right]}{\left[1-\left[\frac{P_{2s}}{P_{01}}\right]^{\frac{\gamma-1}{\gamma}}\right]} \qquad (3.29)$$

Where

$$\frac{P_2}{P_{02}} = \frac{P_2/P_{01}}{P_{02}/P_{01}} = \frac{P_2/P_{01}}{\frac{P_{01}-P_{01}-P_{02}}{P_{01}}} = \frac{P_2/P_{01}}{1-\left[\frac{P_{01}-P_{02}}{P_{01}}\right]}$$

$$= \frac{P_2/P_{01}}{1-\left[\frac{P_{01}-P_{02}}{P_{01}}\right]\left[\frac{P_{01}-P_2}{P_{01}-P_2}\right]} \qquad (3.30)$$

or

$$\frac{P_2}{P_{02}} = \frac{P_2/P_{01}}{1-\left[\frac{P_{01}-P_{02}}{P_{01}-P_2}\right]\left[\frac{P_{01}-P_2}{P_{01}}\right]} = \frac{P_2/P_{01}}{1-\left[\frac{P_{01}-P_{02}}{P_{01}-P_2}\right]\left[1-\frac{P_2}{P_{01}}\right]} \qquad (3.31)$$

Now substituting the value of P_2/P_{02} from equation 3.31 in equation 3.29. We have

$$\eta = \frac{1-\left[\dfrac{P_2/P_{01}}{1-\left[\dfrac{P_{01}-P_{02}}{P_{01}-P_2}\right]\left[1-\dfrac{P_2}{P_{01}}\right]}\right]^{\frac{\gamma-1}{\gamma}}}{\left[1-\left[\dfrac{P_{2s}}{P_{01}}\right]^{\frac{\gamma-1}{\gamma}}\right]}$$

Or

$$\eta = \frac{\left[1-\left[\dfrac{P_{01}-P_{02}}{P_{01}-P_2}\right]\left[1-\dfrac{P_2}{P_{01}}\right]\right]^{\frac{\gamma-1}{\gamma}} - \left[\dfrac{P_2}{P_{01}}\right]^{\frac{\gamma-1}{\gamma}}}{\left[1-\left[\dfrac{P_{2s}}{P_{01}}\right]^{\frac{\gamma-1}{\gamma}}\right]\left[1-\left[\dfrac{P_{01}-P_{02}}{P_{01}-P_2}\right]\left[1-\dfrac{P_2}{P_{01}}\right]\right]^{\frac{\gamma-1}{\gamma}}} \qquad (3.32)$$

The profile loss coefficient ξ_y is calculated using the relation proposed by Dejc and Trojanovskij, expressed as

$$\xi_y = 1- \eta \qquad (3.33)$$

Substituting the value of η in equation 3.34, we have

$$\xi_y = 1-\frac{\left[1-\left[\dfrac{P_{01}-P_{02}}{P_{01}-P_2}\right]\left[1-\dfrac{P_2}{P_{01}}\right]\right]^{\frac{\gamma-1}{\gamma}} - \left[\dfrac{P_2}{P_{01}}\right]^{\frac{\gamma-1}{\gamma}}}{\left[1-\left[\dfrac{P_{2s}}{P_{01}}\right]^{\frac{\gamma-1}{\gamma}}\right]\left[1-\left[\dfrac{P_{01}-P_{02}}{P_{01}-P_2}\right]\left[1-\dfrac{P_2}{P_{01}}\right]\right]^{\frac{\gamma-1}{\gamma}}} \qquad (3.34)$$

On simplification the above equation and putting value of $P_2 = P_{2s}$ (as both points are on same pressure line), equation 3.34 is expressed as follow

$$\xi_y = \left[\frac{P_{2s}}{P_{01}}\right]^{\frac{\gamma-1}{\gamma}} \frac{1-\left[1-\left[\frac{P_{01}-P_{02}}{P_{01}-P_{2s}}\right]\left[1-\frac{P_{2s}}{P_{01}}\right]\right]^{\frac{\gamma-1}{\gamma}}}{\left[1-\left[\frac{P_{2s}}{P_{01}}\right]^{\frac{\gamma-1}{\gamma}}\right]\left[1-\left[\frac{P_{01}-P_{02}}{P_{01}-P_{2s}}\right]\left[1-\frac{P_{2s}}{P_{01}}\right]\right]^{\frac{\gamma-1}{\gamma}}} \qquad (3.35)$$

The effect of change of pitch distance on the profile loss is shown in Fig. 3.10

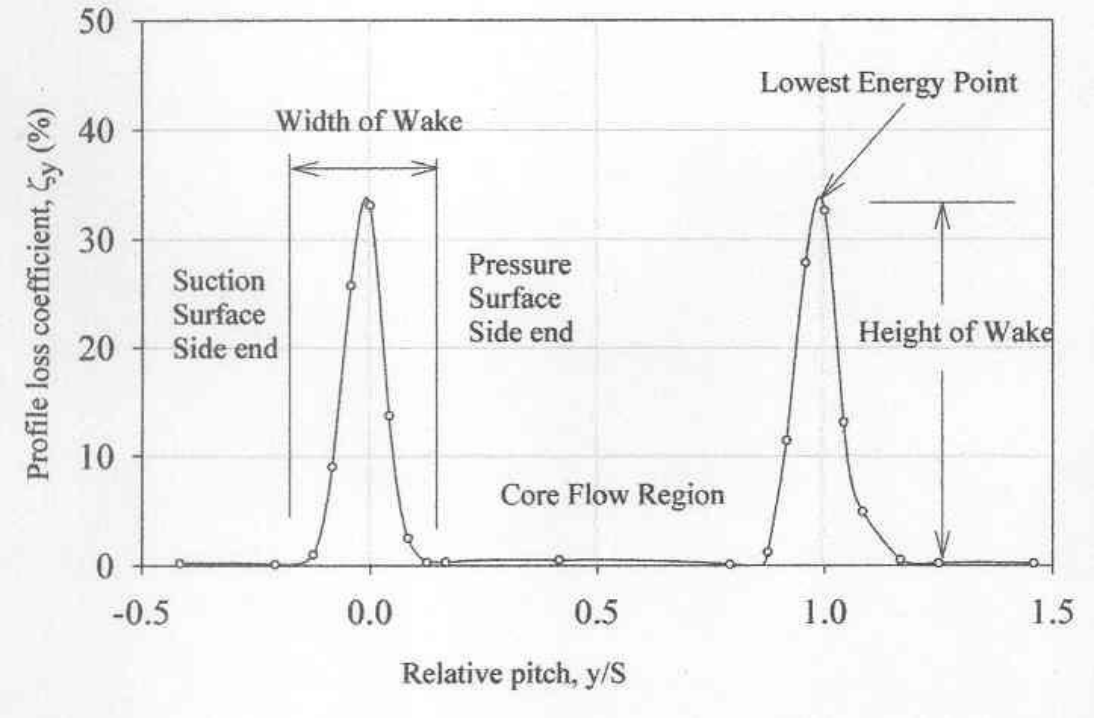

Fig. 3.10: Profile loss coefficient versus relative pitch (Samsher, 2007)**.**

Where, P_{2s} is static pressure at outlet of cascade, P_{01} and P_{02} are the total pressures at the inlet and outlet of cascade respectively, γ is the ratio of specific heats for air.

CHAPTER-4
RESULT AND DISCUSSIONS

Initially the turbine cascade was designed by Gambit®. The boundary types were defined in the pre-processor itself. The exported mesh of the cascade was analyzed using the Fluent 6.2 as solver. The detailed boundary conditions were described in Fluent. The flow field of smooth turbine cascade was analyzed. The flow, pressure, velocity vector, flux were analyzed at appropriate location. At the inlet the measurement plane was taken at (-0.01, 0.005, 0) and (-0.01, 0.055, 0) by drawing a line line/rake option in Fluent. For getting the value of energy loss coefficient, these planes were taken along the whole span.

Similarly for analyzing the pressure, velocity, flux and flow at the exit the measurement plane was selected. At the exit the measurement plane was at 15 % distance of chord distance because at this plane loss is maximum. The measurement plane at the exit was defined by co-ordinates (0.034, -0.06, 0) and (0.0608, 0.0144, 0) by taking the rake at this plane. The measurement planes were then taken along the whole span corresponding to inlet measurement plane for computing the energy loss coefficient along the span.

4.1 Validation of total loss computed from 3-D simulation with experimental data along blade span

Average total loss coefficients were computed from simulation results along blade pitch. Results were compared with experimental values of % loss coefficients measured along the pitch by Samsher [2007] and shown in Fig. 4.1. There is good agreement between trend of computational results & experimental data. Aim of

validation is to show that present numerical model used for simulation is reliable & can be used with confidence for further analysis & parametric studies.

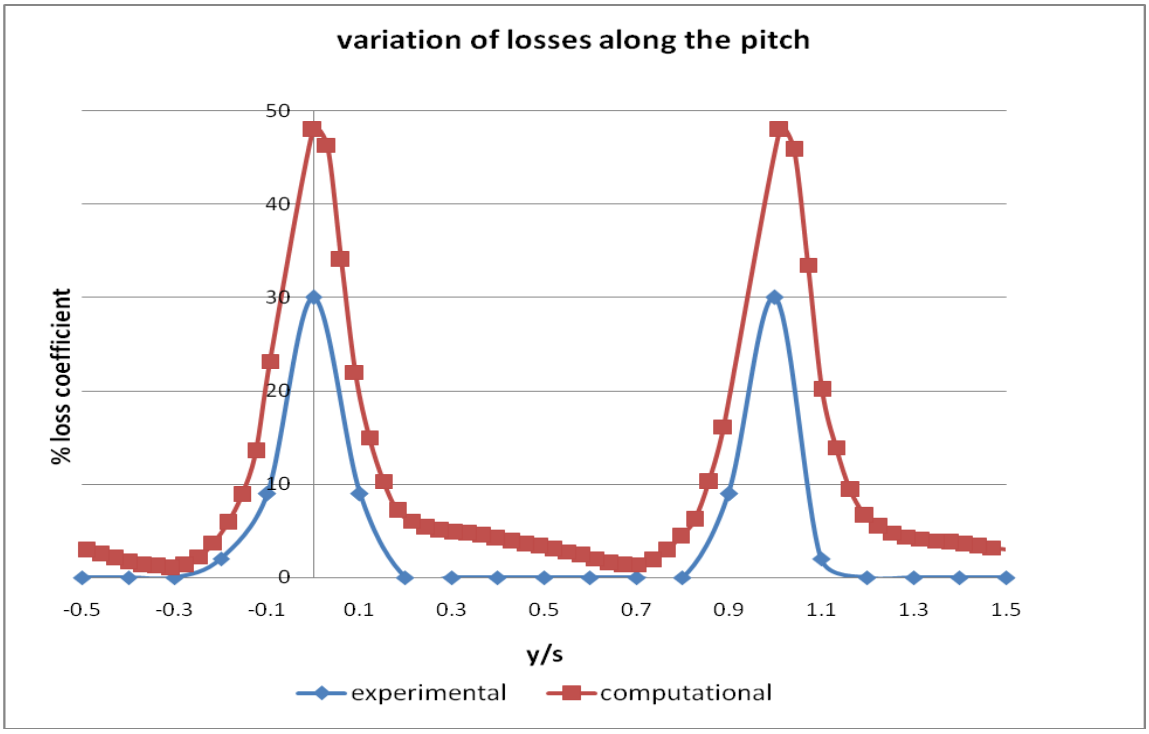

Fig.4.1: Comparison of computational results with experimental data on loss coefficient along the pitch.

The % energy loss coefficient as measured by Prof. Samsher is 30% at the minimum energy region and 0.1% at the highest energy region whereas the computation result by Fluent gave the %energy loss coefficient at the lowest energy region as 47.8% and at the highest energy region as 0.2%. The pattern of variation of %energy loss coefficient v/s non dimensional pitch as obtained by simulation is also in agreement with the experimental result. Hence this computational model is validated against the experimental result of **Samsher [2007]** and can be effectively used for further proceedings.

4.2 Computation of Secondary loss in Smooth cascade

After validating the simulation model, the focus got shifted to the actual area of interest. The aim of this project is to find out the secondary loss in smooth and rough cascade and then analyzing the variation of secondary loss with roughness. The flow was being analyzed for calculating the secondary loss. Average total loss coefficients were computed from simulation results along the complete blade span. Average loss coefficients were computed at 2 mm interval for first 10 mm height from bottom end wall. Thereafter it was computed at every 5 mm interval till 85 mm blade height. Finally for the last 10 mm height it was again computed at every 2 mm interval. The measurement planes at the inlet and exit were already defined. At the inlet, total pressure and at the exit, total as well as static pressure were being noted down along the whole blade span.

4.2.1 Analysis of data

On the basis of readings obtained by the simulation of flow in the smooth cascade, energy loss coefficient was calculated. The local energy loss coefficient ζ_y has been calculated using the following relation proposed by **Dejc and Trojanovskij (1973)** shown in equation 4.1.

$$\xi_y = \left[\frac{P_{2s}}{P_{01}}\right]^{\frac{\gamma-1}{\gamma}} \frac{1-\left[1-\left[\frac{P_{01}-P_{02}}{P_{01}-P_{2s}}\right]\left[1-\frac{P_{2s}}{P_{01}}\right]\right]^{\frac{\gamma-1}{\gamma}}}{\left[1-\left[\frac{P_{2s}}{P_{01}}\right]^{\frac{\gamma-1}{\gamma}}\right]\left[1-\left[\frac{P_{01}-P_{02}}{P_{01}-P_{2s}}\right]\left[1-\frac{P_{2s}}{P_{01}}\right]\right]^{\frac{\gamma-1}{\gamma}}} \qquad (4.1)$$

where, P_{2s} is static pressure at outlet of the cascade, P_{o1} and P_{o2} are the total pressures at the inlet and outlet, respectively, and γ is the ratio of specific heats for air.

To calculate a single value of energy loss coefficient, the mass average value of loss coefficient was calculated using the relation from, **Yahya (2002)** as shown in equation 4.2.

$$\xi = \frac{\int_0^s \xi_y \rho V_a dy}{\int_0^s \rho V_a dy} \qquad (4.2)$$

Where ξ is the mass average loss coefficient, V_a is the axial velocity, ρ is the density of air, S is the pitch distance and dy is the elemental length in pitch wise direction.

Based on above formulae calculations were carried out in Excel worksheet for evaluation of local loss coefficient for each data taken along pitch wise position & then used to evaluate average loss coefficient for that particular span location. Final calculated pitch wise averaged total loss coefficient (expressed in percentage) from the simulation result for different positions along blade span is shown below in Table 4.1.

Table 4.1: %loss coefficient along the blade height for the smooth blade profile 6030

z(mm)	non dim span	% Average total loss	sec loss
0	0.000	25.5	12.7
2	0.021	14.1	1.3
4	0.042	15.6	2.8
6	0.063	16.6	3.8

8	0.084	14.4	1.6
10	0.105	13.7	0.9
15	0.158	13.2	0.4
20	0.211	13.1	0.3
25	0.263	13.0	0.2
30	0.316	13.0	0.2
35	0.368	13.0	0.2
40	0.421	13.0	0.2
45	0.474	13.0	0.2
47.5	0.500	12.8	0.0
50	0.526	13.0	0.2
55	0.579	13.0	0.2
60	0.632	13.0	0.2
65	0.684	13.0	0.2
70	0.737	13.0	0.2
75	0.789	13.1	0.3
80	0.842	13.2	0.4
85	0.895	13.7	0.9
87	0.916	14.4	1.6
89	0.937	16.6	3.8
91	0.958	15.6	2.8
93	0.979	14.1	1.3
95	1.000	25.5	12.7

The total (combined) losses in a blade cascade are estimated by the energy loss coefficient ζ, which is essentially the sum of profile loss coefficient & end loss coefficient as given by **Kostyuk and Frolov (1988)** in equation 4.3.

$$\zeta \text{ (total)} = \zeta \text{ (pr)} + \zeta \text{ (end)} \qquad (4.3)$$

Loss coefficient calculated at blade mid span, where the flow is two-dimensional & influence of end wall effect is not present, constitutes profile losses & is representative of two dimensional reference flows. Thus end loss coefficient along blade height is calculated as the difference between the total and profile energy loss coefficients in a cascade. Using the simulation result end losses along blade span which include all losses in end wall region are obtained by subtracting mid span value of profile loss from individual average loss along the blade height.

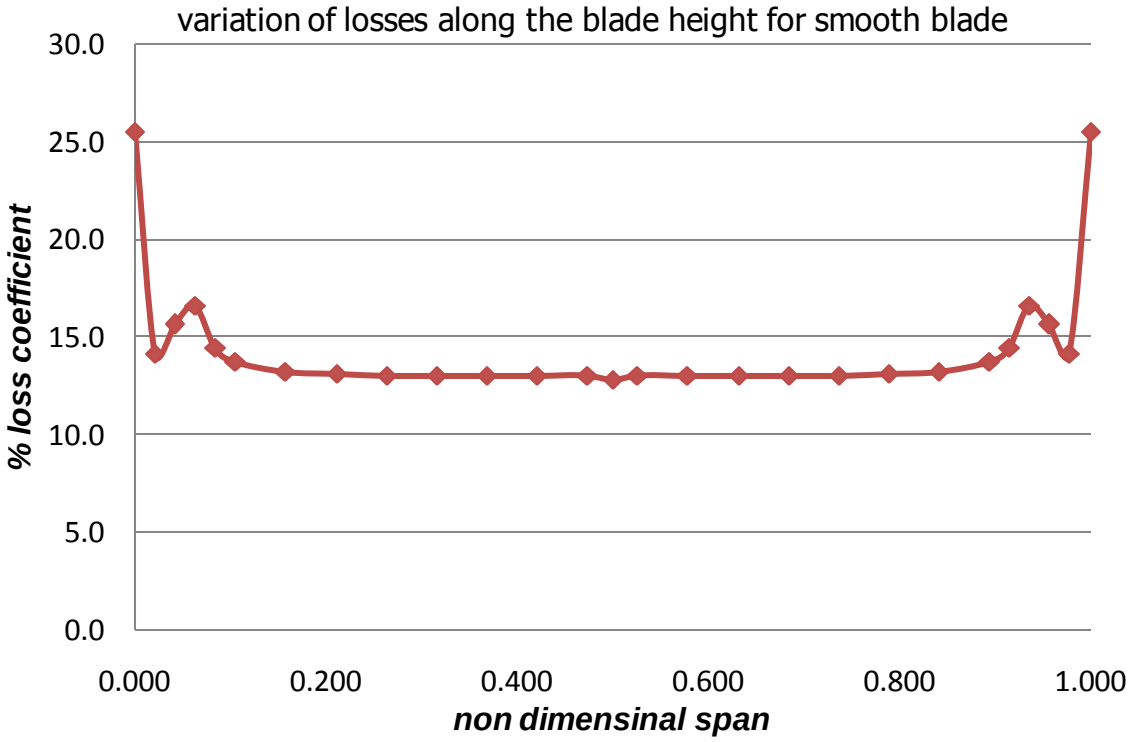

Fig.4.2: Variation of %total loss coefficient along the blade span for smooth blade

Data obtained from the numerical simulation gave the average total loss coefficient as 14.7% and the average secondary or end loss along the blade height is came out to be 1.7%. The total pitch wise average loss is high at hub and casing due to the endwall boundary layers. The local increase in loss coefficient is observed corresponding to the secondary vortex cores near the hub and casing.

4.3 Computation of Secondary Loss on applying the roughness of 500μm

After analyzing the secondary loss in smooth cascade, attention got focused towards the presence of roughness on different blade surface. Secondary loss was analyzed and compared for different cases.

4.3.1 Secondary Loss when roughness is applied to all the suction surfaces

First of all a roughness of 500μm was applied on all the suction surfaces of 6030 blade profile. All other boundary conditions and location of measurement planes remained unchanged. As the numerical model has been already validated against the experimental data so results obtained will be in permissible error limit.

Table 4.2: %loss coefficient along the blade height for the cascade having roughness of 500μm on all the suction surfaces

z(mm)	non dim. span	% total loss coefficient	% Secondary loss
0	0.000	27.9	4.5
2	0.021	27.1	3.7
4	0.042	26.7	3.3
6	0.063	27.2	3.8

8	0.084	25.6	2.2
10	0.105	24.6	1.2
15	0.158	23.7	0.3
20	0.211	23.4	0
25	0.263	23.4	0
30	0.316	23.4	0
35	0.368	23.4	0
40	0.421	23.4	0
45	0.474	23.4	0
47.5	0.500	23.4	0
50	0.526	23.4	0
55	0.579	23.4	0
60	0.632	23.4	0
65	0.684	23.4	0
70	0.737	23.4	0
75	0.789	23.4	0
80	0.842	23.7	0.3
85	0.895	24.6	1.2
87	0.916	25.6	2.2
89	0.937	27.2	3.8
91	0.958	26.7	3.3
93	0.979	27.1	3.7
95	1.000	27.9	4.5

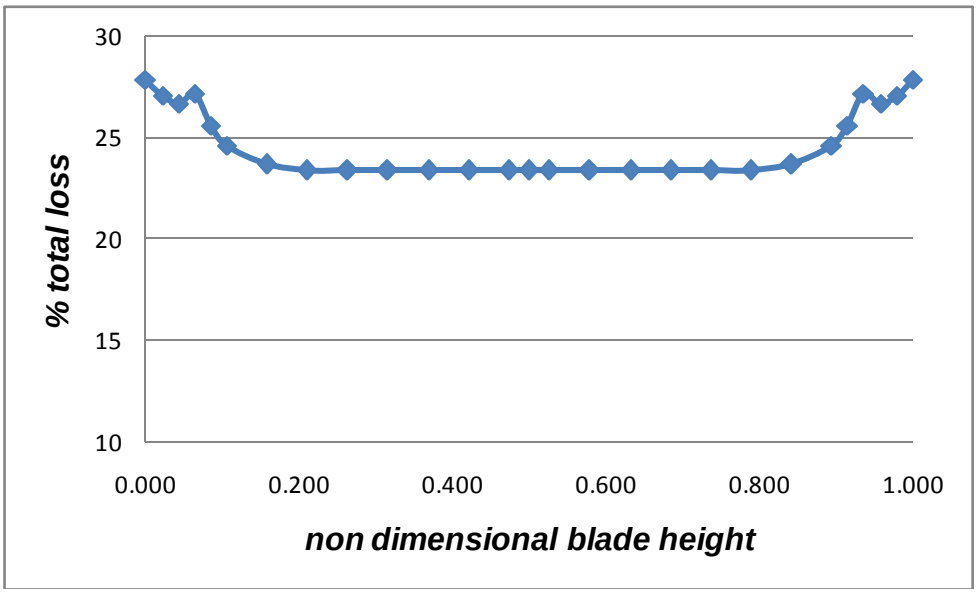

Fig. 4.3: Variation of % total loss coefficient along the blade height when a roughness of 500μm is present on the suction surfaces of the cascade.

Here again the maximum loss occur near the hub and casing due to the presence of end wall. The profile loss for the cascade having all the suction surface rough is 23.4%. The average total loss is 24.8% and average secondary loss along the blade height is 1.4%.

Roughness of 500μm on all the suction surface of the turbine cascade increases the %total loss coefficient from 14.7% to 24.8%. the increase in the total loss is attributed to increase in the profile loss due to roughness but the average value of end loss decreases by 17.64%.

4.3.2 Secondary Loss when roughness is present only on the pressure surfaces

After analyzing the effect of roughness present on the suction over the secondary, the work is moved further by applying the roughness of 500μm only on the pressure surfaces. Presence of roughness increases the average total loss coefficient as well as the profile loss.

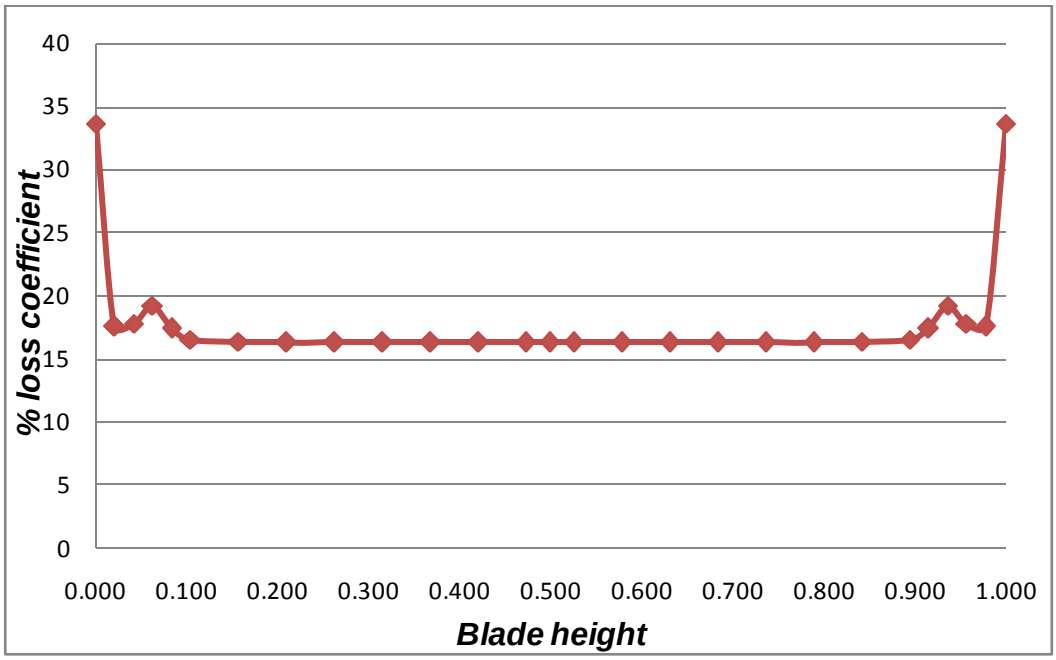

Fig. 4.4: Variation of % total loss coefficient along the blade height when a roughness of 500μm is present on the pressure surfaces of the cascade.

Fig. 4.4 shows that end wall effect increases the total loss near the hub and casing. The maximum value of % loss coefficient at the hub and casing is 33.7%. at the core region this loss gets minimum and attains a value of 16.3%. at the core the total loss consists of only profile loss due to the boundary layer formation and no end loss because at the core end wall is not present. Subtracting this profile loss from the total loss gives the end loss present at that location. The average total loss is 18.1% and average secondary loss is only 1.8%.

4.3.3 Secondary Loss when roughness is present on both the surfaces together

Presence of roughness separately on suction and pressure surface increases the total loss and profile loss. Roughness only on pressure surface reduces the secondary loss but roughness only on suction surfaces increase the secondary loss. Now applying the roughness on suction as well as pressure surface together is analyzed. As expected it increases the profile and total loss. The effect of this roughness on the secondary loss will be analyzed.

Table 4.3: %loss coefficient along the blade height for the cascade having roughness of 500μm on all the pressure surfaces

z(mm)	non dim span	% total loss coefficient	% Secondary loss
0	0.000	36.1	9.9
2	0.021	27.4	1.2
4	0.042	28.7	2.5
6	0.063	29.6	3.4
8	0.084	28.1	1.9
10	0.105	27.1	0.9
15	0.158	26.4	0.2
20	0.211	26.3	0.1
25	0.263	26.2	0
30	0.316	26.2	0
35	0.368	26.2	0
40	0.421	26.2	0
45	0.474	26.2	0
47.5	0.500	26.2	0
50	0.526	26.2	0
55	0.579	26.2	0

60	0.632	26.2	0
65	0.684	26.2	0
70	0.737	26.2	0
75	0.789	26.3	0.1
80	0.842	26.4	0.2
85	0.895	27.1	0.9
87	0.916	28.1	1.9
89	0.937	29.6	3.4
91	0.958	28.7	2.5
93	0.979	27.4	1.2
95	1.000	36.1	9.9

Table 4.3 shows that profile loss is 26.2% for the cascade having a roughness of 500µm all the pressure surface. The average secondary loss is 1.5% but average total loss get increase to 27.7%. The graph showing the variation of %loss coefficient along the span is shown by Fig. 4.5

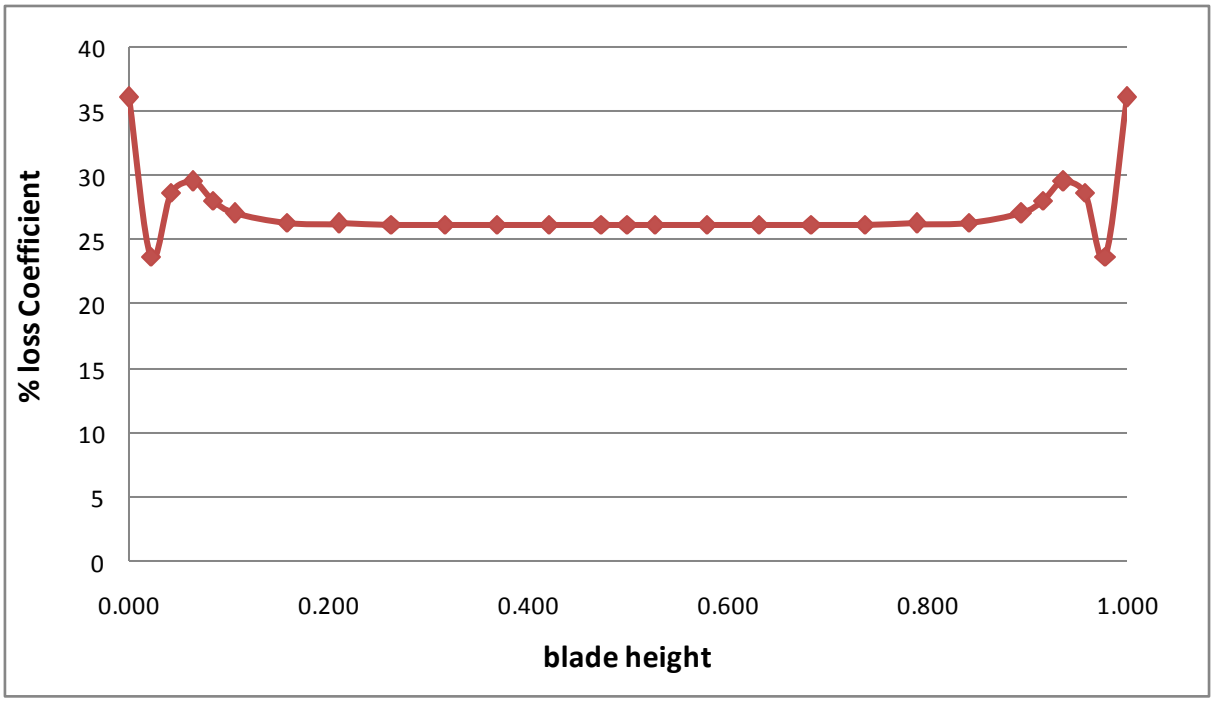

Fig. 4.5: *V*ariation of % total loss coefficient along the blade height when a roughness of 500µm is present on the suction as well as pressure surfaces of the cascade.

4.4 Flow Visualization

Contour plots of total pressure distribution for smooth cascade over entire computational domain at 1% span and 50% span are shown in Figures 4.6 & 4.7

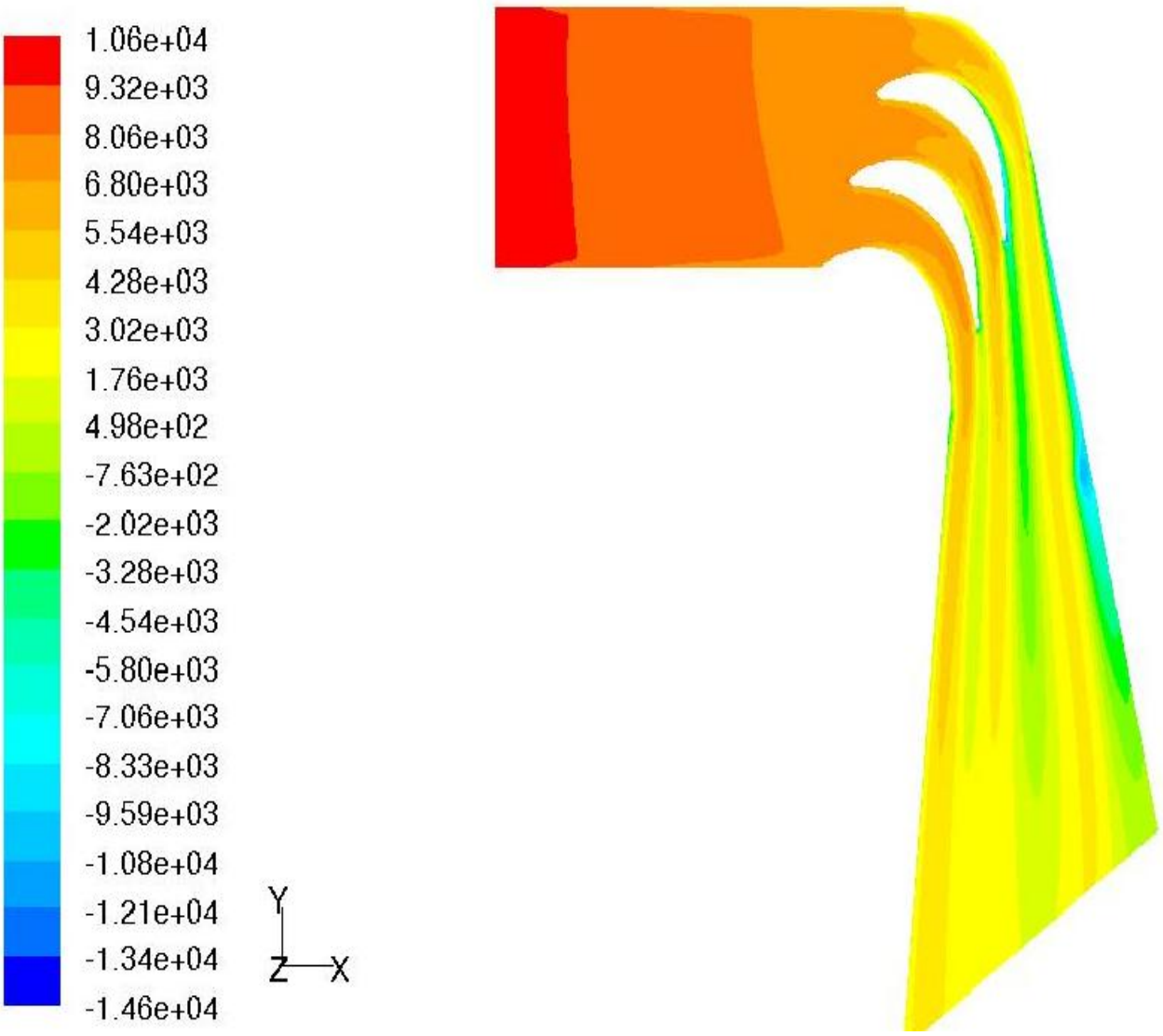

Fig. 4.6: Total pressure distributions in wake region at 1% span for the cascade having all the surfaces smooth .

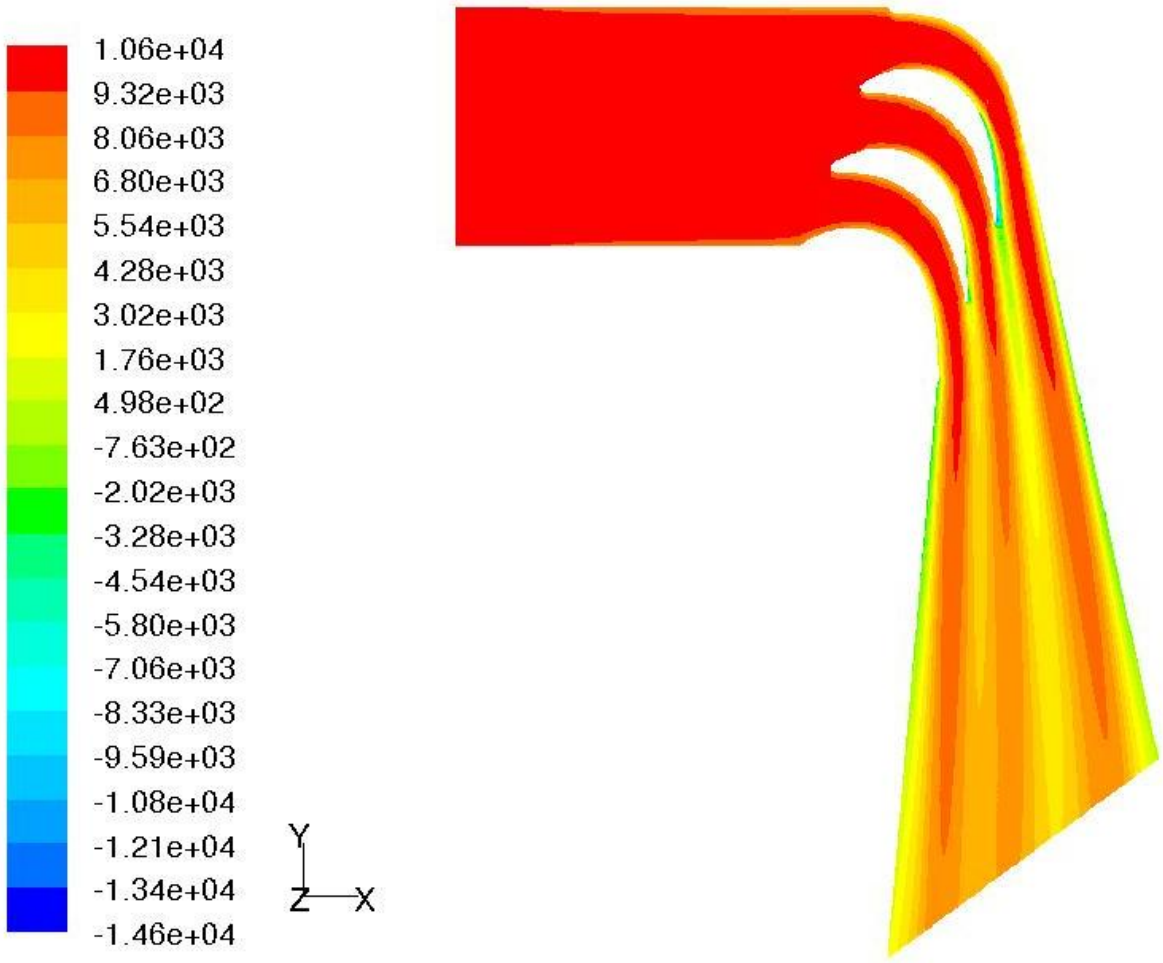

Fig. 4.7: Total pressure distributions in wake region at 50% span for the cascade having all the surface smooth.

After entering cascade section total pressure drops due to expansion of fluid over the cascade section. At exit of cascade wakes are formed where total pressure drops significantly. However in core flow region, pressure drop is insignificant. At significant distance from trailing edge intermixing of core flow and wake takes place and eventually total pressure drops.

At very close to end wall region wake bands are much broader & are much more diffused at very exit from blade trailing edge because of end wall boundary layer interaction as seen in Fig. 4.6 and Fig.4.7.

Similarly the pressure distribution can be seen for the different cases

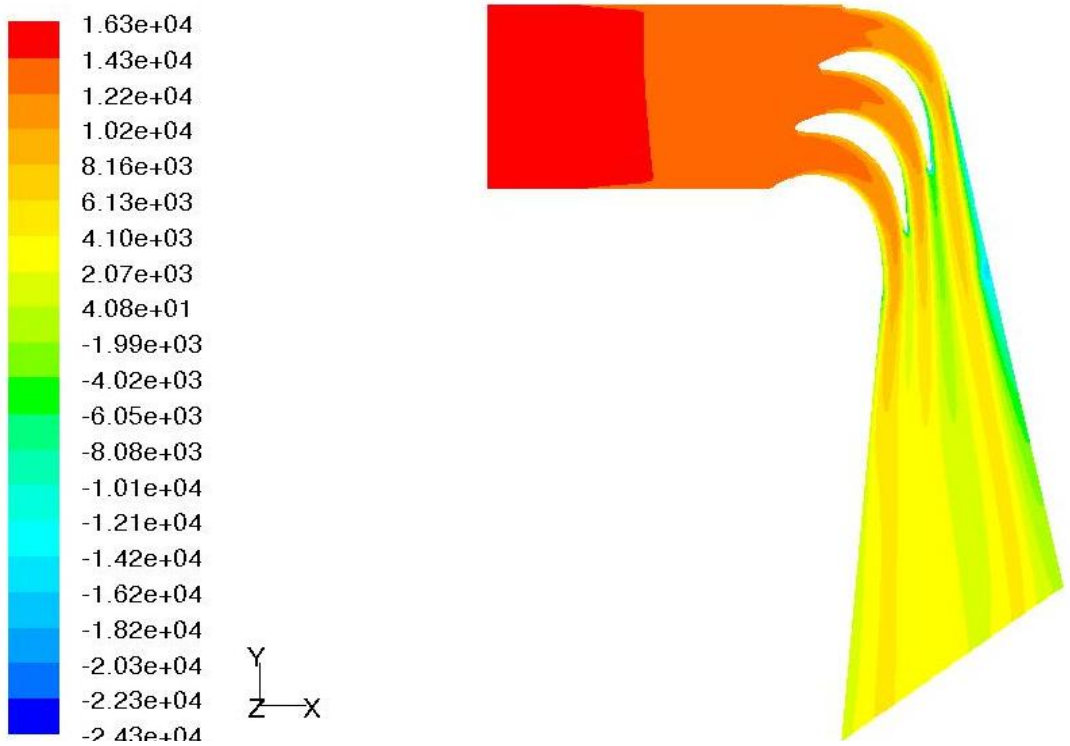

Fig. 4.8: Total pressure distributions in wake region at 1% span for the cascade having both the surface rough.

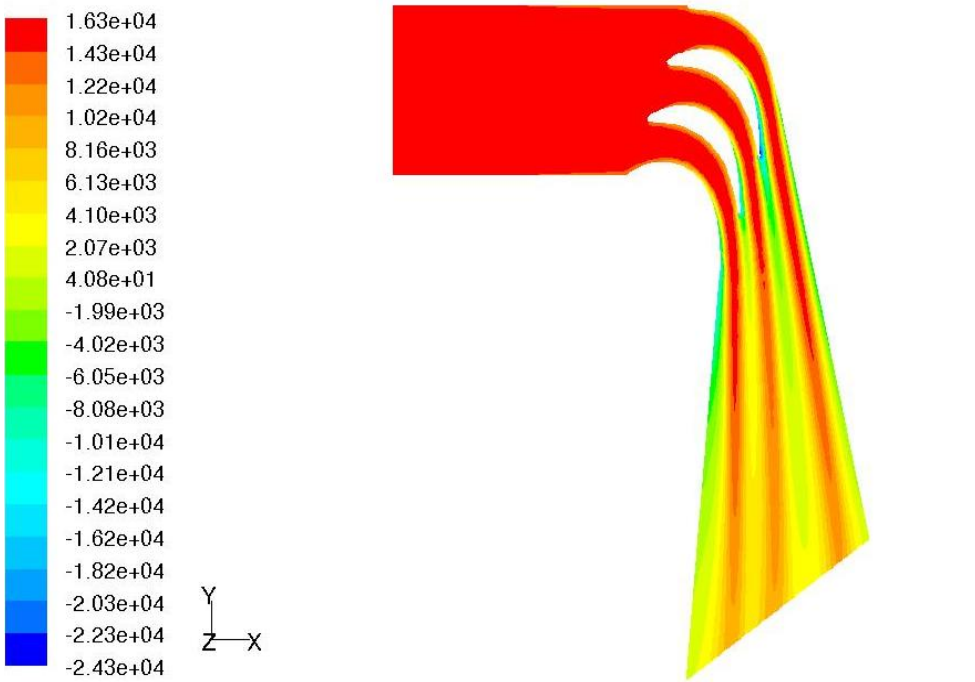

Fig. 4.9: Total pressure distributions in wake region at 50% span for the cascade having both the surface rough

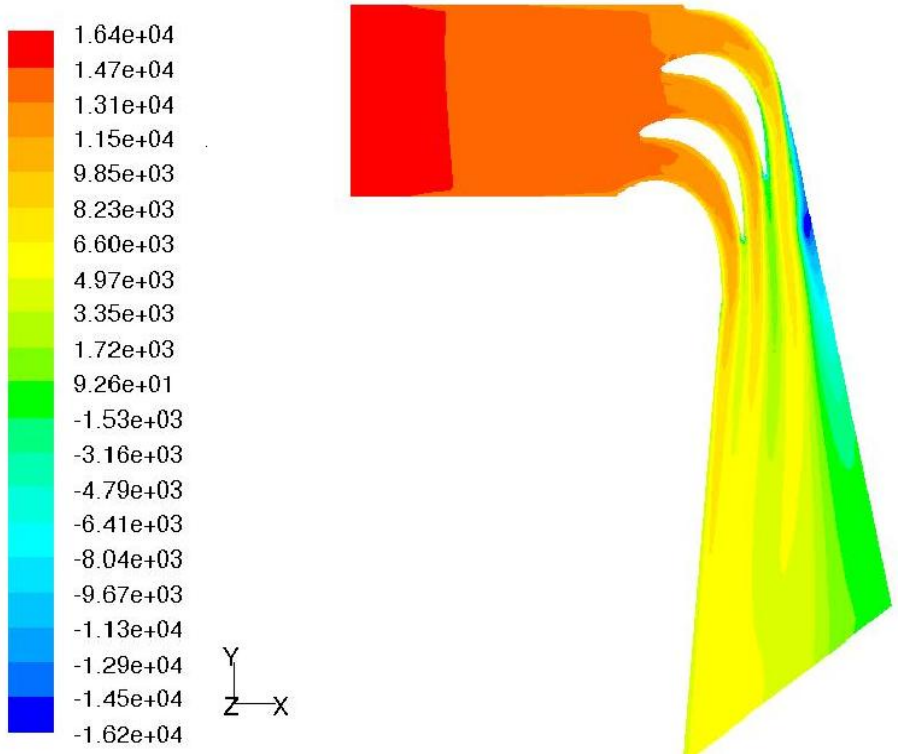

***Fig. 4.10*:** Total pressure distributions in wake region at 1% span for the cascade having all the pressure surface rough

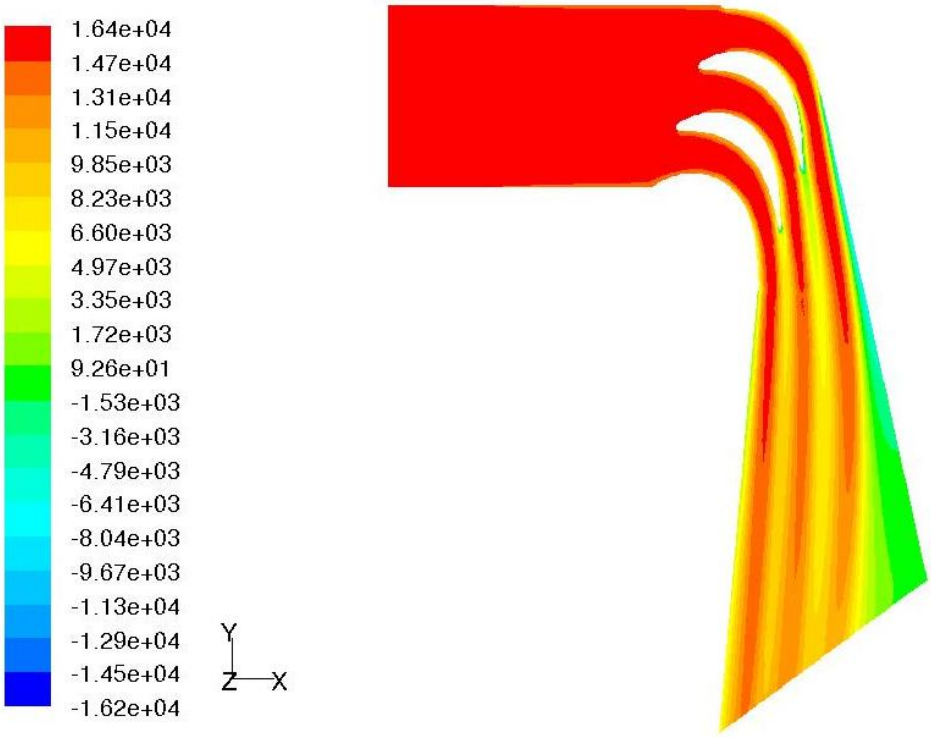

Fig. 4.11: Total pressure distributions in wake region at 50% span for the cascade having all the pressure surfaces rough

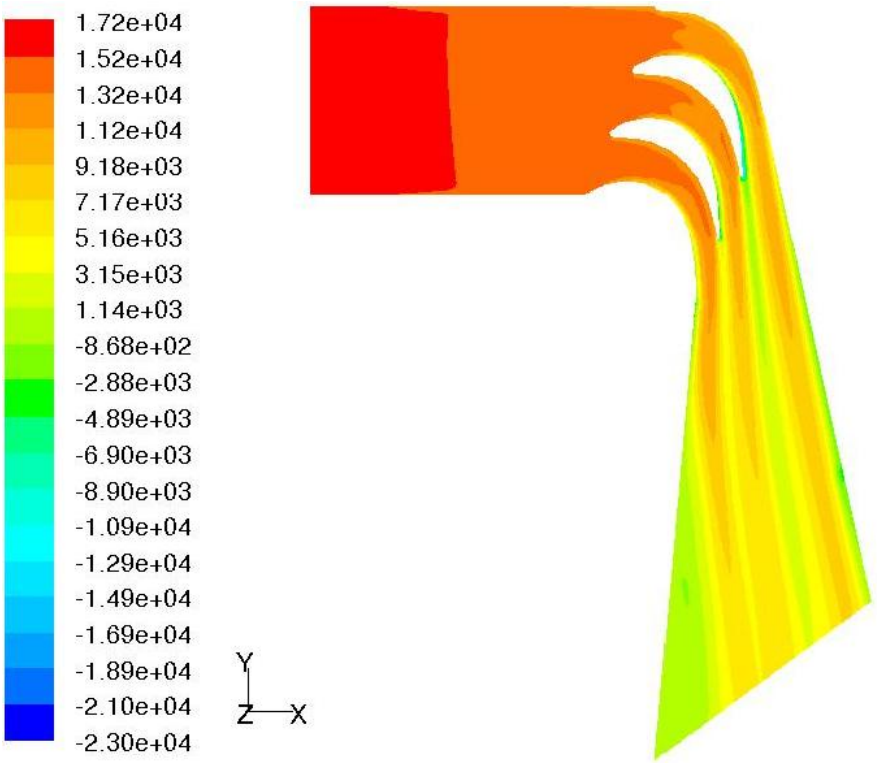

Fig. 4.12: Total pressure distributions in wake region at 1% span for the cascade having all the suction surfaces rough

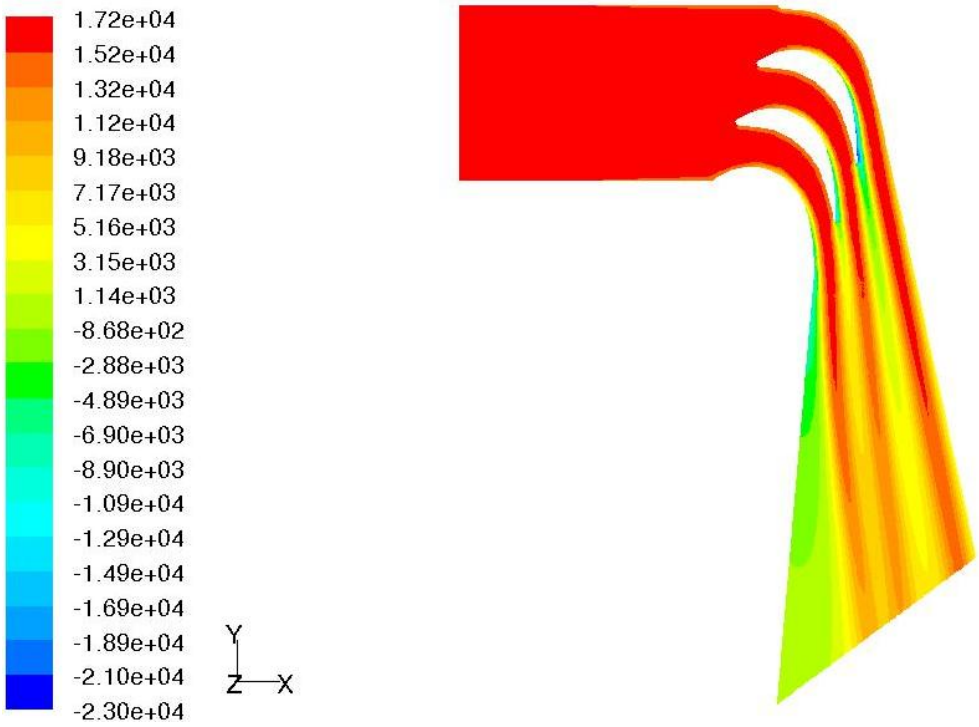

Fig. 4.13: Total pressure distributions in wake region at 50% span for the cascade having all the suction surfaces rough

4.5 Comparison of Secondary Loss in Smooth and Rough Cascade

The %energy loss coefficient and total pressure contours for cascade having both the surfaces smooth and then applied roughness on various surfaces is obtained. It has been observed that the %energy loss coefficient varies with the applied roughness on various surfaces. The comparison of energy loss coefficient and effect of the applied roughness on various blade surfaces can be compared by using Fig. 4.14

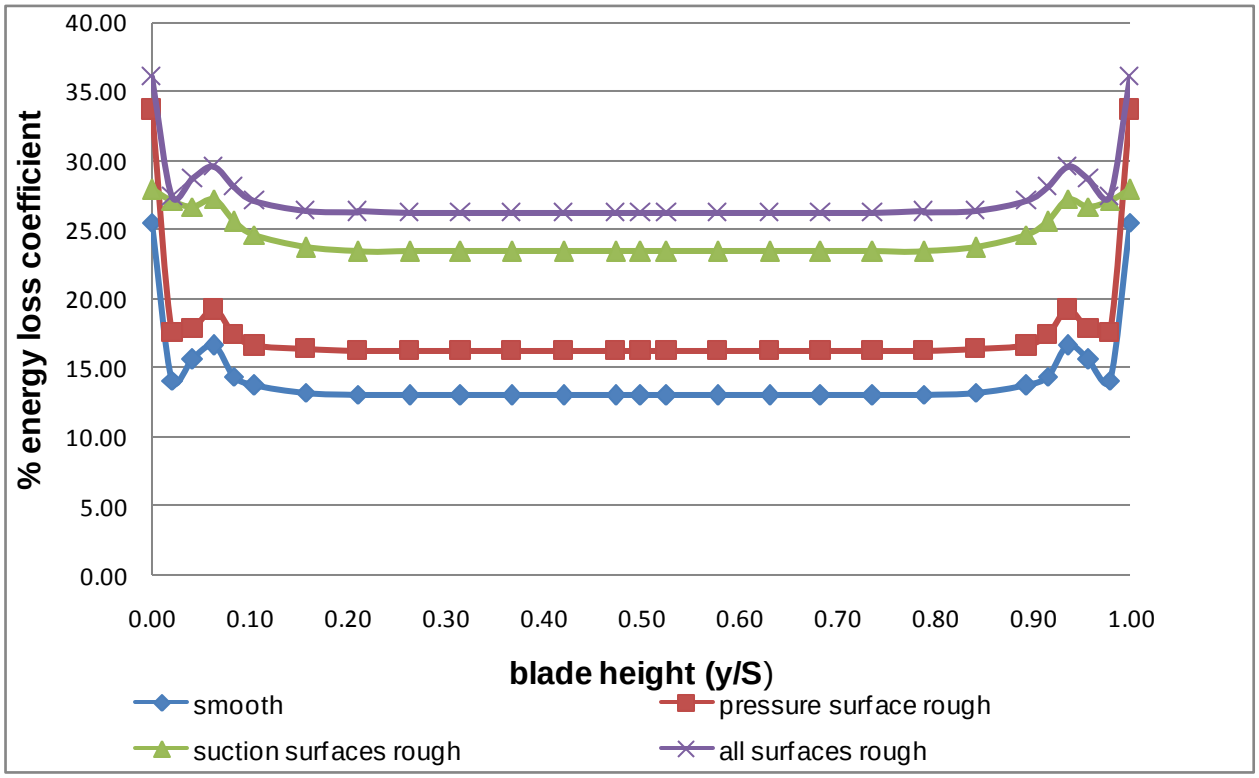

Fig. 4.14: Comparison of energy loss coefficient along the blade height for a) smooth blade surfaces b) all pressure surfaces rough c) all suction surfaces rough d) all the surfaces rough.

It is observed from the Fig. 4.14 that the loss coefficient is high at hub and casing due to the endwall boundary layers. The local increase in loss coefficient is observed near the hub and casing in all the four cases. The profile loss increases as the roughness is being applied to various surfaces. On applying roughness of magnitude 500µm on pressure surface the computed profile loss is 16.3%, roughness on suction surface increases the

profile loss to 23.4% and finally when both the surfaces are rough then the value of profile loss increases to 26.2%. Roughness on the cascade surface increases the profile loss due to thickening of boundary layer and expected separation. The increase in profile loss with the applied roughness validated the model itself. The main aim of this work is to analyze the secondary loss with the applied roughness. It was observed the average secondary loss in smooth blade is 1.7%. When a roughness of 500μm is applied to all the suction surfaces then average secondary loss is 1.3%, it increases to 1.5% when roughness is applied on both the surfaces and then it further reaches a value of 1.9% when roughness is applied to all the pressure surfaces. When roughness is present on all the suction surfaces the secondary loss is least. The probable reason of minimum secondary loss in this case can be accounted due to lack of mixing of passage vortex with the suction side vortex. This decreases the overall secondary loss. When roughness is present on PS as well as SS together then the secondary loss again increases to 1.7%. This increase in secondary loss can occur because of thickening of boundary layer due to roughness which leads to flow separation. Moreover the present of humps at hub and casing occur because of the formation of vortex cores that leads to increase in local energy loss coefficient. As observed from the various pressure contour figures, in between 2-6% of the span adverse pressure gradient is present which causes humps near the hub and casing.

Moreover by comparing the various pressure contours it can be observed that pressure loss is highest in the cascade having both the surfaces rough which increases the energy loss coefficient. Not only this, but the wakes are much broader and diffused in the cascade having all the pressure surfaces rough. Mixing out of a non-uniform flow at blade exit and dissipation of secondary kinetic energy and turbulence kinetic energy downstream of the trailing edge increases the loss in this cascade.

CHAPTER-5

CONCLUSIONS

- The computational model is validated against the experimental work done by Prof. Samsher with good agreement. Computational results obtained from three dimensional simulations are closer to experimentally measured values
- The pattern of variation of energy loss coefficient in span wise direction (y/S) is same for smooth as well as rough blades. Moreover the Fig.4.14 shows that energy loss coefficient is least for smooth blades and it reaches the maximum value in case of the blade on which roughness is introduced on pressure as well as suction surface.
- It is observed that applying roughness on blade surface definitely increases the profile loss as well as total energy loss coefficient. But if both the surface of the blade get rough then the average secondary loss decreases by 11.76%. If roughness is present only on suction surface then the average secondary loss is 1.3% against the average value of secondary loss of 1.7%. Moreover the average secondary loss is 1.9% if roughness is applied to only pressure surface. Hence if roughness is present only on the suction surfaces then secondary loss can decreases by 23.5% in comparison of smooth blade
- Due to the end wall boundary layers the loss coefficient is high at hub and casing.
- Humps are observed near the hub and casing due to secondary vortex which increases the local energy loss coefficient.

CHAPTER-6
FUTURE SCOPES

The effect of roughness on secondary losses is analyzed by applying a roughness of 500μm on suction and pressure surface individually as well as on both the surfaces together and this result is compared with the secondary loss obtained in the cascade having both the surfaces smooth. During the present work, it has been observed that there are areas that require further investigations; some of these are given below

1. Experimental studies can be conducted upon a wider range of turbine blade profiles encountered in high capacity steam and gas turbines.
2. The effect of localized roughness on various surfaces on the secondary flow and losses can be studied further.
3. In the real flow environment of rotating machines, the flow in the turbine blade rows is highly affected by the unsteady conditions. The secondary flow field is also affected by the unsteady inlet flow conditions into the blade passage. Flow unsteadiness may be due to various reasons, some of which are:

   (a) Potential interactions of the upstream and the downstream blade rows.

   (b) Interactions of the upstream wakes with the downstream blade rows.

   (c) Shock wave interaction with the downstream blade rows.

   (d) Leakage and secondary flow vortices interaction with the downstream blades.

Future work can be done in analyzing the effect of roughness on secondary flow and losses using unsteady simulation that can give results closer to the real life situation.

References

[1] Benner M.W., Sjolander S.A. and Moustapha S.H., 2004, "The Influence of Leading-Edge Geometry on Secondary Losses in a Turbine Cascade at the Design Incidence," ASME Journal of Turbomachinery, **126,** 277-287.

[2] Brear Michael J., Hodson Howard P., Gonzalez Palom and Harvey Neil W., 2002, "Pressure Surface Separations in Low-Pressure Turbines—Part 2: Interactions With the Secondary Flow," Transactions of the ASME, **124**, 2002, 402-409.

[3] Chaluvadi, V. S. P. , Kalfas, A. I., Hodson H. P., Ohyama H. and Watanabe E., 2003, "Blade Row Interaction in a High- Pressure Steam Turbine," Transactions of the ASME, **125,** 14-24.

[4] Denton, J.D. and Cumpsty, N.A., 1987, "Loss Mechanisms in Turbomachines," IMechE Paper C, 260-87.

[5] Hawthorne, W.R., 1995, "Rotational Flow through Cascades," Journal of Mechanics and Applied Mathematics, **3,** 266-292.

[6] Holley Brian M. and Langston Lee S., 2009, "Surface Shear Stress and Pressure Measurements in a Turbine Cascade," ASME Journal of Turbomachinery, **131**, 031014-1 - 031014-8.

[7] Knezevici D. C, Sjolander S. A. , Praisner T. J., Bradley E. Allen and Grover E. A., 2007, "Measurements of Secondary Losses in a Turbine Cascade With the Implementation of Nonaxisymmetric Endwall Contouring," ASME Journal of Turbomachinery, **132**, 011013-1 - 011013-10.

[8] Korakianitis T. and Hamakhan I. A., 2010, "Aerodynamic Performance Effects of Leading-Edge Geometry in Gas-Turbine Blades," Applied Energy, **87**,1591–1601.

[9] Langston L. S., Nice M.L. and Hooper R.M., 1977, "Three-Dimensional Flow within a Turbine Cascade Passage," ASME Journal of Engineering for Power, **99**, 21–28.

[10] Launder B. E. and Spalding D. B,1974, "The Numerical Computation of Turbulent Flows," Computer Methods in Applied Mechanics and Engineering, **3** , 269-289.

[11] Lei Qi, Zhengping Zou, Peng Wang, Teng Cao and Huoxing Liu, 2011, "Control Of Secondary Flow Loss Ii Turbine Cascade by Streamwise Vortex ," Computers & Fluids, **54,** 45-55.

[12] Mahmood, G.I. and Acharya S., 2007, "Experimental Investigation of Secondary Flow Structure in a Blade Passage With and Without Leading Edge Fillets," ASME Journal of Fluids Engineering, **129**, , pp. 253-262.

[13] Marchal P., and Sieverding C.H., 1977, "Secondary Flows Within Turbomachinery Bladings," Secondary Flows in Turbomachines, AGARD-CP-214, **11**, 1–19.

[14] Moon, Young J. and Koh Sung-Ryong, 2000, "Counter-rotating streamwise vortex formation in turbine cascade with endwall fencing," Computers And Fluids, **30**, 473-490.

[15] Nho Young Cheol, Park Jung Shin, Lee Yong Jin and Kwak Jae Su, 2011, "Effects of turbine blade tip shape on total pressure loss and secondary flow of a linear turbine cascade," International Journal of Heat and Fluid Flow , **33** , 92–100.

[16] Persico, G., Gaetani P and Osnaghi, C., 2009, "A Parametric Study of the Blade Row Interaction in a High Pressure Turbine Stage," Journal of Turbomachinery, **131**, 031006-1- 031006-13.

[17] Porreca L., Kalfas A.I., and Abhari R.S., 2008, "Optimized Shroud Design for Axial Turbine Aerodynamic Performance", Journal of Turbomachinery, **130**, 031016-1-031016-12.

[18] Pullan Graham, 2006, "Secondary Flows and Loss Caused by Blade Row Interaction in a Turbine Stage," Transactions of the ASME, **128**, 484-491.

[19] Pullan, Graham and Harvey, Neil W., 2008, "The Influence of Sweep on Axial Flow Turbine Aerodynamics in the Endwall Region," Journal of Turbomachinery, **130**, 041011-1 - 041011-10.

[20] Saha Arun K. and Acharya Sumanta, 2008, "Computations of Turbulent Flow and Heat Transfer Through a Three-Dimensional Nonaxisymmetric Blade Passage," ASME Journal of Turbomachinery, **130**, 031008-1- 031008-10.

[21] Samsher, 2007, —Effect of Localized Roughness Over Reaction And Impulse Blades on Loss Coefficient,|| Proceedings of Institution of Mechanical Engineers, Part A: Journal of Power and Energy, **221**, 21-32

[22] Sauer H., Muller R. and Vogeler,K., 2001, " Reduction of Secondary Flow Losses in Turbine Cascades by Leading Edge Modifications at the Endwall," Journal of Turbomachinery, **123,** 207 – 213.

[23] Sharma O.P. and Butler T.L, 1987, "Predictions of Endwall Losses and Secondary Flows in Axial Flow Turbine Cascades," ASME Journal of Turbo machinery, **109**, 229-236.

[24] Shih T. I-P. and Lin Y.L, 2003, "Controlling Secondary-Flow Structure by Leading-Edge Airfoil Fillet and Inlet Swirl to Reduce Aerodynamic Loss and Surface Heat Transfer," Transactions of the ASME, **125,** 48-56.

[25] Shih. T. H., Liou W.W., Shabbir A. and Zhu J., 1995, "A new κ-ε eddy viscosity model for high Reynolds number turbulent flows –models development & validation," Computer And Fluids, **24**, 227-238.

[26] Sieverding C.H and, Bosch P. Van den, 1983, "The Use of Coloured Smoke to Visualise Secondary Flows in a Turbine-Blade Cascade," ASME Journal of Fluid Mechanics, **134,**85-89.

[27] Sonoda Toyotaka, Hasenjäger Martina, Arima Toshiyuki and Sendhoff Bernhard, 2009, "Effect of End Wall Contouring on Performance of Ultra-Low Aspect Ratio Transonic Turbine Inlet Guide Vanes," ASME Journal of Turbomachinery, **131,** 011020-1- 011020-11.

[28] Bhattacharjee Somnath, 2006, "Experimental & Numerical Study of End Loss Phenomena in Turbine Steam Path," M.Tech Thesis, Mech. Engg. Dept. IIT Delhi.

[29] Torre Diego, Vázquez Raúl, Blanco Elena de la Rosa and Hodson Howard P., 2011, "A New Alternative for Reduction in Secondary Flows in Low Pressure Turbines," ASME Journal of Turbomachinery, **133**, 011029-1 - 011029-10.

[30] Wang H.P., Olson S.J., Goldstein R.J., Eckert E.R.G., 1997, "Flow visualization in a linear turbine cascade of high performance turbine blades," ASME Journal of Turbomachinery, **119,** 1-8.

[31] Yahya, S.,M., 2002, "Turbines, compressors and fans ," Tata McGraw-Hill, New Delhi.

[32] Yaras M. I., and Sjolander S.I., 1992, "Effects of Simulated Rotation on Tip Leakage in a Planer Cascade of Turbine Blades: Part II-Downstream Flow Field and Blade Loading," ASME Journal of Turbomachinery, **114**, 660-667.

[33] Zhang Weihao, Zou Zhengping and Ye Jian, 2011, “Leading-edge redesign of a turbomachinery blade and its effect on aerodynamic performance,” Applied Energy.

[34] www.powermin.nic.in/indian_electricity_scenario/introduction.htm

[35] en.wikipedia.orgwikiSecondary_flow

APPENDIX-1

GLOSSORY OF TERMS

Aspect ratio - Ratio of blade height to chord. Reduction in aspect ratio increases the contribution of secondary losses in total aerodynamic losses.

Blade angle - Included angle between tangents drawn on the camber line at leading edge and trailing edge with the axial or tangential direction are the blade angles at inlet and exit, respectively.

Camber angle - The angle between tangent drawn on the camber line at leading edge and chord line at inlet, the angle between tangent drawn on the camber line at trailing edge and chord line is camber angle at exit. The sum of camber angle at inlet and exit is camber angle.

Camber line - A blade section of infinitesimal thickness is a curved line known as camber line. This forms the backbone line of a blade of finite thickness.

Cascade - An infinite row of equidistant similar blade is called a cascade. When blades are arranged in a straight line the cascade is called rectilinear cascade. In annular cascades, the blades are arranged in an annulus. In a radial cascade the blades are arranged radial inward or outward direction.

Chord - A straight line joining center of leading edge and center of trailing edge. The length of this line is blade chord.

Deviation - The difference between flow angle and blade angle at outlet is called deviation angle. It also may be positive or negative.

Flow inlet angle - Angle that the flow makes at inlet with the axial or tangential direction.

Flow outlet angle - Angle that the flow makes at outlet with the axial or tangential direction. It depends on pitch-chord ratio and stagger angle.

Incidence angle - The difference between flow angle and blade angle at inlet. It may be positive or negative.

Leading edge thickness - Edge of Blade where the flow enters.

Pitch-cord ratio - Ratio of pitch to the chord

Pressure and suction surface - The concave surface of the blade is called pressure surface, and convex surface is called suction surface.

Span - Height of the blade from hub to tip.

Stagger angle - Stagger angle is the inclination of chord line with the axial or tangential direction. The shape of the channel changes with change in stagger angle, which results in change in pressure distribution and boundary layer thickness and hence losses. Increase in stagger angle (axial) increases semi-vane-less region and reduces the throat. For the same stagger angle exit angle changes with pitch-chord ratio and for pitch-chord ratio exit angle increase with increase in stagger angle.

Trailing edge thickness - The edge of the blade at flow exit end.

APPENDIX-2

Coordinates of profile 6030

x	y
0.17	2.29
0.18	2.37
0.22	2.55
0.42	3.38
0.67	4.19
1.23	5.67
1.71	6.79
2.41	8.14
2.83	8.88
3.93	10.69
4.98	12.01
6.38	13.43
7.15	14.13
8.32	15.04
9.51	15.80
10.88	16.55
12.68	17.34
14.16	17.79
16.00	18.21
17.43	18.43
19.70	18.54
21.15	18.47
22.78	18.28
25.04	17.89
27.29	17.19
29.35	16.33
30.28	15.92
32.09	15.02
34.41	13.69
36.75	12.12
38.82	10.60
40.07	9.62
41.96	8.07
43.82	6.45
46.00	4.49
47.35	3.26
48.23	2.47
48.66	2.07
48.93	1.83
49.11	1.66
49.28	1.49
49.69	1.09
49.90	0.86
50.00	0.67
50.06	0.54
50.06	0.42
50.02	0.28
49.97	0.24
49.94	0.23
49.91	0.22
49.86	0.21
49.72	0.20
49.52	0.29
49.28	0.41
49.09	0.53
48.80	0.71
48.52	0.89
48.04	1.21
47.43	1.60
46.50	2.18
45.95	2.52
45.04	3.07
43.69	3.88
41.80	4.95
39.99	5.93
38.54	6.68
36.82	7.51
35.45	8.12
34.05	8.67
31.98	9.42
29.72	10.00
27.63	10.31
26.63	10.41
25.37	10.50
24.12	10.52
22.44	10.47
20.99	10.35
18.50	10.00
16.58	9.55
14.99	9.04
13.93	8.68
11.48	7.67
9.21	6.26
6.94	4.58
5.93	3.77
4.98	2.98
4.25	2.36
3.40	1.62
2.76	1.07
2.40	0.76
2.24	0.62
1.79	0.23
1.41	-0.09
0.83	-0.19
0.56	-0.16
0.35	-0.09
0.21	0.01
-0.01	0.22
-0.07	0.66
0.01	1.44
0.09	1.87
0.17	2.29

APPENDIX - 3

Details of model used

A3.1 Meshing at glance

Number of cells	**1530830**
Number of faces	**4527261**
Number of nodes	**1596480 nodes**
Number of face zones	17
Type of cell	Hexahedral
Method of meshing	Mapping & Cooper scheme

A3.2 Fluent model at glance

Version 3d, segregated, realizable k-epsilon.

Model	**Setting**
Space	3D
Time	Steady
Viscous	Realizable k-ε turbulence model
Wall treatment	Standard wall functions
Domain motion	Stationary
Buoyancy	Non-buoyant
Heat transfer	Enabled
Solidification and melting	Disabled

Radiation	Disabled
Species transport	Disabled
Coupled dispersed phase	Disabled
Pollutants	Disabled
Soot	Disabled

A3.3 Solver Control

(a) Equation solved

Equations	**Solved**
Flow	Yes
Turbulence	Yes
Energy	Yes

(b) Numeric

Numeric	**Enabled**
Absolute velocity formulation	Yes

(c) Relaxation

Variable	**Relaxation factor**
Pressure	0.3
Density	1.0
Body force	1.0
Momentum	0.7
Turbulence Kinetic energy	0.8

Turbulence dissipation rate	0.8
Turbulence viscosity	1.0
Energy	1

(d) Linear solver

Variable	**Cycle type**	**Termination criteria**	**Residual reduction tolerance**
Pressure	V-cycle	0.1	
X-Momentum	Flexible	0.1	0.7
Y-Momentum	Flexible	0.1	0.7
Z-Momentum	Flexible	0.1	0.7
Turbulence kinetic energy	Flexible	0.1	0.7
Turbulence dissipation rate	Flexible	0.1	0.7
Energy	Flexible	0.1	0.7

(e)Discretization scheme

Variable	**Scheme**
Pressure	Standard
Pressure velocity compounding	Simple
Density	Second order upwind
Momentum	Second order upwind
Turbulence kinetic energy	Second order upwind
Turbulence dissipation rate	Second order upwind
Energy	Second order upwind

(f) Solution limits

Quantity	Limit
Minimum absolute pressure	1
Maximum absolute pressure	5000000
Minimum temperature	1
Maximum temperature	5000
Minimum turbulence kinetic energy	$1\times e^{-14}$
Minimum turbulence dissipation rate	$1\times e^{-20}$
Maximum turbulence viscosity rate	100000

A3.4 Material Property

(a) Material air (fluid)

Property	Units	Method	Value
Density	Kg/m^3	Ideal gas	1.225
Specific heat (C_p)	J/kg-K	Constant	1006.43
Thermal conductivity	W/m-K	Constant	0.0242
Viscosity	Kg/m-s	Constant	1.789×10^{-5}

(b) Material aluminum (solid)

Property	Units	Method	Value
Density	Kg/m^3	Constant	2719
Specific heat (C_p)	J/kg-K	Constant	871
Thermal conductivity	W/m-K	Constant	202.4

A3.5 Convergence criteria

Continuity	$1\times e^{-06}$
X-velocity	$1\times e^{-06}$
Y-velocity	$1\times e^{-06}$
Z-velocity	$1\times e^{-06}$
Energy	$1\times e^{-06}$
Turbulence kinetic energy (k)	$1\times e^{-06}$
Turbulence dissipation rate (ε)	$1\times e^{-06}$

A3.6 Operating conditions

Operating pressure (Pascal)	101325.00
Reference pressure location –X(m)	-0.089
Reference pressure location –Y(m)	0.00
Reference pressure location –Z (m)	0.0475

A3.7 Solution Initialization

Gauge pressure (Pascal)	0
X velocity (m/s)	102
Y velocity (m/s)	0.0
Z velocity (m/s)	0.0
Turbulence K.E. (m2/s2)	9.9999
Turbulence Dissipation rate (m2/s3)	1000.099
Temperature	299.99